Sensitivity of Mixed-Phase Low-Level Clouds to Secondary Ice Formation Processes

Master's Thesis in Meteorology
by

Patrick Kuntze

November 2019

Karlsruher Institut für Technologie

INSTITUTE FOR METEOROLOGY AND CLIMATE RESEARCH
KARLSRUHE INSTITUTE OF TECHNOLOGY (KIT)

Advisor: Prof. Dr. Hoose
Second Advisor: Prof. Dr. Leisner

Abstract

Today's numerical weather prediction still suffers from an underestimation of ice number concentrations in clouds. Inclusion of Secondary ice formation processes such as rime splintering, collision fragmentation, and droplet shattering could yield significant improvement. While several modeling studies on secondary ice production (SIP) in convective mixed-phase clouds have been carried out in resent years, similar investigations concerning these processes in stratiform clouds have been sparse. In this study a two moment bulk microphysics scheme is used within the ICON *(Icosahedral Nonhydrostatic*) model of the *Deutscher Wetterdienst* and the *Max-Planck Institute for Meteorology* in Hamburg to investigate a newly implemented temperature dependent set of SIP processes, consisting of these three mechanisms. Two types of arctic mixed-phase stratus clouds, based on observations during the *Indirect and Semi-Direct Aerosol Campaign* (ISDAC) respectively *Mixed-Phase Arctic Cloud Experiment* (M-PACE), are used in an idealized model set-up to analyze the sensitivity of cloud properties to the inclusion of the new SIP schemes. Additionally the simulations are run with two variants of the collisional breakup parameterization, once with a constant temperature dependent fragment generation function without consideration of the actual colliding particle classes, and a second time with an individually normed function, considering mass and velocity of the particles involved. Differences between both cloud cases, as well as the two applied collisional breakup variants are demonstrated.

Zusammenfassung

Die heutige numerische Wettervorhersage leidet immer noch unter der Unterschätzung von Eiskristall-Konzentrationen in Wolken. Die Berücksichtigung von sekundären Mechanismen der Eisbildung, wie das Emittieren von Fragmenten während der Bereifung von Eis, das Zerspringen von gefrierenden Regentropfen oder das Zersplittern von Teilchen durch Kollisionen (BR), könnte zu signifikanten Verbesserungen führen. Während in den letzten Jahren einige Modellierungsstudien zur sekundären Eisbildung in konvektiven Mischphasenwolken durchgeführt wurden, sind ähnliche Untersuchungen zu diesen Prozessen in geschichteten Wolken bisher selten. In der vorliegenden Arbeit wird ein mikrophysikalisches zwei-Momenten-Schema mit dem ICON (*Icosahedral Nonhydrostatic*) Modell des *Deutschen Wetterdienstes* und des *Max-Planck-Instituts für Meteorologie* in Hamburg verwendet, um neu implementierte, Temperatur abhängige Parametrisierungen der genannten Mechanismen zu untersuchen. Zwei Arten von arktischen Stratuswolken, die auf Observationen der *Indirect and Semi-Direct Aerosol Campaign* (ISDAC) und des *Mixed-Phase Arctic Cloud Experiment* (M-PACE)basieren, werden in einem idealisierten Modell Set-up verwendet, um Rückschlüsse auf die Sensitivität von Wolkeneigenschaften auf sekundäre Eisbildung zu ziehen. Zusätzlich werden die Simulationen, die den BR-Prozess beinhalten, mit zwei Varianten durchgeführt, die sich in der Skalierung der Funktion zur Berechnung der Fragmentanzahl unterscheiden. Ein Durchlauf wird mit konstanter Funktion für alle Kollisionen, unabhängig der teilnehmenden Teilchenarten, vorgenommen. Ein weiterer wird mit angepasster Funktion, unter Berücksichtigung von Teilchenmassen und -geschwindigkeiten durchgeführt. Zudem werden Unterschiede sowohl zwischen beiden Wolkenfällen als auch den verwendeten BR-Varianten herausgestellt.

Contents

1 Introduction 1

2 Theory 3

2.1 Mixed-Phase Clouds . . . 3

2.1.1 Freezing Processes . . . 5

2.1.2 Secondary Ice Formation Processes . . . 7

2.2 The ICON Model . . . 10

2.2.1 General Framework . . . 10

2.2.2 Cloud Microphysics . . . 11

3 Model Implementations 19

3.1 Preceding Work . . . 19

3.2 Secondary Mechanisms . . . 19

3.2.1 Rime Splintering . . . 20

3.2.2 Droplet Shattering . . . 21

3.2.3 Collisional Breakup . . . 23

Summary . . . 27

4 Simulations 29

4.1 General Set-Up and Grid Structure . . . 29

4.2 Observational Basis . . . 30

4.2.1 ISDAC . . . 30

4.2.2 M-PACE . . . 32

5 Results and Discussion 35

5.1 Time Evolution of the Mixed-Phase Clouds . . . 36

5.1.1 ISDAC . . . 36

5.1.2 M-PACE . . . 38

5.2 Liquid and Ice Water Path . . . 40

5.2.1 ISDAC . . . 40

5.2.2 M-PACE . . . 41

5.2.3 Liquid-Ice Partitioning . . . 42

5.3 Ice Crystal Number Concentration and SIP Rates . . . 43

5.3.1 ISDAC . . . 43

5.3.2 M-PACE . . . 44

5.4 SIP Dependence on Particle Profiles 46
5.4.1 Rime Splintering 46
5.4.2 Droplet shattering 47
5.4.3 Collisional Breakup 48
5.5 Vertical velocity of high SIP Grid Cells 49
5.5.1 ISDAC 49
5.5.2 M-PACE 51

6 Summary and Outlook **55**

List of Figures **59**

List of Tables **62**

References **71**

1 Introduction

Clouds play a huge role in our climate system. They are essential for liquid and solid precipitation, and therefore Earth's water cycle, influencing the eco system and human life. They provide freshwater and nutrients and clean the air, but also cause large destruction through heavy rainfall and hailstorms.
Reflection of solar radiation and absorption of infrared light influences the radiative balance of the earth and contributes to the temperature gradient between tropics and high latitudes. On the other hand may clouds transport energy over long distances or into high regions of the troposphere, when phase shifts of hydrometeors release or absorb latent heat [Lamb and Verlinde, 2011].
The effects of clouds on weather and climate are vast and complex and often sparsely understood. These circumstances lead to cloud parameterizations still contributing one of the largest uncertainties to climate and numerical weather prediction [Boucher et al., 2013]. Especially difficult to accurately represent are mixed-phase clouds, that is, in large part, due to the problems models have with handling supercooled water (Korolev et al. [2017] and references therein).
Mixed-phase clouds can be found in all kinds of environments under diverse conditions. Mülmenstädt et al. [2015] found that cold clouds contribute to precipitation in all latitudes but over the tropical ocean. Being common especially in high latitudes, Korolev et al. [2017] and further Shupe et al. [2005] advise investing research into arctic mixed-phase clouds.

One way to improve the understanding of clouds are sensitivity studies, in which the influence of certain parameterizations on the model result is tested. Here, the effects of secondary ice formation processes are analyzed in two idealized test cases of stratiform arctic mixed-phase clouds. The occurrence of secondary ice production (SIP) is evident through observations. The excess of measured ice crystal concentrations, compared to the concentration of ice nucleating particles (INP), is often several orders of magnitude. For temperature ranges where only heterogeneous nucleation is expected to produce ice, these findings demand additional sources of ice production [Rangno and Hobbs, 2001]. The most prominent processes, that are capable of such amplifications are rime splintering (RS), droplet shattering (DS) and collisional breakup (BR).

This study follows the concept of preceding investigations, where simulations were triggered by observational data to investigate these secondary sources of ice particle enhancement in the light of a real case scenario. Studies on convective systems include a simulation of a line of shallow cumulus clouds by Crawford et al. [2011], who found evidence for rime splintering being a strong source for ice particle enhancement. Lawson et al. [2015] investigated the rapid freezing in tropical cumuli by applying the droplet shattering process to a one-dimensional cloud model with explicit bin microphysics, and Phillips et al. [2017] implemented a new parameterization for collisional breakup and investigated its effects on a simulated convective storm.

Studies of SIP in stratiform clouds, however, are rarer. Such has been done by Fridlind et al. [2007] who investigated ice formation mechanisms, including SIP processes, in arctic mixed-phase clouds on the basis of observations from the *Mixed-Phase Arctic Cloud Experiment* (M-PACE) using a bin microphysics scheme of the *Distributed Hydrodynamic Aerosol-Radiation-Microphysics Application* (DHARMA) [Ackerman et al., 1995]. They used a parameterization by Vardiman [1978] for collisional breakup. Droplet shattering was represented by fragmenting large freezing droplets in a way, that the over all produced fragment number was enhanced by two. Fragment generation through rime splintering was calculated to be one ice splinter per 250 collisions with liquid particles between -3 and $-8\,^{\circ}\mathrm{C}$. Very little contribution of SIP processes to ice formation in these clouds was found.

In this study, the idealized model set-ups of two arctic stratiform clouds are analyzed and compared. They are based on intercomparison studies by Ovchinnikov et al. [2014], which was based on observations during the *Indirect and Semi-Direct Aerosol Campaign* (ISDAC), and by Klein et al. [2009], where the observational data was collected during M-PACE.
The sensitivity experiments are conducted using the ICON (*Icosahedral Nonhydrostatic*) model of the *Deutsche Wetterdienst* (DWD) and the *Max-Planck Institute for Meteorology* (MPI-M) in Hamburg. In order to represent the three mentioned SIP processes, temperature dependent parameterizations based on Sullivan et al. [2018] are implemented into the model code. Furthermore a modified version of the collisional breakup parameterization is used to analyze the influence of particle mass and velocity.
Cloud properties that are investigated include liquid water path (LWP), ice water path (IWP), particle mass mixing ratios, ice crystal number concentration (ICNC), vertical particle profiles, and vertical velocity.

2 Theory

Fundamental for the understanding of weather and climate is the knowledge of the underlying physical processes. In this study the emphasis is on the development of mixed-phase clouds in an idealized small scale model environment, especially regarding mass and number concentration of frozen particle regimes. Therefore a closer look on microphysical interactions in mixed-phase clouds is required.

In the first part of this chapter the theoretical basis of mixed-phase clouds and the analyzed processes are examined. The second part is concerned with the model parameterization of cloud microphysics.

2.1 Mixed-Phase Clouds

The mixed-phase regime is the part of a cloud between $0\,^{\circ}\mathrm{C}$ and around $-38\,^{\circ}\mathrm{C}$, below where practically all water droplets freeze homogeneously. In this region supercooled droplets exist alongside frozen particles, that interact in numerous ways. While air masses ascent through different temperature regions in the cloud they are exposed to different microphysical processes. Figure 2.1 shows a schematic overview of the particle types and processes, inherent to mixed-phase clouds, that are taken into account by the two moment microphysics scheme of Seifert and Beheng [2006], that is used in this study and is discussed in detail in section 2.2.2. Since liquid water is present, warm-cloud processes also occur and may enhance the formation of frozen particles.
Below $0\,^{\circ}\mathrm{C}$ liquid water is metastable and the laws of thermodynamics command that it transits to its stable solid phase. The transition of all liquid water in a particular cloud volume to ice is called glaciation. This happens through freezing processes or mass conversion, where water vapor deposits on existing ice particles, while liquid drops evaporate. The former is inhibited by an activation barrier and the latter depends strongly on the vertical motion of the cloud and the availability of ice particles [Lamb and Verlinde, 2011]. Freezing modes are discussed in section 2.1.1, mass conversion in the following paragraph.

If the ascent of the air masses is fast, supersaturation of water vapor can be met with regard to water and ice. In this case both types of hydrometeors grow by vapor condensation and deposition respectively. In this both-growth regime, accretion becomes the dominant process between both species and large rimed particles like graupel and hail may form and begin to accelerate against the updraft, collecting even more drops on their way.
If air masses are descending, water vapor may become subsaturated with regard to both phases, leading droplets and ice particles to evaporate and the cloud ultimately dissolves.
In the intermediate case the difference in saturation water pressure of ice and liquid water creates a

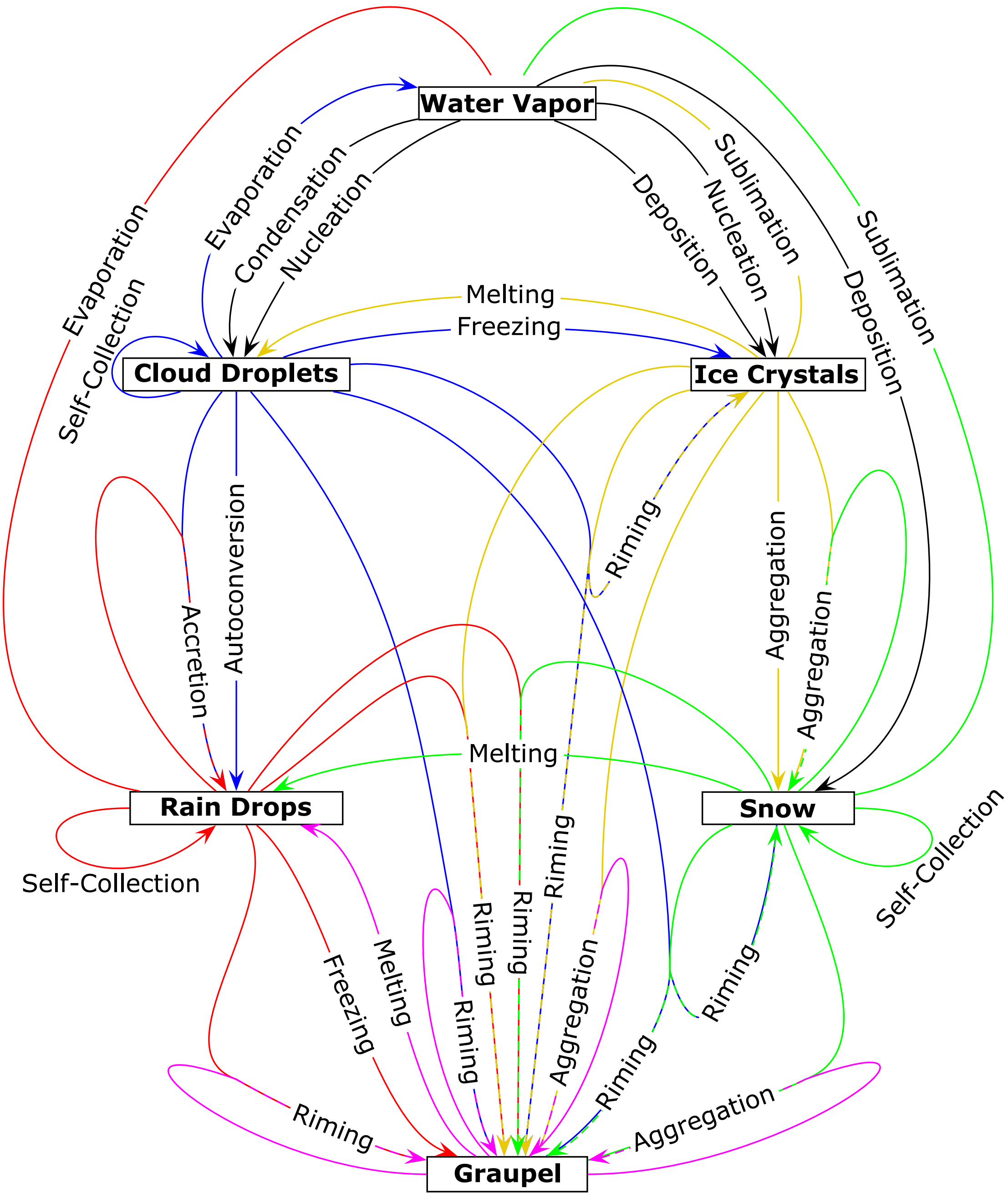

Figure 2.1: Cloud microphysical interactions included in the ICON model. The boxes represent the particle classes and water vapor. Larger particles are located further down. The arrowheads symbolize where the product of the process is assigned to. The colors of the arrow line represent the classes of all participating particles. (adapted from Seifert [2002])

situation where ice is supersaturated and liquid water is subsaturated. If the concentration of ice is not to high, the *Wegener-Bergeron-Findeisen* (WBF) process occurs, where cloud drops evaporate and ice particles grow through deposition until the whole cloud glaciates [Lamb and Verlinde, 2011].

Another factor that has to be considered for cloud glaciation is ice multiplication. This is the enhancement of primary ice particle concentration caused by SIP processes. These are discussed

in section 2.1.2.
In figure 2.2 an schematic overview of important processes in mixed-phase clouds, including primary and secondary ice formation, is shown for a convective cloud. Feedbacks between both are also included. There the three phase regimes of the cloud are depicted and the afore-mentioned processes are indicated in relation to their active temperature ranges. The secondary processes are positioned to the right, primary processes to the left. Capture nucleation is placed in between, because the fragments from SIP may serve as INP in the contact freezing mode. In the warm base of the cloud condensation and collision-coalescence is in effect, besides melting of falling ice particles. In the cold top homogeneous freezing is occurring.

In stratiform clouds, the situation is different, due to the typically slower vertical motion. This leads to growth by deposition and the WBF process. Snow ist often forming at cloud top and then falling slowly, resulting in a long time of exposure to water vapor and growth. In lower heights, where temperature rises, from the perspective of a falling particle, snow may aggregate and even rime while falling through the mixed-phase region [Lamb and Verlinde, 2011].

2.1.1 Freezing Processes

Since primary ice is necessary for secondary ice formation processes to tricker, a short overview over ice nucleation shall be given.

Homogeneous Freezing

Below 0 °C water may stay in the liquid state until an critical ice embryo is formed or freezing is initiated through an INP. The former is called homogeneous freezing and is a purely stochastical process depending on temperature and droplet size. The water molecules inside a droplet twist and diffuse through the liquid, forming metastable clusters of molecules with ice-like structure that dissolve again, until an critical embryo forms. The larger the liquid volume, the better the chances. For pure cloud droplets around $20\,\mu$m the temperature where 99.99 % of droplets freeze homogeneously is -38 °C [Lamb and Verlinde, 2011].

Heterogeneous Freezing

Cloud droplets may freeze upon contact with an existing INP above -38 °C. This is called heterogeneous freezing. An INP is an aerosol particle whose surface structure facilitates the arrangement of water molecules in an ice-like state. That way the activation barrier of the freezing process is lowered and the water transits into the more stable solid phase. There are three different processes resulting in heterogeneous freezing of droplets [Lamb and Verlinde, 2011].

Immersion Freezing Immersion freezing requires a not yet activate INP situated inside a liquid droplet. When the temperature then drops below a particle specific activation temperature ice forms around the immersed particle and serves as the nucleus. The drop then freezes entirely.

Deposition Nucleation Water vapor may deposit directly onto a dry INP and form a solid crystal without an intermediate liquid state. However, there are some conditions for deposition

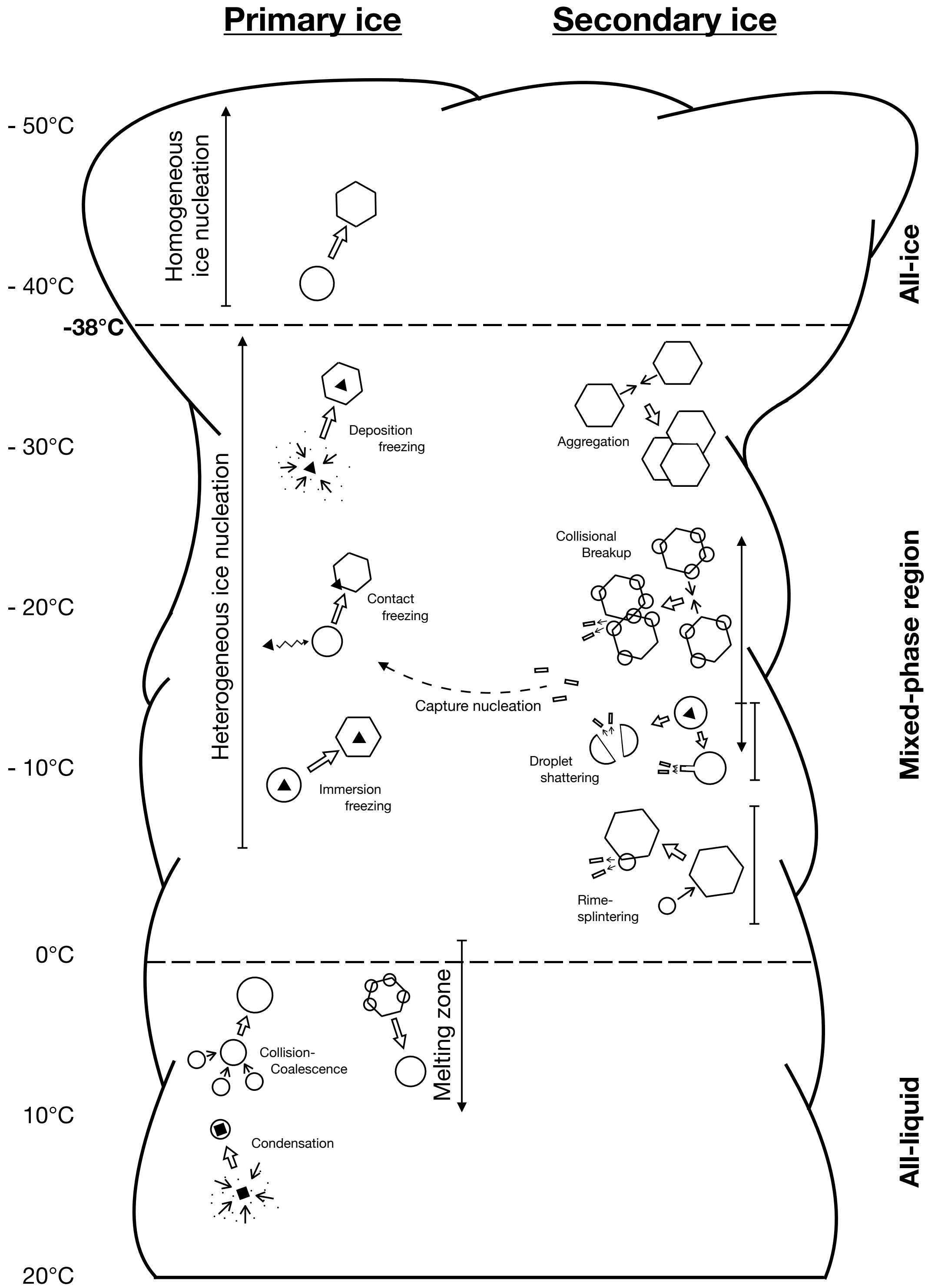

Figure 2.2: Schematic diagram of the main ice processes in convective clouds. The depicted cloud is segmented by dashed lines into an all-liquid, a mixed-phase, and an all-ice part. Round symbols represent liquid droplets, hexagonal shapes symbolize frozen and combinations of both rimed particles, and fragments from SIP are indicated as small rectangles. The values on the left side showcase the spacial distribution of cloud temperature. Temperature ranges, where the microphysical processes are active, are symbolized by arrows and bars. An arrow with bar indicates an one sided open range, two bars a relatively constrained range, and the bar with two arrows indicates a two sided open range with a defined efficiency maximum. (based on Lamb and Verlinde [2011] and Hartmann [2019])

nucleation. First, the surface lattice of the INP and that of ice have to be so similar that the activation barrier is reduced sufficiently to form an ice nucleus in the present temperature regime. Further more, water vapor has to be supersaturated with respect to ice and subsaturated with respect to liquid in order to bypass condensation [Lamb and Verlinde, 2011].

Contact Freezing A supercooled droplet can capture an INP that is already activated. The freezing process than immediately originates from the point of collision. In this case ice fragments can serve as INPs through capture nucleation.

2.1.2 Secondary Ice Formation Processes

Theories about processes that are capable of enhancing the concentration of ice particles are not just a recent subject. As long ago as the late 60s scientists wondered about the discrepancy between INP concentrations and ice crystal numbers in observations (e.g. Mossop et al. [1970] and Hobbs and Rangno [1985]). An example, where this is apparent, is shown in figure 2.3, that is taken from Mossop [1985].

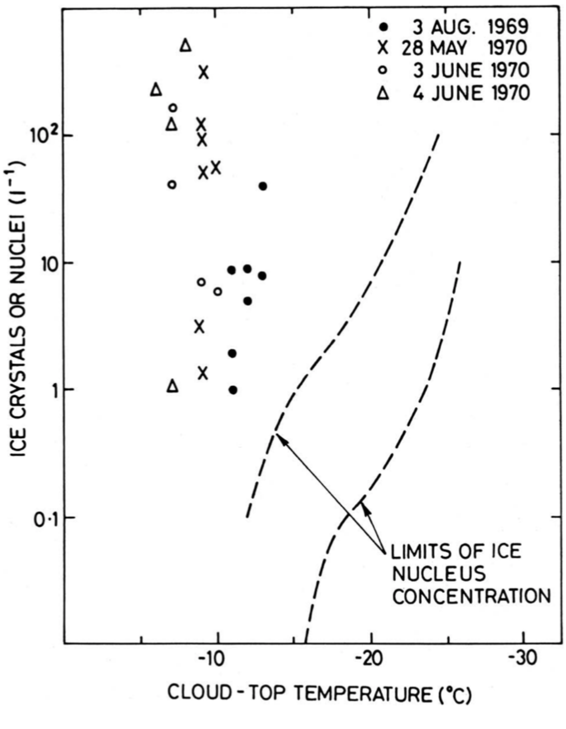

Figure 2.3: Number of ice crystals measured on 4 different dates plotted over the respective cloud top temperature. The dashed lines indicate the range of active INP concentration, while the different markers symbolizes measured ice crystal concentrations.

While several mechanisms are being discussed in the scientific community, this study concerns itself only with the afore-mentioned SIP processes. Such processes are not reliant on ice nucleating particles, but on pre-existing ice concentrations [Field et al., 2017]. Other processes, that are not discussed here include pre-activated INPs and thermophoretically enhanced contact freezing (Field et al. [2017] and further Beard [1992]).

Sublimation fragmentation, is another mechanism, that can be classified as SIP, but is not included in these experiments. There, a larger ice or snow crystal is separated into smaller fragments that loose contact after susceptible particle parts melt or evaporate. For a thorough discussion refer to Bacon et al. [1998].

In the following sections, a general introduction to the three examined processes, rime splintering, droplet shattering, and collisional breakup, is given. Model implementations are discussed in section 3.2.

Rime Splintering

In 1974 Hallett and Mossop [1974] provided experimental evidence for the rime splintering process, that could explain large values of ICNC in warm subzero temperatures.

This mechanism, also called the Hallett-Mossop process, is assumed to be active between $-3\,°\mathrm{C}$ and $-8\,°\mathrm{C}$, under abundance of rain drops or cloud droplets larger than $25\,\mu\mathrm{m}$ or smaller than $13\,\mu\mathrm{m}$ [Field et al., 2017]. Though it is not yet clear, whether the air temperature is more important or the particle surface temperature as suggested in Heymsfield and Mossop [1984].

As supercooled drops are collected by larger frozen particles like graupel or hail, they can produce splinters while freezing at the particle surface. Although, the exact process is still not understood, several promising theories have been made. For a comprehensive overview see Field et al. [2017].

Most models use a simple proportional approach where the amount of fragments produced by RS depends linearly on the amount of rimed mass (e.g. Crawford et al. [2011], Sullivan et al. [2017b], Huang et al. [2017]). The same is done in this study.

Droplet Shattering

When water drops freeze, they first form a frozen outer shell and continue to freeze inwards. As the frozen water expands, pressure is building up inside the drop, that can be release through cracks in the surface. Depending on drop size and temperature there is a chance the drop splits open into fragments. Apart from large irregular pieces that break free, smaller splinters can be ejected through spicules or frozen bubbles at the surface (e.g. Lauber et al. [2018], Rangno and Hobbs [2001] and further Brownscombe and Thorndike [1968], Mason and Maybank [1960]). Figure 2.4 shows a sequence of video frames of a shattering event from Lauber et al. [2018] where a droplet splits into two larger frozen particles and some smaller fragments that are emitted can be seen .

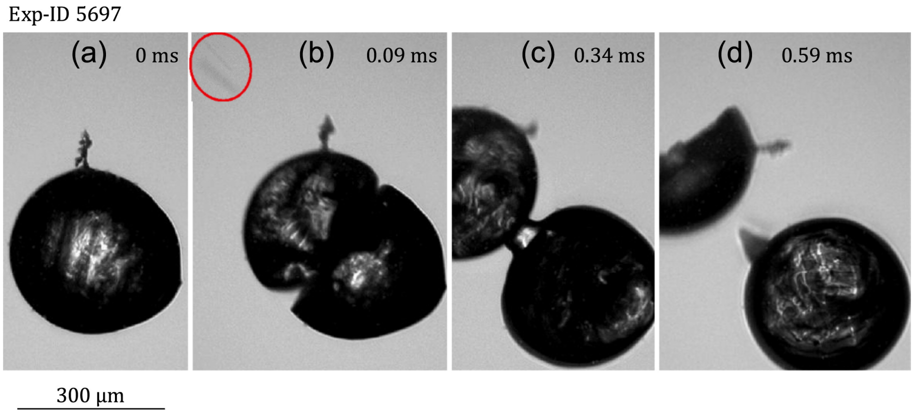

Figure 2.4: Droplet shattering event with two larger and some smaller fragments. The latter are highlighted inside the red circle. (from Lauber et al. [2018])

Droplet shattering is assumed to be most efficient between $-10\,^{\circ}\mathrm{C}$ and $-15\,^{\circ}\mathrm{C}$ [Lauber et al., 2018] and does not seam to occur on droplets smaller than $50\,\mu\mathrm{m}$ [Hobbs and Alkezweeny, 1968]. Model implementations have mainly been done by prescribing constant numbers of fragments per frozen drop (Field et al. [2017] and further Fridlind et al. [2007] and Lawson et al. [2015]), while recent parameterizations by Sullivan et al. [2017a] add a temperature dependent normal distributed shattering probability to the scheme. On this the parameterization in this study is build on.

Collisional Breakup

A SIP mechanism that could be expected in all kinds of clouds with ice formation is collisional breakup, though the amount of fragments is expected to greatly depend on temperature [Takahashi et al., 1995] and riming fraction [Vardiman, 1978]. Also particle mass and particle velocity play a substantial role (Vardiman [1978], Phillips et al. [2017]).
Takahashi et al. [1995] analyzed the collision of two graupel particles in a mechanical laboratory set-up and found that the maximum fragment generation lies around $-15\,^{\circ}\mathrm{C}$. Figure 2.5 shows the findings.

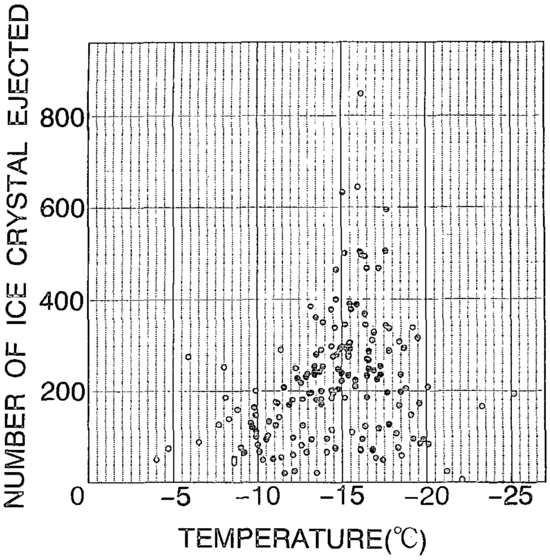

Figure 2.5: Fragment number of graupel-graupel-collisions during laboratory experiments of Takahashi et al. [1995] with a collision force of $5 \times 10^{-3}\,\mathrm{N}$. The fragment maximum appears to center around $-15\,^{\circ}\mathrm{C}$.

There have been several different strategies to implement parameterizations of collisional breakup into models. Fridlind et al. [2007] used an ansatz based on Vardiman [1978], where the fragment generation rate dependents on the change of particle momentum. Sullivan et al. [2017a] took a different approach, where the fragment production only depends on a temperature function based on the findings of Takahashi et al. [1995]. An physically more complete parameterization was introduced by Phillips et al. [2017], where the collision kinetic energy of two colliding particles play a major role.

2.2 The ICON Model

2.2.1 General Framework

The Icosahedral Nonhydrostatic model is a unified modeling system for global numerical weather prediction (NWP) and climate modeling. Like its predecessor, the GME, it uses a triangular grid structure. Mapping the globe in the shape of an icosahedral body, the model does not suffer from non-uniformity of grid cells, which is advantageous over models using a rectangular structure [Deutscher Wetterdienst, 2019].
The desired grid resolution is constructed by first n-secting the triangle edges followed by iterative bisection of the resulting gird. To save computational cost one can use a nesting mechanism for a local refinement [Zängl et al., 2015]. However, because ICON uses an unstructured grid, required resources increase dramatically under use of higher-accuracy schemes [Dipankar et al., 2015].

The model solves a system of prognostic nonhydrostatic equations for a set of variables. These are the horizontal velocity component normal to the triangle edges υ_n, the vertical wind component w, density ρ, virtual potential temperature θ_v, and the specific masses and number densities of tracers q_j, that include water vapor q_v and all of the contained hydrometeor classes. Except for υ_n, that is defined at the midpoints of the triangle edges, all prognostic variables are appointed to the grid cell centers.
There are different time steps on which different parts of the model operate. The dynamical core on default is called five times during one cycle of tracer advection, numerical dissipation and physics parametrization. The latter again is divided into so called slow-physics, that include radiation and convection, and fast-physics, e.g. saturation adjustment, cloud microphysics and turbulence. The slow-physics time step is defined by the user as a multiple of the fast-physics time step [Zängl et al., 2015].
To provide a variable applicability, three physics packages are available, suitable for either climate modeling, numerical weather prediction or large eddy simulations.

The model version used for this study is the 2.1.0 ICON-LEM (large eddy model) received from the DWD during the ICON training course 2018.
The aim of large eddy simulations (LES) is to improve the representation of clouds. This can only be done if the resolution is dramatically increased to a point, where cloud cover and shallow convection are directly resolved instead of parameterized. A typical resolution is $\mathcal{O}(100\,\mathrm{m})$, which is also used in this study. In order to fulfill the requirements for the new representations of turbulence and convection, a diagnostic Smagorinsky scheme, modified by Lilly [1962] is used for subgrid-scale turbulence, prognostic winds, potential temperature, specific humidity and specific cloud liquid water (Dipankar et al. [2015], Heinze et al. [2016]).
The default microphysics scheme implemented in the LEM package is a two-moment microphysics scheme based on Seifert and Beheng [2006], that is used in this study and discussed in section 2.2.2.

For a comprehensive discussion of the ICON model refer to Zängl et al. [2015] and to Dipankar et al. [2015] and Heinze et al. [2016] for more details about the ICON-LEM version.

2.2.2 Cloud Microphysics

Throughout all experiments a modified two-moment bulk microphysics scheme of Seifert and Beheng [2006] has been used. Since the main focus lies on the ice phase, only the corresponding microphysical processes are explained here in detail.

Particle Classes

The model predicts six types of hydrometeors, which are cloud droplets, rain drops, ice crystals, snow, graupel and hail. These are represented by number density size distributions of the form:

$$f(x) = A \cdot x^{\nu} \cdot exp\left(-\lambda x^{\mu}\right), \tag{2.1}$$

i.e. generalized Γ-distributions with mass x, rate parameter λ, and coefficients ν and μ, that are class dependent and summarized in table 2.1 beside the mean mass ranges of the particle classes.

Table 2.1: Power laws for equivalent spherical diameter and terminal fall velocitie of all hydrometeor classes, coefficients of the particles generalized Γ-distributions and corresponding ranges of mean particle mass. The power law coefficients are rounded to three decimal places.

particle class	max. diameter $D(x)$ (D in m, x in kg)	fall velocity $\upsilon(x)$ (υ in $m \cdot s^{-1}$, x in kg)	ν	μ	$\bar{x}_{min}$ (in kg)	$\bar{x}_{max}$ (in kg)
cloud dropletts	$D(x) = 0.124\, x^{1/3}$	$\upsilon(x) = 3.75 \cdot 10^5\, x^{2/3}$	1	1	$4.2 \cdot 10^{-15}$	$2.6 \cdot 10^{-10}$
rain drops	$D(x) = 0.124\, x^{1/3}$	$\upsilon(x) = 114.014\, x^{0.234}$	0	1/3	$2.6 \cdot 10^{-10}$	$3.0 \cdot 10^{-6}$
ice crystals	$D(x) = 0.835\, x^{0.39}$	$\upsilon(x) = 27.7\, x^{0.216}$	0	1/3	$1.0 \cdot 10^{-12}$	$1.0 \cdot 10^{-5}$
snow	$D(x) = 5.130\, x^{1/2}$	$\upsilon(x) = 8.294\, x^{1/8}$	0	1/2	$1.0 \cdot 10^{-10}$	$2.0 \cdot 10^{-5}$
graupel	$D(x) = 0.142\, x^{0.314}$	$\upsilon(x) = 86.894\, x^{0.268}$	1	1/3	$1.0 \cdot 10^{-9}$	$5.0 \cdot 10^{-4}$
hail	$D(x) = 0.137\, x^{1/3}$	$\upsilon(x) = 39.3\, x^{1/6}$	1	1/3	$2.6 \cdot 10^{-9}$	$5.0 \cdot 10^{-4}$

The coefficients A and λ can be expressed by the number (N_j) and mass (L_j) concentrations:

$$A = \frac{\mu N}{\Gamma\left(\frac{\nu+1}{\mu}\right)} \lambda^{\frac{\nu+1}{\mu}}, \tag{2.2}$$

$$\lambda = \left[\frac{\Gamma\left(\frac{\nu+1}{\mu}\right)}{\Gamma\left(\frac{\nu 21}{\mu}\right)} \bar{x}\right]^{-\mu} \tag{2.3}$$

Note that one has always:

$$L_j = \bar{x}_j \cdot N_j, \tag{2.4}$$

with $\bar{x}_j$ being the mean particle mass, L_j the total mass mixing ratio, and N_j the total number of particles of particle type j.

The two fundamental variables, that are tracked explicitly are mass density L_j and number concentration N_j. These are the zeroth and first moment m of the number density size distribution function regarding any one of the six particle classes:

$$M_j^m = \int_0^\infty x^m \cdot f_j(x)dx, \quad m \in \{0,1\}. \tag{2.5}$$

With equations 2.1 to 2.3 the power moments reads:

$$M_j^m = \frac{\Gamma\left(\frac{m+\nu+1}{\mu}\right)}{\Gamma\left(\frac{\nu+1}{\mu}\right)} \left[\frac{\Gamma\left(\frac{\nu+1}{\mu}\right)}{\Gamma\left(\frac{\nu+2}{\mu}\right)}\right]^m N_j\, x^m, \quad m \in \{0,1\}. \tag{2.6}$$

Since only those two quantities are explicitly traced throughout the simulation other particle attributes have to be specifically derived from these whenever they are needed. Most importantly, size and terminal fall velocity are related to their masses by class specific power laws:

$$D_j(x) = a_j \cdot x^{b_j}, \tag{2.7}$$

$$\upsilon_j(x) = \alpha_j \cdot x^{\beta_j}. \tag{2.8}$$

Table 2.1 also includes these power laws with explicit coefficients for all particle classes.

Balance Equations

The general equations that provide the physical basis of any changes to the fundamental variables are the balance equations for mass

$$\frac{\partial L_j}{\partial t} = -\nabla \cdot (\vec{\upsilon} L_j) + \nabla \cdot (K_h \nabla L_j) - \frac{\partial}{\partial z}(\overline{\upsilon}_{j,0} N_j) + \sum_{XYZ} \left.\frac{\partial L_j}{\partial t}\right|_{XYZ} \tag{2.9}$$

and number concentration

$$\frac{\partial N_j}{\partial t} = -\nabla (\vec{\upsilon} N_j) + \nabla (K_h \nabla N_j) - \frac{\partial}{\partial z}(\overline{\upsilon}_{j,0} N_j) + \sum_{XYZ} \left.\frac{\partial N_j}{\partial t}\right|_{XYZ} \tag{2.10}$$

of each particle class. Here the first three terms on the right side of the equal sign are an advection term with the mean wind velocity $\vec{\upsilon}$, a turbulent diffusion term with the turbulent diffusion coefficient for heat K_h, and a sedimentation term with $\overline{\upsilon}_{j,0}$ being the mean sedimentation velocity of the m-th moment and particle class j. The sources for change of these variables are indicated by the sum over XYZ, where the index serves as a placeholder for any microphysical process effecting mass or number concentration.

The ice phase processes included in the model involve nucleation (NUC), condensation/evaporation (CND), deposition/sublimation (DEP), freezing (FRZ), melting (MEL), autoconversion (AUT),

accretion (*ACC*), self-collection (*SLF*), collisional interaction(*CLS*), particle conversion (*CNV*), and secondary ice production mechanisms (*SIP*).
Transition of particles from one class j to another class k, e.g. through growth processes, or mass transfer through collection processes is computed following mass conservation and the identity:

$$\left.\frac{\partial L_j}{\partial t}\right|_{XYZ} = - \left.\frac{\partial L_k}{\partial t}\right|_{XYZ} . \tag{2.11}$$

Collection Processes

Another important microphysical process that needs to be characterized more thoroughly, since it is essential for both rime splintering and collisional breakup, is the collection process. Hydrometeors from any class can collide with particles of the same or of different types. In case the collision partners stick they form a new particle, that is put into the fitting class depending on its size. Only processes involving frozen hydrometeors are considered here.
Here, the central aspect is the collection kernel $K_{jk}\left(x_j, x_k\right)$. Expanding equation 2.5, the evolution of the size distribution moments of collecting particle class j and collected particle class k reads as follows:

$$\left.\frac{\partial M_j^m}{\partial t}\right|_{CLE,jk} = + \int_0^\infty \int_0^\infty K_{jk}\, f_j\left(x_j\right) f_k\left(x_k\right)\, \left[\left(x_j + x_k\right)^m - x_j^m\right]\, dx_j dx_k, \tag{2.12}$$

$$\left.\frac{\partial M_k^m}{\partial t}\right|_{CLE,jk} = - \int_0^\infty \int_0^\infty K_{jk}\, f_j\left(x_j\right) f_k\left(x_k\right)\, x_k^m\, dx_j dx_k. \tag{2.13}$$

With $m \in \{0,1\}$, i.e. particle number and mass concentration, equations 2.12 and 2.13 reduce to:

$$\left.\frac{\partial N_j}{\partial t}\right|_{CLE,jk} = 0, \tag{2.14a}$$

$$\left.\frac{\partial N_k}{\partial t}\right|_{CLE,jk} = - \int_0^\infty \int_0^\infty K_{jk}\, f_j\left(x_j\right) f_k\left(x_k\right)\, dx_j dx_k, \tag{2.14b}$$

$$\left.\frac{\partial L_j}{\partial t}\right|_{CLE,jk} = + \int_0^\infty \int_0^\infty K_{jk}\, f_j\left(x_j\right) f_k\left(x_k\right)\, x_k\, dx_j dx_k, \tag{2.14c}$$

$$\left.\frac{\partial L_k}{\partial t}\right|_{CLE,jk} = - \int_0^\infty \int_0^\infty K_{jk}\, f_j\left(x_j\right) f_k\left(x_k\right)\, x_k\, dx_j dx_k. \tag{2.14d}$$

The collection kernel K_{jk} depends on a collection efficiency coefficient E_{jk}, the relative velocity of both collision partners $\left|\upsilon_j\left(x_j\right) - \upsilon_k\left(x_k\right)\right|$, and the cross sections of both particle types, that are represented by a combined function $G_{jk}\left(x_j, x_k\right)$:

$$K_{jk}\left(x_j, x_k\right) = E_{jk}\, \left|\upsilon_j\left(x_j\right) - \upsilon_k\left(x_k\right)\right|\, G_{jk}\left(x_j, x_k\right). \tag{2.15}$$

If sphericity of particles is assumed the cross section function can be defined as:

$$G_{jk}(x_j,x_k) = \frac{\pi}{4}\left[D_j(x_j) + D_k(x_k)\right]^2, \tag{2.16}$$

where $D(x)$ is the particle diameter from equation 2.7.

Because the model handles particle ensembles with the aid of size distributions, computation of the absolute value of velocity differences is not straight forward and can not be simply approached by using mean values. To retain a non-vanishing result in case of equal mean fall velocities of two particle ensembles an improved Wisner-Approximation, as discussed in Seifert [2002], is used to calculate the characteristic fall velocity difference $\overline{\Delta\upsilon_{jk}}$:

$$\overline{\Delta\upsilon_{jk}}^2 = \frac{1}{\mathcal{N}} \int\limits_{x_k=0}^{\infty} \int\limits_{x_j=0}^{\infty} \int\limits_{\upsilon_j=0}^{\infty} \int\limits_{\upsilon_k=0}^{\infty} (\upsilon'_j - \upsilon'_k)^2\, D_j^2(x_j) D_k^2(x_k)\, f_j(x_j) f_k(x_k) \\ P_j(\upsilon'_j,x_j) P_k(\upsilon'_k,x_k)\, x_k^m\, d\upsilon'_k d\upsilon'_j dx_j dx_k, \tag{2.17}$$

with a normalization factor $\mathcal{N}$. Here, normal distribution functions for velocity $P(\upsilon,x)$ are used to take statistical deviations from the velocity-size relation in equation 2.8 into account. Under consideration of generalized Γ-distributions $f_j(x_j)$ and $m = 0$, integrating yields:

$$\overline{\Delta\upsilon_{jk}}^2 = \vartheta_j^0 \upsilon_j^2(\bar{x}_j) - \vartheta_{jk}^0 \upsilon_j(\bar{x}_j) \upsilon_k(\bar{x}_k) + \vartheta_k^0 \upsilon_k^2(\bar{x}_k) + \sigma_j^2 + \sigma_k^2, \tag{2.18}$$

while $m = 1$ leads to:

$$\overline{\Delta\upsilon_{jk}}^2 = \vartheta_j^0 \upsilon_j^2(\bar{x}_j) - \vartheta_{jk}^1 \upsilon_j(\bar{x}_j) \upsilon_k(\bar{x}_k) + \vartheta_k^1 \upsilon_k^2(\bar{x}_k) + \sigma_j^2 + \sigma_k^2, \tag{2.19}$$

where ϑ_j^m are dimensionless coefficients, that are formulated in equations 2.33 and 2.34 and σ_j are the variances of the velocity distributions, listed in table 2.2.

Table 2.2: Some attributes of the frozen particle classes essential for collection processes. $\overline{E}_{j,CLS}^{max}$ is the collision efficiency, D_{crit} is the critical diameter, below that collision efficiency is zero, q_{crit} is the lower limit of total mass mixing ratio necessary for the collection to happen, and σ_υ is the fall velocity variance.

particle class	$\overline{E}_{j,CLS}^{max}$	D_{crit} (μm)	q_{crit} $(kg \cdot kg^{-1})$	σ_υ $(m \cdot s^{-1})$
ice crystals	0.8	150	1.0×10^{-5}	0.05
snow	0.8	150	1.0×10^{-5}	0.25
graupel	1.0	100	1.0×10^{-6}	0.0
hail	1.0	100	1.0×10^{-6}	0.0

In general, the collection efficiency E_{jk} is a product of collision efficiency $E_{jk,CLS}$ and sticking efficiency $E_{jk,stick}$, which are summarized in table 2.3.

The latter is parameteriesed as a temperature dependent mean efficiency and in case of riming of cloud droplets or rain on any frozen particles assumed to be one. For graupel-graupel-collisions,

Table 2.3: Collision and sticking coefficients for all collection processes included in the ICON model. Information on the literary bases of the parameterizations is given in the text.

Collision Type (j+k)	$\overline{E}_{jk,stick,}$	$\overline{E}_{jk,CLS}$
i+i	$MIN[10^{0.035(T-T_c)-0.7}, 0.2]$	1
i+s, i+g, i+h, s+s, s+g, s+h	$MIN[e^{0.09(T-T_c)}, 1]$	1
g+g { dry wet	0.1 0.4	1
i+r, s+r, g+r, h+r	1	1
i+c, s+c, g+c, h+c	1	$\overline{E}_c(\overline{D}_c)\overline{E}_e(\overline{D}_e)$

$\overline{E}_{jk,stick}$ is 0.1 for dry and 0.4 for wet graupel. Colliding ice crystals follow a parametrization given in Cotton et al. [1986]:

$$\overline{E}_{ii,stick}(T) = MIN[10^{0.035(T-T_c)-0.7}, 0.2], \tag{2.20}$$

with T_c being the triple point temperature of water, 273.16 K. In all other cases one has:

$$\overline{E}_{jk,stick}(T) = exp\left(0.09(T-T_c)\right), \tag{2.21}$$

as in Lin et al. [1983].

Equivalently, mean collision efficiencies are used in this microphysics scheme. For collisions between frozen particles and collisions of frozen particles with raindrops, $\overline{E}_{jk,CLS}$ is assumed to be one for all diameters. In case of collisions that involve cloud droplets, critical minimum particle diameters $D_{j,crit}$ are nesessary for any collisions to happen. The parameterization is a product of piecewise linear functions depending on mean diameter for all collection partners:

$$\overline{E}_{ce,CLS}(\overline{D}_c, \overline{D}_e) = \overline{E}_c(\overline{D}_c) \cdot \overline{E}_e(\overline{D}_e), \tag{2.22}$$

with

$$\overline{E}_c(\overline{D}_c) = \begin{cases} 0, & \overline{D}_c < D_{c,crit} \\ \frac{\overline{D}_c - D_{c,crit}}{D_{c,1} - D_{c,crit}}, & D_{c,crit} < \overline{D}_c < D_{c,1}, \\ 1, & D_{c,1} < \overline{D}_c \end{cases} \tag{2.23}$$

and

$$\overline{E}_e(\overline{D}_e) = \begin{cases} 0, & \overline{D}_e < D_{e,crit} \\ \overline{E}^{max}_{e,CLS}, & D_{e,crit} < \overline{D}_e, \end{cases} \tag{2.24}$$

where e is a placeholder for either ice crystals, snow, graupel, or hail.

For all frozen particle classes, values of collision efficiency $\overline{E}^{max}_{j,CLS}$, associated critical diameter D_{crit}, and the limit of total mass mixing ratio q_{crit}, below that no particle collection occures are also summarized in table 2.2.

Applying the mean collision efficiency $\overline{E}_{jk,CLS}$, the sticking efficiency $\overline{E}_{jk,stick}$, the characteristic velocity difference $\overline{\Delta\upsilon_{jk}}$ (eq. 2.18), and the cross section function G_{jk} (eq. 2.16) to the collection cernel K_{jk} in equation 2.15 and consequently equations 2.14a to 2.14d, one has the following collection rates for mass and number concentrations of particle j and k:

$$\left.\frac{\partial N_j}{\partial t}\right|_{CLE,jk} = 0, \tag{2.25}$$

$$\left.\frac{\partial N_k}{\partial t}\right|_{CLE,jk} = -\frac{\pi}{4}\,\overline{E}_{jk,CLS}\overline{E}_{jk,stick}\,\overline{\Delta\upsilon_{jk}} \int_0^\infty\int_0^\infty \left[D_j(x_j)+D_k(x_k)\right]^2 f_j(x_j) f_k(x_k)\; dx_j dx_k, \tag{2.26}$$

$$\left.\frac{\partial L_j}{\partial t}\right|_{CLE,jk} = +\frac{\pi}{4}\,\overline{E}_{jk,CLS}\overline{E}_{jk,stick}\,\overline{\Delta\upsilon_{jk}} \int_0^\infty\int_0^\infty \left[D_j(x_j)+D_k(x_k)\right]^2 f_j(x_j) f_k(x_k)\; x_k\; dx_j dx_k, \tag{2.27}$$

$$\left.\frac{\partial L_k}{\partial t}\right|_{CLE,jk} = -\frac{\pi}{4}\,\overline{E}_{jk,CLS}\overline{E}_{jk,stick}\,\overline{\Delta\upsilon_{jk}} \int_0^\infty\int_0^\infty \left[D_j(x_j)+D_k(x_k)\right]^2 f_j(x_j) f_k(x_k)\; x_k\; dx_j dx_k. \tag{2.28}$$

Eventually, integrating yields:

$$\left.\frac{\partial N_j}{\partial t}\right|_{CLE,jk} = 0, \tag{2.29}$$

$$\left.\frac{\partial N_k}{\partial t}\right|_{CLE,jk} = -\frac{\pi}{4}\,\overline{E}_{jk,CLS}\overline{E}_{jk,stick}\,N_j N_k \left[\vartheta_j^0\upsilon_j^2(\overline{x}_j) - \vartheta_{jk}^0\upsilon_j(\overline{x}_j)\upsilon_k(\overline{x}_k) + \vartheta_k^0\upsilon_k^2(\overline{x}_k) + \sigma_j^2 + \sigma_k^2\right]^{\frac{1}{2}} \left[\delta_j^0 D_j^2(\overline{x}_j) - \delta_{jk}^0 D_j(\overline{x}_j) D_k(\overline{x}_k) + \delta_k^0 D_k^2(\overline{x}_k)\right], \tag{2.30}$$

$$\left.\frac{\partial L_j}{\partial t}\right|_{CLE,jk} = +\frac{\pi}{4}\,\overline{E}_{jk,CLS}\overline{E}_{jk,stick}\,N_j L_k \left[\vartheta_j^0\upsilon_j^2(\overline{x}_j) - \vartheta_{jk}^1\upsilon_j(\overline{x}_j)\upsilon_k(\overline{x}_k) + \vartheta_k^1\upsilon_k^2(\overline{x}_k) + \sigma_j^2 + \sigma_k^2\right]^{\frac{1}{2}} \left[\delta_j^0 D_j^2(\overline{x}_j) - \delta_{jk}^1 D_j(\overline{x}_j) D_k(\overline{x}_k) + \delta_k^1 D_k^2(\overline{x}_k)\right], \tag{2.31}$$

$$\left.\frac{\partial L_k}{\partial t}\right|_{CLE,jk} = -\frac{\pi}{4}\,\overline{E}_{jk,CLS}\overline{E}_{jk,stick}\,N_j L_k \left[\vartheta_j^0\upsilon_j^2(\overline{x}_j) - \vartheta_{jk}^1\upsilon_j(\overline{x}_j)\upsilon_k(\overline{x}_k) + \vartheta_k^1\upsilon_k^2(\overline{x}_k) + \sigma_j^2 + \sigma_k^2\right]^{\frac{1}{2}} \left[\delta_j^0 D_j^2(\overline{x}_j) - \delta_{jk}^1 D_j(\overline{x}_j) D_k(\overline{x}_k) + \delta_k^1 D_k^2(\overline{x}_k)\right], \tag{2.32}$$

with $\bar{x}$ being the mean masses of the particle size distributions.
Again considering Γ-distributions for $f_j\left(x_j\right)$, the dimensionless coefficients ϑ_{jk}^m and δ_j^m are defined as:

$$\vartheta_j^m = \frac{\Gamma\left(\frac{2\beta_j+2b_j+\nu_j+1+m}{\mu_j}\right)}{\Gamma\left(\frac{2b_j+\nu_j+1+m}{\mu_j}\right)} \left[\frac{\Gamma\left(\frac{\nu_j+1}{\mu_j}\right)}{\Gamma\left(\frac{\nu_j+2}{\mu_j}\right)}\right]^{2\beta_j} \tag{2.33}$$

$$\vartheta_{jk}^m = 2\,\frac{\Gamma\left(\frac{\beta_k+b_k+\nu_k+1+m}{\mu_k}\right)}{\Gamma\left(\frac{b_k+\nu_k+1+m}{\mu_k}\right)} \frac{\Gamma\left(\frac{\beta_j+b_j+\nu_j+1}{\mu_j}\right)}{\Gamma\left(\frac{b_j+\nu_j+1}{\mu_j}\right)} \left[\frac{\Gamma\left(\frac{\nu_k+1}{\mu_k}\right)}{\Gamma\left(\frac{\nu_k+2}{\mu_k}\right)}\right]^{\beta_k} \left[\frac{\Gamma\left(\frac{\nu_j+1}{\mu_j}\right)}{\Gamma\left(\frac{\nu_j+2}{\mu_j}\right)}\right]^{\beta_j} \tag{2.34}$$

$$\delta_j^m = \frac{\Gamma\left(\frac{2b_j+\nu_j+1+m}{\mu_j}\right)}{\Gamma\left(\frac{\nu_j+1}{\mu_j}\right)} \left[\frac{\Gamma\left(\frac{\nu_j+1}{\mu_j}\right)}{\Gamma\left(\frac{\nu_j+2}{\mu_j}\right)}\right]^{2b_j+m} \tag{2.35}$$

$$\delta_{jk}^m = 2\,\frac{\Gamma\left(\frac{b_k+\nu_k+1+m}{\mu_k}\right)}{\Gamma\left(\frac{\nu_k+1}{\mu_k}\right)} \frac{\Gamma\left(\frac{b_j+\nu_j+1}{\mu_j}\right)}{\Gamma\left(\frac{\nu_j+1}{\mu_j}\right)} \left[\frac{\Gamma\left(\frac{\nu_k+1}{\mu_k}\right)}{\Gamma\left(\frac{\nu_k+2}{\mu_k}\right)}\right]^{b_k+m} \left[\frac{\Gamma\left(\frac{\nu_j+1}{\mu_j}\right)}{\Gamma\left(\frac{\nu_j+2}{\mu_j}\right)}\right]^{b_j} . \tag{2.36}$$

These coefficients only depend on the size distribution function with constants ν and μ and particle atributes b and β from equation 2.7 and 2.8.

For a general overview of the two moments scheme refer to Seifert and Beheng [2006] and for a fully detailed elaboration see Seifert [2002].

3 Model Implementations of Secondary Ice Processes

This chapter treats the model code especially related to this thesis, namely the routines dealing with SIP. Before the different mechanisms and their scientific derivations are explained, the preceding changes of Dr. Beydoun to the original ICON code are outlined in short.
A summary of all parameters of the SIP implementations is given at the end of this chapter.

3.1 Preceding Work

As mentioned in section 2.2.1, the basis for this study is the ICON-LEM model version 2.1.0. Before modifications were made to the code as part of this study, Dr. Beydoun, who assumed supervision of this thesis, made some preceding changes to the ICON code. These concerned the fundamental coding structure for the SIP implementations, since only a default rime splintering parameterization based on Hallett and Mossop [1974] was included in the base version. This had been implemented for all relevant processes, i.e. riming of cloud droplets and rain drops on ice crystals, snow, graupel or hail.

A droplet shattering parameterization of Sullivan et al. [2017a] was implemented into the existing model code for heterogeneous freezing of rain drops.
In order to make particle-particle-collisions more case dependent, the existing subroutine was split into two cases, one for collisions involving ice crystals, and one for snow with graupel or hail. Snow-snow and graupel-graupel-collisions already had their own subroutines. Then a parameterization, again based on Sullivan et al. [2017a], was implemented for snow-graupel, snow-hail, and graupel-graupel-collisions. The parameterization of snow only collisions was carried out later by the author of this thesis.
Eventually on-off switches for each of the SIP processes were created to simplify their handling via a simulation run script.

3.2 Secondary Mechanisms

To simulate the influence of SIP mechanisms on the mass and number concentrations of the various particle types, representations of the three regarded processes, rime splintering, droplet shattering, and collisional breakup have been added into the ICON code. The algorithms are based on Sullivan et al. [2018], so the inherited code had to be slightly adjusted. The new parameterizations are explicitly dependent only on temperature. The following sections describe their literary basis and how they were implemented, as well as changes that have been made to improve their impact on the chosen scenarios.

The relation of these mechanisms to the greater microphysical picture given in section 2.2.2 lies in the source term regarding secondary ice production processes of the balance equations 2.9 and 2.10:

$$\left.\frac{\partial N_{ice}}{\partial t}\right|_{SIP} = \left.\frac{\partial N_{ice}}{\partial t}\right|_{RS} + \left.\frac{\partial N_{ice}}{\partial t}\right|_{DS} + \left.\frac{\partial N_{ice}}{\partial t}\right|_{BR}, \tag{3.1}$$

with the identifiers RS, DS, and BR representing rime splintering, droplet shattering, and collisional breakup respectively.
On this initial point the following considerations are based.

3.2.1 Rime Splintering

The rate of change in ice crystal numbers caused by rime splintering is described by the product of rime mixing ratio q_{rime}, a weighting function dependent on temperature $w_{RS}(T)$, and a constant factor $\aleph_{RS}$, that indicates the amount of fragments produced per kg of rime:

$$\left.\frac{\partial N_i}{\partial t}\right|_{RS} = \aleph_{RS}\, w_{RS}(T)\, q_{rim}. \tag{3.2}$$

The weighting function is of triangular form:

$$w_{active}(T) = \frac{T - T_{min}}{T_{opt} - T_{min}} \frac{T - T_{max}}{T_{opt} - T_{max}}, \tag{3.3}$$

between 265 K and 270 K and has its maximum at 268 K. Outside this temperature range the function is zero. With these assumptions $w_{RS}(T)$ yields:

$$w_{RS}(T) = \begin{cases} 0, & T < 265\,\mathrm{K} \\ \frac{T-265\,\mathrm{K}}{3\,\mathrm{K}} \frac{T-270\,\mathrm{K}}{-2\,\mathrm{K}}, & 265\,\mathrm{K} < T < 270\,\mathrm{K}, \\ 0, & 270\,\mathrm{K} < T \end{cases} \tag{3.4}$$

and is shown in figure 3.2 alongside the fragment number functions of droplet shattering and collisional breakup. The model runs with 3.5×10^8 fragments produced from 1 kg rime, which corresponds to one fragment per 250 collision events:

$$\aleph_{RS} = 3.5 \times 10^8\, (\mathrm{kg} \cdot \mathrm{rime})^{-1}. \tag{3.5}$$

Any ice crystals generated by this process in each simulation time step are added to the tracked number concentration of ice crystals N_i while the mass concentration is adjusted by adding the number multiplied by the minimal ice crystal mass $x_{i,min}$ to the mass mixing ratio L_i:

$$N_i' = N_{i,0} + N_{i,RS}, \tag{3.6}$$

$$L_i' = L_{i,0} + N_{i,RS}\, x_{i,min}. \tag{3.7}$$

While the number concentration of the rimed particle class stays the same, the riming particle freezes and is transferred into another class. That leads to following changes:

$$N'_e = N_{e,0}, \tag{3.8}$$

$$L'_e = L_{e,0} + N_{w,rime} \cdot \bar{x}_w, \tag{3.9}$$

$$N'_w = N_{e,0} - N_{w,rime}, \tag{3.10}$$

$$L'_w = L_{w,0} - N_{w,rime}\, \bar{x}_w, \tag{3.11}$$

with $e \in \{i,s,g,h\}$, $w \in \{c,r\}$, the initial values $N_{j,0}$ and $L_{j,0}$, and $\bar{x}_w$ being the mean mass of the riming particle class.

3.2.2 Droplet Shattering

The rate of fragment generation by droplet shattering depends on the heterogeneous freezing rate of rain and a droplet shattering rate. The latter itself is a product of freezing rate, a shattering probability function $p_{DS}\big(T \mid T_\mu, \sigma\big)$, depending on temperature, and a constant factor $\aleph_{DS}$, that indicates the amount of additional fragments per shattering event:

$$\left.\frac{\partial N_{frag}}{\partial t}\right|_{DS} = [1 + p_{DS}\ \aleph_{DS}]\ \left.\frac{\partial N_r}{\partial t}\right|_{FRZ}, \tag{3.12}$$

with the number of total fragments:

$$N_{\Sigma,frag} = [1 + p_{DS}\ \aleph_{DS}]\ \left.\frac{\partial N_r}{\partial t}\right|_{FRZ} dt. \tag{3.13}$$

The shattering probability is described by a normal distribution $\mathcal{N}\big(T \mid T_\mu, \sigma\big)$, with the mean temperature T_μ and standard deviation σ:

$$p_{DS}\big(T \mid T_\mu, \sigma\big) = \frac{p_{max}}{\max\big[\mathcal{N}\big(T \mid T_\mu, \sigma\big)\big]}\mathcal{N}\big(T \mid T_\mu, \sigma\big), \tag{3.14}$$

$$\mathcal{N}\big(T \mid T_\mu, \sigma\big) = \frac{1}{\sqrt{2\pi\sigma^2}} \exp\left(-\frac{\big(T - T_\mu\big)^2}{2\sigma^2}\right), \tag{3.15}$$

where p_{max} is the maximum of 20 % at 258 K and the standard deviation is 3 K. On average ten fragments are assumed to break off in a shattering event:

$$p_{DS}\big(T \mid 258\,\mathrm{K}, 3\,\mathrm{K}\big) = 0.2\ \exp\left(-\frac{(T - 258\,\mathrm{K})^2}{18\,\mathrm{K}^2}\right), \tag{3.16}$$

$$\aleph_{DS} = 10. \tag{3.17}$$

Therefore the expression inside the square brackets in equation 3.12 can be interpreted as the number of fragments per event, that is again depicted in figure 3.2. Note, that even if a frozen rain drop does not shatter, equation 3.12 still applies and one fragment is generated, that is simply the frozen particle.

Heterogenous freezing is formulated following Bigg [1953], with the moment equations:

$$\left.\frac{\partial M_r^m}{\partial t}\right|_{FRZ} = -M_r^{m+1}\, J_{het}\big(T\big). \tag{3.18}$$

Thus the parameterization of the rain freezing rate depends on the number of rain drops N_r, the associated mean mass $\bar{x}_r$, and a temperature dependent rate coefficient $J_{het}\big(T\big)$:

$$\left.\frac{\partial N_r}{\partial t}\right|_{FRZ} = -N_r\, \bar{x}_r\, J_{het}\big(T\big), \tag{3.19}$$

with:

$$J_{het}\big(T\big) = b_{het}\,\Big(\exp\big[a_{het}(T_0 - T)\big] - 1\Big), \tag{3.20}$$

where $b_{het} = 0.2\,\mathrm{kg}^{-1}\,\mathrm{s}^{-1}$ and $a_{het} = 0.65\,\mathrm{K}^{-1}$ as in Barklie and Gokhale [1959] [Pruppacher and Klett, 1997]. T_0 is the freezing temperature $273.15\,\mathrm{K}$. Hence, the amount of rain drops that freeze is:

$$N_{r,FRZ} = N_r\, \bar{x}_r\, J_{het}\big(T\big)\; dt, \tag{3.21}$$

and the frozen mass is calculated by:

$$L_{r,FRZ} = M_r^2\, L_r\, \bar{x}_r\, J_{het}\big(T\big)\; dt, \tag{3.22}$$

where M_r^2 is the second moment of $f_r\big(x\big)$. In case of rain drops, with equation 2.6, $\nu = 0$, and $\mu = \frac{1}{3}$, one has $M_r^2 = 5.6$

The fragments produced by the model are added to the number of particles of either one of the ice crystal, graupel, or hail class, depending on their sizes. Therefore the Γ-distribution of all fragments is calculated and divided into three particle bins delimited by prescribed particle masses. This is done using the cumulative distribution function $F_{j,CDF}\big(x\,\big|\alpha_s,\lambda\big)$:

$$F_{j,CDF}\big(x_{j,lim}^{\mu}\,|\alpha_s,\lambda\,\big) = \int_0^{x_{j,lim}} f\big(x_j\,|\alpha_s,\lambda\,\big)\; dx_j = \frac{\gamma\big(\alpha_s,\lambda x_{j,lim}^{\mu}\big)}{\Gamma\big(\alpha_s\big)}, \tag{3.23}$$

with shape parameter α_s, rate parameter λ and $\gamma\big(\alpha_s,\lambda x_{lim}^{\mu}\big)$ being the lower incomplete Γ-function. With $\alpha_s = (\nu+1)/\mu$, taken from equation 2.1, the number of fragments smaller than the respective mass limits are then calculated by the following formula:

$$N_{j,frag} = J_{het}\big(T\big)\; N_r\; \bar{x}_{\Sigma,frag}\; \frac{\gamma\big(\frac{\nu+1}{\mu},\lambda x_{jk,lim}^{\mu}\big)}{\Gamma\Big(\frac{\nu+1}{\mu}\Big)}\; dt, \qquad (jk \in ig, gh), \tag{3.24}$$

where $x_{jk,lim}$ is the separation mass and either 6.56×10^{-8} kg for distinction of ice crystals and graupel or 1.0×10^{-6} kg for distinction between graupel and hail. $\bar{x}_{\Sigma,frag}$ is the mean mass of all fragments generated. The latter is calculated by dividing initial rain drop mean mass through the number of fragments per freezing event:

$$\bar{x}_{\Sigma,frag} = \frac{\bar{x}_r}{[1 + p_{DS}\ \aleph_{DS}]}. \tag{3.25}$$

It should be noted, that in reality larger drops freeze more rapidly and at warmer subzero temperatures while small droplets may stay liquid for as cold as $-30\,°\mathrm{C}$ [Khain et al., 2000]. Therefore it may be physically more accurate to recalculate $\bar{x}_{\Sigma,frag}$ by means of total fragment number and mass:

$$\bar{x}_{\Sigma,frag} = \frac{\bar{x}_{r,FRZ}}{[1 + p_{DS}\ \aleph_{DS}]} = \frac{L_{r,FRZ}}{N_{r,FRZ}}\ \frac{1}{[1 + p_{DS}\ \aleph_{DS}]}. \tag{3.26}$$

However, since the model does not discriminate between freezing rates of larger and smaller droplets, it should be acceptable to stick to the first parameterization.
As in equation 3.24, mass of fragments is handled equivalently:

$$L_{j,frag} = 5.6\ J_{het}\big(T\big)\ L_r\ \bar{x}_{\Sigma,frag}\ \frac{\gamma\big(\frac{\nu+2}{\mu}, \lambda x_{jk,lim}^{\mu}\big)}{\Gamma\left(\frac{\nu+2}{\mu}\right)}\ dt, \qquad (jk \in ig, gh). \tag{3.27}$$

Eventually the allocation of the fragments to different particle categories reads as follows:

$$N'_r = N_{r,0} - N_{r,FRZ}, \tag{3.28}$$
$$L'_r = L_{r,0} - L_{r,FRZ}, \tag{3.29}$$

$$N'_i = N_{i,0} + N_{i,frag}, \tag{3.30}$$
$$N'_g = N_{g,0} + N_{g,frag} - N_{i,frag}, \tag{3.31}$$
$$N'_h = N_{h,0} + N_{\Sigma,frag} - N_{g,frag}, \tag{3.32}$$

$$L'_i = L_{i,0} + L_{i,frag}, \tag{3.33}$$
$$L'_g = L_{g,0} + L_{g,frag} - L_{i,frag}, \tag{3.34}$$
$$L'_h = L_{h,0} + L_{r,FRZ} - L_{g,frag}, \tag{3.35}$$

with initial values $N_{j,0}$ and $L_{j,0}$. Note, that one has $L_{r,FRZ} = L_{\Sigma,frag}$, however $N_{r,FRZ} \neq N_{\Sigma,frag}$.

3.2.3 Collisional Breakup

Parameterization of collisional breakup was implemented for collisions of snow with either snow, graupel or hail, as well as graupel-graupel-collisions. Processes with ice crystals are neglected, since they are expected to contribute little to the total fragment numbers. Also collisions between hail particles and hail and graupel are neglected, because the number of hail particles is to small.

The algorithm that calculates fragment number produced by particle-particle-collisions is a product of collision rate and the amount of splinters per collision $\aleph_{BR}$:

$$\left.\frac{\partial N_i}{\partial t}\right|_{BR,jk} = \aleph_{BR} \left.\frac{\partial N_j}{\partial t}\right|_{CLS,jk} . \tag{3.36}$$

The former is a function of particle numbers of each class that is involved and the corresponding collection Kernel discussed in section 2.2.2:

$$\begin{aligned}\left.\frac{\partial N_j}{\partial t}\right|_{CLE,jk} = -\frac{\pi}{4}\,\overline{E}_{jk,CLS}\,N_j N_k & \\ \left[\vartheta_j^0 \upsilon_j^2(\overline{x}_j) - \vartheta_{jk}^0 \upsilon_j(\overline{x}_j)\upsilon_k(\overline{x}_k) + \vartheta_k^0 \upsilon_k^2(\overline{x}_k) + \sigma_j^2 + \sigma_k^2\right]^{\frac{1}{2}} & \\ \left[\delta_j^0 D_j^2(\overline{x}_j) - \delta_{jk}^0 D_j(\overline{x}_j) D_k(\overline{x}_k) + \delta_k^0 D_k^2(\overline{x}_k)\right], &\end{aligned} \tag{3.37}$$

with the collision efficiency $\overline{E}_{jk,CLS}$, particle velocities $\upsilon_j(\overline{x}_j)$ and the dimensionless coefficients ϑ_{jk}^m and δ_{jk}^m defined in equation 2.33 to 2.36. Weather the two particles stick or not, is not important here, hence the missing sticking coefficient.

The fragment number is temperature dependent and based on the laboratory experiments of Takahashi et al. [1995]. The number of ice fragments produced per collision of two artificial graupel particles during those experiments under varying environmental temperatures were previously shown in figure 2.5 of section 2.1.2. Sullivan et al. [2017b] characterized these results using a temperature dependent distribution:

$$\aleph_{BR_C} = F_{BR}\,(T - T_{min})^{1.2}\,\exp\left(-\frac{(T - T_{min})}{\gamma}\right), \tag{3.38}$$

where F_{BR} is a scaling factor, γ is the decay rate of the fragments at warmer temperatures, and T_{min} is the lower temperature limit where apparently fragment ejection is neglectable. Taken from figure 2.5, the maximum of the distribution lies around 258 K. In that regard T_{min} and γ are set to 252 K and 5 respectively. The amount of fragments generated is than calculated by:

$$N_{i,frag} = \aleph_{BR} \left.\frac{\partial N_j}{\partial t}\right|_{CLS,jk} dt. \tag{3.39}$$

In this study F_{BR} is handled differently in two sets of sensitivity experiments. In the first set, labeled BR_C from here on, F_{BR_C} is 50 and constant for all types of particle-particle collisions. This leads to a maximum of approximately 130 fragment per collision around 258 K. A plot of this distribution is again shown in figure 3.2. As a reference, the maximum amount of fragments produced in the parameterization $BR1ig$ of Sullivan et al. [2017b] was used (their figure 2a).

The disadvantage of this approach is the missing dependency on other variables than temperature. Therefore it seams inappropriate to assume the same parameterization for all collision types. Especially the abundant existence of snow, that was discovered in the first simulations, for both cloud cases, lead to the decision to include a snow-snow-collision parameterization and generally refine the algorithm of this process.

Phillips et al. [2017] introduced a new parameterization, that considers a physically more complete understanding of the process. This approach is based on the available collision kinetic Energy of two particles, that is used to create the new surface of the collision fragments after breakup. The temperature dependence is also based on Takahashi et al. [1995], but a simpler triangular fit is used. Besides that, this new concept accounts for particle sizes and fall velocities. Furthermore the parameterization is able to handle particle type, ice crystal habits, and riming fraction, that makes it more applicable for different collision types. It is of the following general form:

$$\aleph_{BR_V} = \alpha A\left(coll.\right)\left(1-\exp\left[-\left(\frac{(CK_0)}{\alpha A\left(coll.\right)}\right)^{\gamma}\right]\right), \tag{3.40}$$

where α is the equivalent spherical surface area of the smaller particle, $A\left(coll.\right)$ is the the density of breakable branches at the surface, that is dependent on the collision type, C is the asperity-fragility coefficient, K_0 is the collision kinetic energy, and γ is a shape parameter. This equation can be reduced further. α can be expressed as a function of equivalent-spherical diameter:

$$\alpha = \pi D_s^2 \tag{3.41}$$

and K_0 is a function of particle mass and velocities:

$$K_0 = \frac{m_j m_k}{2\left(m_j + m_k\right)}\left(\upsilon_1 - \upsilon_2\right)^2. \tag{3.42}$$

Diameter and velocities themselves could be expressed by equations 2.7 and 2.8, and therefore by mass. However, to avoid vanishing relative velocity differences by using the mean values of the particle size distributions, equation 2.19 is used again to calculate the characteristic collision velocity.

Within the scope of this study the parameterization of Phillips et al. [2017] is not directly implemented into the model, but, with the considerations made, it is possible to find more physically reliable values for F_{BR}, that should scale according to particle mass and characteristic velocity, collision type, and temperature. These are then used for the second set of experiments, that are labeled BR_V from here on. To find appropriate values for F_{BR_V} the following assumptions are made. For graupel-graupel-collisions the parameters of equation 3.40 read as follows:

$$\begin{aligned} A\left(M\right) = {} & 1.26\times10^4\left(1+\frac{0.0079}{D_s^{1.5}}\right) \\ & + max\left[2.52\times10^4\left(1+\frac{0.0079}{D_s^{1.5}}\right) - 4.2\times10^3\left(1+\frac{0.0079}{D_s^{1.5}}\right)\left|T-T_0\right|, 0\right], \end{aligned} \tag{3.43}$$

$$C = 2.205\times10^4, \tag{3.44}$$

$$\gamma = 0.3, \tag{3.45}$$

with the freezing temperature T_0 and the equivalent spherical diameter of the smaller particle D_s. Because the model version used in this study can not distinguish crystal habits, all other collisions are assumed to be spatial planar crystals (ice or snow) colliding with particles from any one of the frozen classes. In these cases the parameters read:

$$A\big(M\big) = 1.58 \times 10^{7}(1+100\Psi)\left(1+\frac{1.33\times 10^{-4}}{D_s^{1.5}}\right), \tag{3.46}$$

$$C = 7.08 \times 10^{6}\ \Psi, \tag{3.47}$$

$$\gamma = 0.5 - 0.25\ \Psi, \tag{3.48}$$

with the rimed fraction of the smaller particle Ψ, that is assumed to be of minor extend and set to 0.1 for ice crystals and snow.

In order to calculate the fragment numbers for each collision type individually, eventually some kind of representative values for particle masses have to be identified. As all particles are assumed to be Γ-distributed, the particle masses are averaged over time for all simulations in the BR_C experiments and than averaged again over all sensitivity runs, for each cloud case separately. The mean particle masses are summarized in table 3.1. These mean values are than used to calculate the collision type dependent fragment numbers $\aleph_{BR_V}$ and through inverting and applying equation 3.38 the new values for F_{BR_V} are found. These values are listed in table 3.2. It instantly stands out, that the particle masses in the ISDAC case, except for ice crystals, are larger than in the M-PACE case, leading to higher fragment generation during collisions. However, it will be shown, that this effect is completely counteracted by the smaller particle numbers in the ISDAC case.

Table 3.1: Mean masses of the BR_C simulations.

particle class	mean mass (kg)	
	ISDAC	M-PACE
ice crystals	1.21×10^{-7}	4.56×10^{-7}
snow	6.39×10^{-6}	7.41×10^{-7}
graupel	1.49×10^{-5}	1.12×10^{-5}
hail	2.51×10^{-5}	1.07×10^{-5}

Table 3.2: Number of fragments generated in specific particle-particle collision, as well as the corresponding scaling factors of the fragment generation functions, for both cloud cases.

collision type	ISDAC		M-PACE	
	$\aleph_{BR_V}$	F_{BR_V}	$\aleph_{BR_V}$	F_{BR_V}
graupel-graupel	17.2409	6.667	14.8331	5.7359
snow-snow	146.7283	56.7395	16.2396	6.2798
snow-graupel/hail	424.8077	164.2721	65.2204	25.2206

Figure 3.1 shows the fragment generation distributions (equation 3.38) with the new leading fac-

tors from the Phillips scheme. Largest fragment generation is expected in collisions of snow with

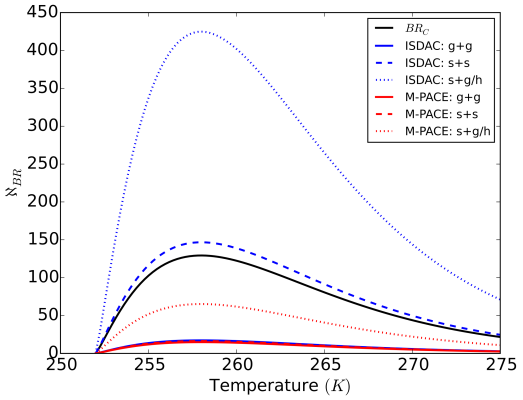

Figure 3.1: Fragment numbers generated by the Sullivan et al. [2017b] particle-particle-collision parameterization (equation 3.38) with leading factors depending on collision types and calculated with the Phillips et al. [2017] parameterization. Blue lines symbolize parameterization for the ISDAC case (section 4.2.1), red those for M-PACE case (section 4.2.2). Black is the reference simulation BR_C with a constant leading factor of 50.

graupel or hail. The BR_C parameterization is included for reference. It appears it greatly overestimates the particle collisions in the M-PACE case, but underestimates collisions in the ISDAC case, where snow is involved.

After the fragment numbers are calculated, the model adds any ice crystals produced by SIP directly to the tracked number concentration of ice crystals while the tracked mass concentration is adjusted by adding the number of fragments times the minimum possible ice crystal mass $x_{i,min}$:

$$N_i' = N_{i,0} + N_{i,frag}, \tag{3.49}$$

$$L_i' = L_{i,0} + N_{i,frag}\, x_{i,min}, \tag{3.50}$$

where $N_{i,0}$ and $L_{i,0}$ being initial values.
Conservation of mass demands:

$$L_j' = L_{j,0} - N_{i,frag}\, x_{i,min}, \tag{3.51}$$

with j indicating the more fragile particle class.

Summary

Figure 3.2 shows the temperature dependent parts of the SIP implementations. These are the temperature weighting function of rime splintering, the shattering probability distribution of droplet shattering, and the fragment generation function of the collisional breakup parameterization BR_C. Feedbacks may exist between droplet shattering and collisional breakup, due to the large overlap in temperature range. There fragments of particle-particle collisions could induce contact freezing of rain drops, that consequently may shatter.

All parameters of the SIP processes used in the model are summarized in table 3.3

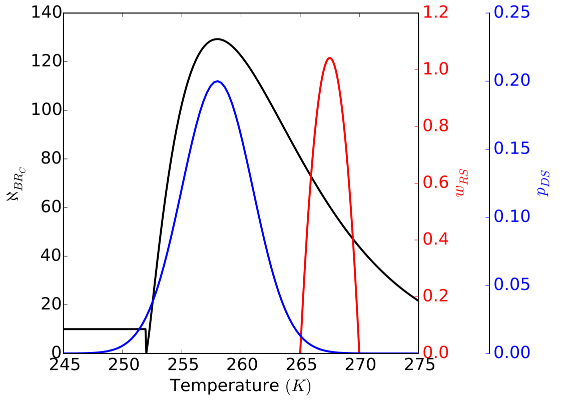

Figure 3.2: Temperature dependent parts of the SIP parameterizations. Black is the fragment generation function of the collisional breakup reference simulation BR_C, blue is the droplet shattering probability function and red is the temperature weighting function for rime splintering.

Table 3.3: SIP relevant parameters.

	Rime Splintering		
RS:	$\aleph_{RS} = 3.5 \times 10^{8}\,(\mathrm{kg} \cdot \mathrm{rime})^{-1}$,	$w_{RS}(T) =$ triangular $(T_{min} = 265\,\mathrm{K},\ T_{opt} = 268\,\mathrm{K},\ T_{max} = 270\,\mathrm{K})$	
	Droplett Shattering		
DS:	$\aleph_{DS} = 10$,	$T_{\mu} = 258\,\mathrm{K}, \quad \sigma = 3\,\mathrm{K}, \quad p_{max} = 0.2$	
	Collisional Breakup		
BR$_\mathbf{C}$:	$F_{BR_C} = 50$,	$T_{min} = 252\,\mathrm{K}, \quad \gamma = 5$	
BR$_\mathbf{V}$:	$F_{BR_V} = \ \ 6.2701, \ \ 5.7271, \ \ \ 25.1816$	$T_{min} = 252\,\mathrm{K}, \quad \gamma = 5$	(cold air outbreak)
	$F_{BR_V} = 56.6518, \ \ 6.6567, \ \ 164.0184$	$T_{min} = 252\,\mathrm{K}, \quad \gamma = 5$	(simp. strat. cloud)
	(coll.: $\quad s+s, \quad g+g, \quad s+g/h \ $)		
	$(F_{BR} = 10, \quad T < 252K)$		

4 Simulations

In this study the cases of two mixed-phase low-level clouds are simulated and analyzed in respect of their sensitivity to SIP. This chapter contains the description of the synoptic conditions of the two chosen cloud cases and the model setups.

4.1 General Set-Up and Grid Structure

As described in section 2.2 the model used for simulating the cloud cases is the ICON model, which can be highly individualized. This section shall serve as a short overview over most of the settings, that are used in general. The more case specific preferences, that mainly concern the synoptic conditions are highlighted in sections 4.2.1 and 4.2.2.

All simulations are set-up for a total duration of 48 hours, although, in many cases the end is not reached because the model terminates after vertical instability occurs. The basic time step used for the fast-physics processes is set to 0.5 s.

In all Simulations, the same grid structure was used. The domain consists of 50 cells in longitudinal and 100 cells in latitudinal direction with a resolution of 100 m. The atmosphere consists of 100 levels, reaching an amplitude of 20 000 m, using the Smooth Level Vertical coordinate scheme (SLEVE, Schär et al. [2002], Leuenberger et al. [2010]). The lowest layer starts with a thickness of 20 m, which than increases for each next layer, with a stretching factor of 0.9, that increases the layer thickness at the top of the model. The model domain is assumed to be a plane torus.

In order to stabilize the simulations a Rayleigh damping height of 4000 m with a Rayleigh coefficient of 0.1 is chosen to reduce vertical wind above the cloud, while from 5000 m upward no moist processes are allowed and the roughness length is 0.001 m.

The radiation scheme used is the *Rapid Radiative Transfer Model* from Mlawer et al. [1997], with a time step of 300 s. Smagorinski diffusion is used. Grid-scale clouds and the atmosphere above model height is included into the radiation calculation scheme. Incoming solar radiation is assumed to have a zenith angle of 0 for the whole duration of the simulations.

Note, that for the aerosol concentrations the default settings of ICON are used. These are prescribed global constant values and do not reflect the true situations observed during the field campaigns. Future studies can enhance the realism of the simulations but this is beyond the scope of the current work.

Other non default settings include the following: For both cases no surface schemes but fixed surface fluxes are used. Forcing of dynamics and transport is set to NWP forcing. And calculation of large scale tracer transport is turned on for a total of fife tracers. Furthermore, there is no diffusion on the vertical wind field. Convection is not parameterized but resolved directly. And the coriolis force is turned of.

4.2 Observational Basis

The two model setups are based on two cases of single layer arctic mixed-phase clouds that where observed over the Beaufort Sea, adjacent to the northern coast of Alaska, between Oliktok Point and Barrow. Figure 4.1 shows an satellite image of the Beaufort Sea and northern Alaska during a cold air outbreak. It was taken during the M-PACE field campaign in fall 2004. Black dots indicate the ground-based remote sensing sites Barrow and Oliktok Point. From both locations aircraft measurements were made of vertical profiles for particle size distributions, total condensate, and liquid water content [Klein et al., 2009].

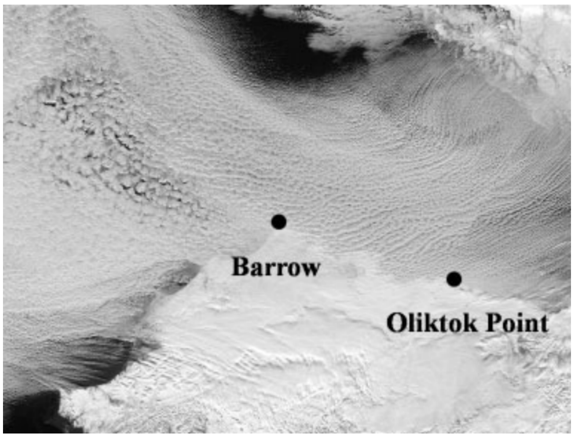

Figure 4.1: Satellite image of the North Slope of Alaska and the adjacent Beaufort Sea. The black dots indicate the to observation sites from where aircraft measurements were started during the ISDAC (Barrow) and M-PACE (Barrow, Oliktok Point) field campaigns. The visible cloud-streets belong to a cold air outbreak that occurred on 9 October 2004.

Based on the experiences of M-PACE, ISDAC, another large field campaign, was conducted during spring 2008 in Barrow. Again surface based remote sensing measurements were performed alongside aircraft in situ flights northward over the Beaufort Sea [McFarquhar et al., 2011].

4.2.1 ISDAC

Synoptic Situation

A simple single-layer stratocumulus deck on 26 April 2008 was chosen for this study.

Here a high pressure system over the arctic ocean created a single layer stratocumulus deck over the Beaufort Sea, that was covered with broken sea ice. The thin ice inhibited surface heat fluxes, decoupling surface and mixed-phase layers, and stabilizing the cloud structure for 15 h [Ovchinnikov et al., 2014].

Measured aerosols included mainly organic particles, a large portion of sulfates, little biomass from burning and sea salt. For a more thorough discussion refer to McFarquhar et al. [2011].

Model Set-up

An intercomparison study by Ovchinnikov et al. [2014] on large-eddy simulations of arctic mixed-phase clouds observed during the ISDAC field campaign serves as a guiding concept for the model set-up of one of the cloud cases in this study. Simulations are initialized with the following initial profiles of liquid water potential temperature $\theta_{l,0}(z)$, water vapor $q_{v,0}(z)$, and horizontal wind components $u_0(z)$ (zonal) and $v_0(z)$ (meridional):

$$\theta_{l,0}(z) = \begin{cases} 265 + 0.004\,(z-400) & [\mathrm{K}], \quad z < 400\,\mathrm{m} \\ 265 & [\mathrm{K}], \quad 400\,\mathrm{m} \leq z < 825\,\mathrm{m} \\ 266 + (z-825)^{0.3} & [\mathrm{K}], \quad 825\,\mathrm{m} \leq z < 2045\,\mathrm{m}, \\ 271 + (z-2000)^{0.33} & [\mathrm{K}], \quad 2045\,\mathrm{m} \leq z \end{cases} \tag{4.1}$$

$$q_{v,0}(z) = \begin{cases} 1.5 - 0.00075\,(z-400) & [10^{-3}\,\mathrm{kg\,K^{-1}}], \quad z < 400\,\mathrm{m} \\ 1.5 & [10^{-3}\,\mathrm{kg\,K^{-1}}], \quad 400\,\mathrm{m} \leq z < 825\,\mathrm{m} \\ 1.2 & [10^{-3}\,\mathrm{kg\,K^{-1}}], \quad 825\,\mathrm{m} \leq z < 2045\,\mathrm{m}, \\ 0.5 - 0.000075\,(z-2045) & [10^{-3}\,\mathrm{kg\,K^{-1}}], \quad 2045\,\mathrm{m} \leq z \end{cases} \tag{4.2}$$

$$u_0(z) = -7 \qquad [\mathrm{m\,s^{-1}}], \tag{4.3}$$

$$v_0(z) = -2 + 0.003\,z \qquad [\mathrm{m\,s^{-1}}], \tag{4.4}$$

with z being the altitude above the ocean.

Figures 4.2a and 4.2b show the initial temperature and moisture profiles respectively. One can see, looking at the potential temperature profile, that the part of the boundary layer below 400 m

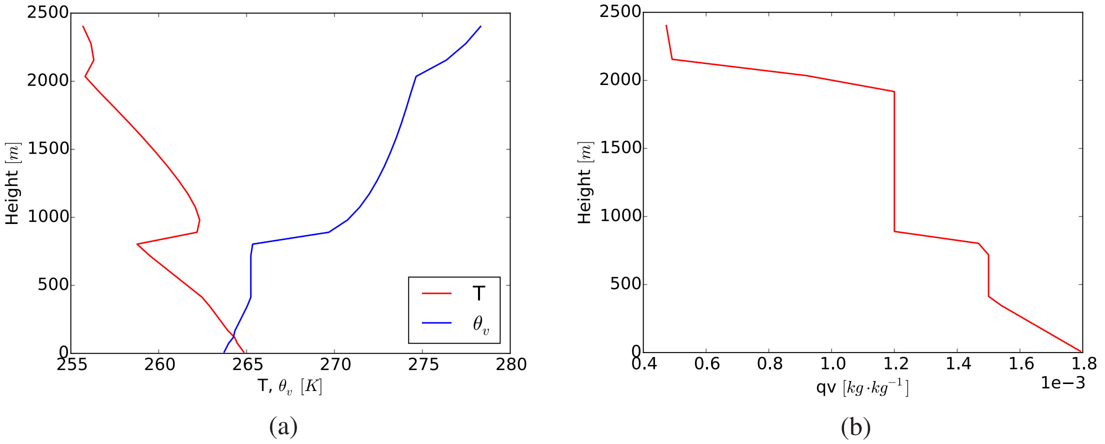

(a) (b)

Figure 4.2: Initial soundings used for the ISDAC case. a) Temperature (red) and liquid water potential temperature (blue). b) Initial water vapor mass mixing ratio profile.

is quite stable. This is consistent with the very small surface sensible ϕ_s and latent ϕ_l heat fluxes. In this study these are neglected for the ISDAC case:

$$\phi_s = \phi_l = 0\,\mathrm{W\,m^{-2}}. \tag{4.5}$$

The strong inversion in 825 m contains the analyzed stratiform cloud. It should be pointed out, that the temperature profile shows a second, smaller inversion at 2045 m, where a second cloud forms after 15 hours, when the lower inversion dissolves. This is no surprise, since during ISDAC several multilayer clouds were observed.
Furthermore, no sea surface temperature is defined, totally decoupling the ocean from the boundary layer. The starting temperature of the lowermost atmospheric level is 265 K.
Note, that these figures show the very first time step of the profiles. All cloud water is assumed to be vapor upon initiation of the simulation. The model then immediately calculates the condensation from supersaturation, that leads to cloud formation. I.e. in this step water is redistributed from water vapor to condensed particles, that can be seen in the profiles as little distortions around the inversion layers at 825 m and to a lesser extent at 2045 m.
Surface pressure is assumed to be 1020 hPa.

Ovchinnikov et al. [2014] suggests a large scale forcing of horizontal wind divergence below the initial inversion layer, resulting in a linearly increasing subsidence from zero at sea level to a constant downwelling above the inversion.
However, this could not be accomplished for these experiments, since large scale forcing resulted in considerable instability of the model, that could not be solved within the scope of this study.

A simple radiation scheme is used, where the short wave solar irradiance is set to a neglectable value to prohibit interference. Long wave radiation however is turned on to allow cloud top evolution to some extent.

4.2.2 M-PACE

Synoptic Situation

On 9 October 2004 an cold-air outbreak was observed during M-PACE. A high pressure system over the arctic ice to the north-east of Alaska resulted in strong winds over the ice free ocean of the southern Beaufort Sea towards the coast. With decreasing temperatures the ice grew steadily southward, cooling the air above it further. While the air flew over the edge of the pack ice onto the free ocean the warmer surface temperature induced large surface fluxes, resulting in a well-mixed boundary layer. This again resulted in boundary layer stratocumuli, shaped like cloud-streets, which are typical for cold air outbreaks (Klein et al. [2009] and Verlinde et al. [2007]).
The aerosol picture was somewhat cleaner than in the ISDAC case, what is common for this time of year [Jackson et al., 2012]. Although, information on aerosol composition is not available, preceding observations by Fridlind et al. [2000] suggest a pure ammonium bisulfate composition.

Model Set-up

The model set-up of the M-PACE case is based on an intercomparison study by Klein et al. [2009] and the procedure is the same as with the ISDAC case. However, initial liquid water potential temperature $\theta_{l,0}(P)$ and water vapor $q_{\mathrm{v},0}(P)$ are given in terms of pressure vertical coordinates:

$$\theta_{l,0}(P) = \begin{cases} 269.2 & [\mathrm{K}], \quad P \leq 850\,\mathrm{hPa} \\ 275.33 + 0.0791(815 - P) & [\mathrm{K}], \quad 850\,\mathrm{hPa} < P, \end{cases} \tag{4.6}$$

$$q_{\mathrm{v},0}(P) = \begin{cases} 1.95 & [10^{-3}\,\mathrm{kg\,K^{-1}}], \quad P \leq 850\,\mathrm{hPa} \\ 0.291 + 0.00204(P - 590) & [10^{-3}\,\mathrm{kg\,K^{-1}}], \quad 850\,\mathrm{hPa} < P. \end{cases} \tag{4.7}$$

Before implementation, they have to be converted to the ICON internal geometric coordinates. From the barometric formula and the definition of potential temperature:

$$dz = -\frac{R_d}{g}\frac{T(P)}{P}\,dp, \tag{4.8}$$

$$\theta = T\left(\frac{P_0}{P}\right)^{R_d/c_P}, \tag{4.9}$$

the following expression for the geometric height can be derived:

$$z = \begin{cases} -\frac{\theta_{l,0}\;c_P}{g}\,P_0^{-R_d/c_P}\left(P^{R_d/c_P} - P_s^{R_d/c_P}\right) & [\mathrm{m}], \quad P \leq 850\,\mathrm{hPa} \\ -\frac{R_d\;c_P}{g}\,P_0^{-R_d/c_P}\left(\frac{339.8}{R_d} - \frac{0.0791}{R_d+1}(P - P_s)\right)\left(P^{R_d/c_P} - P_s^{R_d/c_p}\right) & [\mathrm{m}], \quad 850\,\mathrm{hPa} < P, \end{cases} \tag{4.10}$$

with the gas constant $R_d = 287.1\,\mathrm{J\,kg^{-1}\,K^{-1}}$ and specific heat capacity $c_P = 1003.5\,\mathrm{J\,kg^{-1}\,K^{-1}}$ of dry air, the gravitational acceleration $g = 9.8067\,\mathrm{m\,s^{-2}}$, a reference pressure $P_0 = 1000\,\mathrm{h/Pa}$, and the surface pressure $P_s = 1010\,\mathrm{h/Pa}$.
This translates the inversion pressure $P_{inv} = 850\,\mathrm{hPa}$ to a height of $z_{inv} \approx 1330\,\mathrm{m}$.
Initial horizontal wind components u_0 (zonal) and υ_0 (meridional) are not height dependent:

$$u_0 = -13 \quad [\mathrm{m\,s^{-1}}], \tag{4.11}$$

$$\upsilon_0 = -7 \quad [\mathrm{m\,s^{-1}}]. \tag{4.12}$$

In figure 4.3a and 4.3b again the sounding profiles are shown. Apart from the higher inversion layer, a few more things appear to differ from the ISDAC case. First, the boundary layer is less stable, indicated by the steep potential temperature. Second, the surface layer temperature starts 5 K higher, while the temperature in the inversion layer is slightly lower. This is probably due to the warmer ocean warming the air, while the greater height of the boundary layer leads to

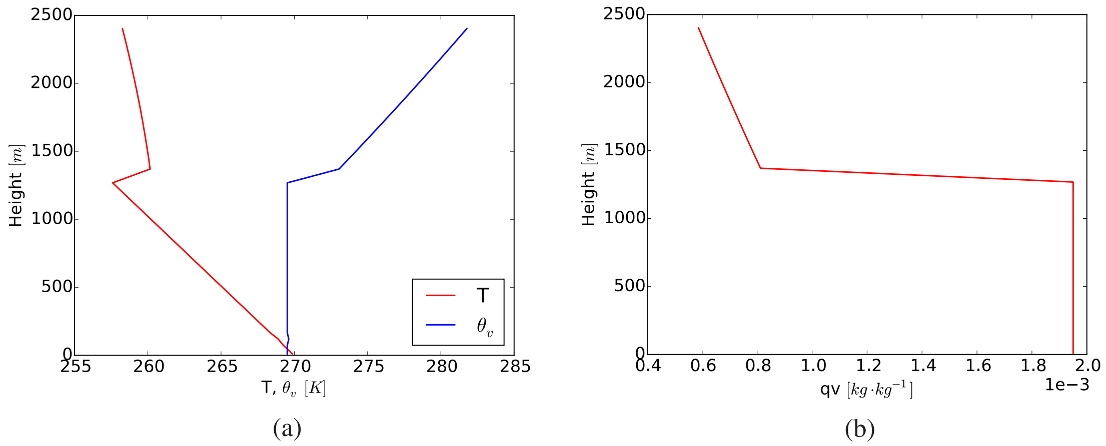

Figure 4.3: Initial soundings used for the M-PACE case. a) Temperature (red) and liquid water potential temperature (blue). b) Initial water vapor mass mixing ratio profile.

cooler top layer temperatures. In combination with the high surface fluxes, as announced in the preceding section:

$$\phi_s = 136.5\,\mathrm{W\,m^{-2}}, \tag{4.13}$$

$$\phi_l = 107.7\,\mathrm{W\,m^{-2}}, \tag{4.14}$$

the boundary layer is assumed to be more turbulent and the inversion layer expected to rise faster. Hence colder subzero cloud temperatures are anticipated.

Horizontal wind speeds are somewhat larger on initialization, but die down over time, due to friction at the surface in both cases.

Large scale forcing is not available either. And the radiation scheme is the same as in the ISDAC case.

5 Results and Discussion

In this chapter the results of this study are discussed. It starts with a general first impression of the evolution of the cloud. Then a closer look is taken at different variables, like LWC, IWC, ICNC, and their reaction to the sensitivity simulations. Eventually, the SIP rates are analyzed in regard of their sensitivity on different conditions.
Note, that the sensitivity experiments on the M-PACE cloud case experienced large model instability depending on the active SIP mechanisms. Hence, for many parts of the following discussion the interpretation of results is possible for different time intervals. Most of the analysis are reduced to ten hours of simulation time, cutting of large parts of available output from more stable simulations. Nevertheless, longer analysis can be made for occasional comparisons of fewer sensitivity simulations.

In total, 24 simulations exist for both cloud cases, twelve each. These consist of all eight possible combinations of SIP mechanisms. The simulations including collisional breakup again are subdivided into two sets of sensitivity experiments. One set is based on the original Sullivan et al. [2018] scheme with a constant leading factor F_{BR_C}. In the other F_{BR_V} is adjusted for each collision type, based on the findings of Phillips et al. [2017], as described in section 3.2.3. An overview over all experiments is given in table 5.1.

Table 5.1: Overview over all simulations. The prescribed superscript indicates the cloud case, the information inside parentheses the combination of active SIP mechanisms. Simulations without SIP are indicated as SIP_{off}, simulations including all three processes as SIP_{on}.

ISDAC		M-PACE	
$^{I}(SIP_{off})$		$^{M}(SIP_{off})$	
$^{I}(RS)$		$^{M}(RS)$	
$^{I}(DS)$		$^{M}(DS)$	
$^{I}(BR_C)$	$^{I}(BR_V)$	$^{M}(BR_C)$	$^{M}(BR_V)$
$^{I}(RS+DS)$		$^{M}(RS+DS)$	
$^{I}(RS+BR_C)$	$^{I}(RS+BR_V)$	$^{M}(RS+BR_C)$	$^{M}(RS+BR_V)$
$^{I}(DS+BR_C)$	$^{I}(DS+BR_V)$	$^{M}(DS+BR_C)$	$^{M}(DS+BR_V)$
$^{I}(SIP_{on,BR_C})$	$^{I}(SIP_{on,BR_V})$	$^{M}(SIP_{on,BR_C})$	$^{I}(SIP_{on,BR_V})$

The simulations are named after the combination of active SIP processes and the first letter of the cloud cases, i.e. I for ISDAC and M for M-PACE. If there are no active SIP processes the label is SIP_{off}, if all mechanisms are active it is SIP_{on}. $^{I}(SIP_{off})$ and $^{M}(SIP_{off})$ are also called control runs from here on.

5.1 Time Evolution of the Mixed-Phase Clouds

Before discussing individual simulations and specific microphysical effects, a general overview of the development of the mixed-phase clouds is given. For illustration purposes the control runs $^{I}(SIP_{off})$ and $^{M}(SIP_{off})$ are chosen exemplarily.

5.1.1 ISDAC

For the ISDAC case the vertical cloud evolution of the $^{I}(SIP_{off})$ run is illustrated in figure 5.1 and the development of vertically integrated and horizontally averaged mass mixing ratios of all hydrometeors is shown in figure 5.2.

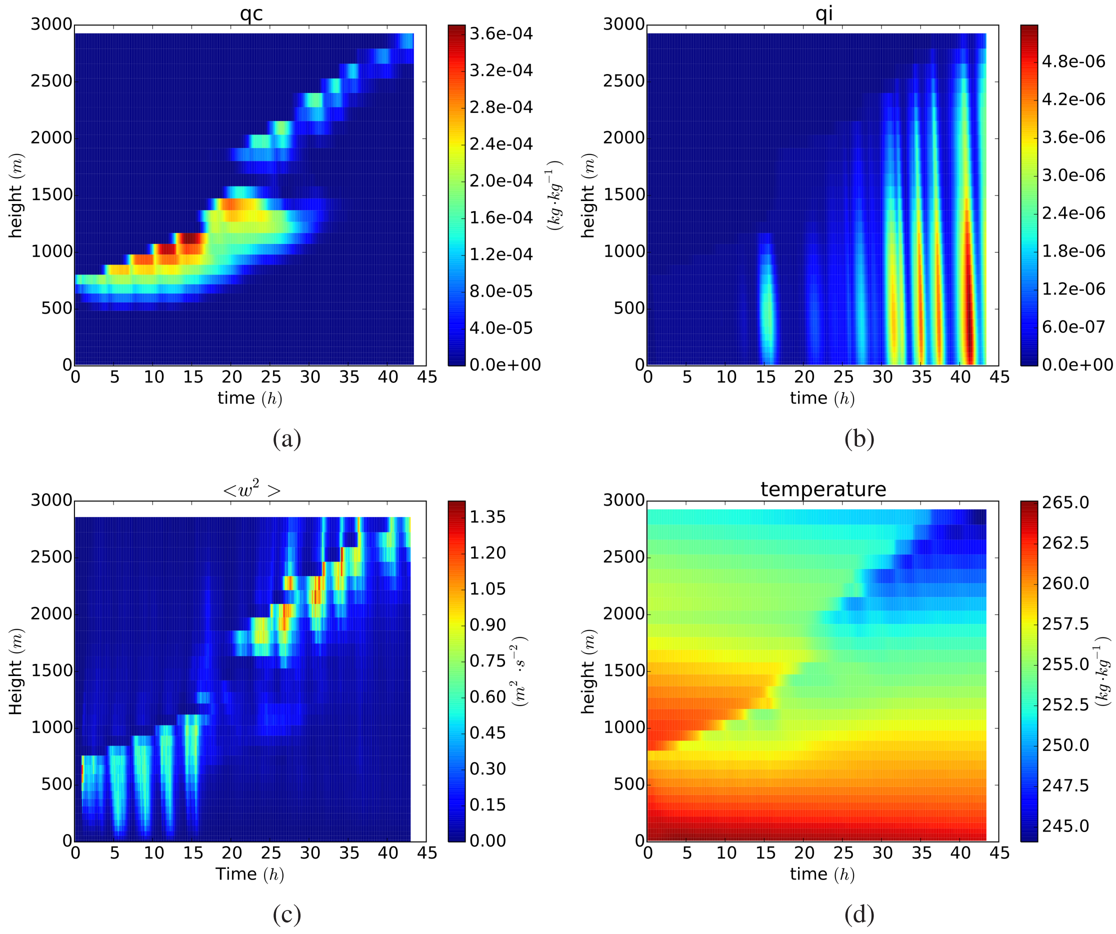

(a) (b)

(c) (d)

Figure 5.1: Time evolution of vertical profiles of the ISDAC horizontal mean LWC (a) and IWC (b) as well as the variance of vertical velocity $< w^2 >$ (c) and temperature (d) for the control run $^{I}(SIP_{off})$. Only the first 22 height levels are shown. the color bars of the LWC and IWC image differ in around two orders of magnitude. Little production of ice crystals is already happening after half an hour, but is hardly visible in figure b).

In this cloud case cloud droplets form around the inversion layer right after the simulation starts. This is due to supersaturation with respect to liquid water, that leads to the formation of a stratified

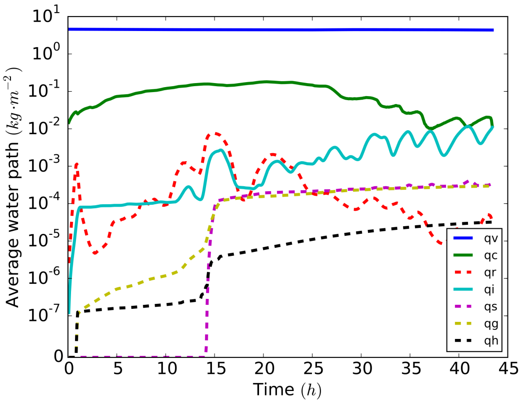

Figure 5.2: Time evolution of the horizontal mean and vertically integrated mass for all hydrometeors of the ${}^{I}(SIP_{off})$ run. Water vapor is also included.

cloud with little change in composition over up to 15 hours, except for a small time interval, before an hour has passed, where rain is formed, sediments and freezes partly. While cloud top radiative cooling slowly thickens the cloud layer, temperature sinks and steadily increase the amount of condensate. The cloud top rises about 400 m in 15 hours.

There is a very small amount of ice and even less graupel and hail produced, starting after half an hour when rain drops freeze. Those steadily precipitate and reach the ground one hour from simulation start and then continue to do so. Note, that this is hardly visible in figure 5.1b, since the amount of ice crystals is so small, compared to later times, but can be observed in figure 5.2. Turbulence seemingly is generated mainly from falling rain and graupel, affecting the boundary layer from ground to barely below cloud top.

After around 15 hours ice, graupel, and hail production experiences a short boost, again from a strong rain freezing event. At the same time snow is forming abruptly, due to riming, which is enhanced by the increase in ice crystals and rain. This is also where the mass of cloud droplets reach its maximum.

From around 17 to 20 hours the cloud top then rises dramatically more than 100 m per hours, because the inversion strength by then is largely reduced. This is apparent in figure 5.1d, where the hard temperature gradient of the inversion is visibly dissolved around 20 hours. As pointed out in section 4.2.1, a second cloud layer then forms around 250 m above the first, where the second inversion is located. This cloud layer then rises steadily due to radiative cooling, gets more turbulent and produces frozen particles, while the remnant liquid cloud water below slowly depletes.

Comparing ${}^{I}(SIP_{off})$ and ${}^{I}(SIP_{on,BR_C})$, there is not much macroscopic evidence for a strong impact of SIP, that is why the latter is not separately shown. The only noteworthy difference is an increase of hail and a decrease of graupel mass mixing ration, that is caused by the change of fragment numbers during rain drop freezing. This ultimately effects the redistribution of frozen rain mass to the three involved particle classes, ice, graupel, and hail (see section 3.2.2 for a more thorough explanation).

For the subsequent analysis the main focus shall be laid on the first 15 hours of the simulations where the cloud is more stratified.

5.1.2 M-PACE

The M-Pace case looks different in several regards, while some features can be recognized from before. Figure 5.3 again shows the vertical evolution of different cloud properties for $^M(SIP_{off})$.

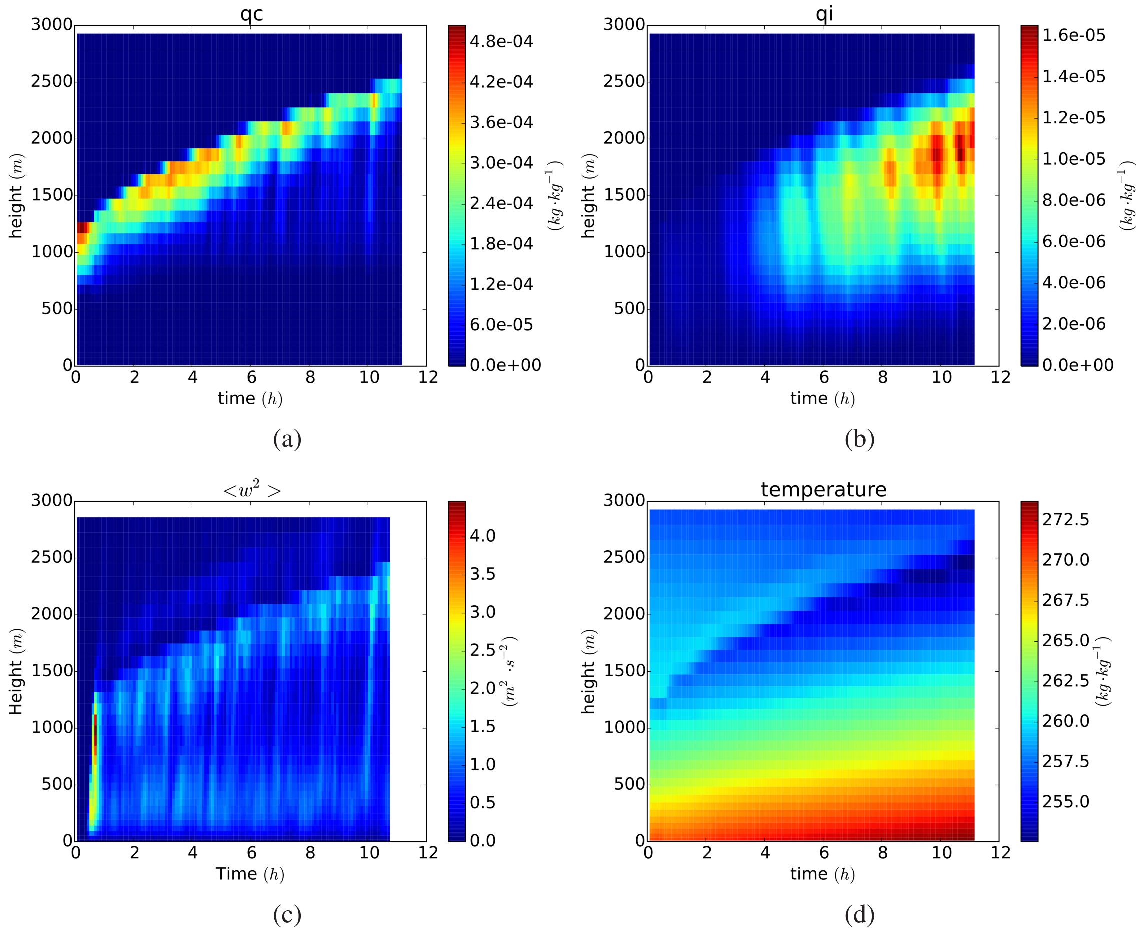

(a)

(b)

(c)

(d)

Figure 5.3: Time evolution profiles of the M-PACE horizontally mean LWC (a) and IWC (b) as well as the variance of vertical velocity $< w^2 >$ (c) and temperature (d) for the control run $^M(SIP_{off})$. Only the first 22 height levels are shown. The color bars range of LWC and IWC differ in around one and a half orders of magnitude.

Right from simulation start, there is a high concentrated liquid cloud present at the inversion layer. After a couple of minutes, rain drops form, sediment and freeze, like before in the ISDAC case. That again leads to ice, graupel and hail formation, as can be taken from the evolution of horizontal mean of vertically integrated particle mass mixing ratios in figure 5.4.

As expected, the rise of the cloud top is enhanced by the strong surface latent and sensible heat fluxes. This influence can be seen in figure 5.3d. There the transfer of heat from the surface to the atmosphere and a change over time in the temperature gradient in the lower part of the boundary layer can be seen. Generally speaking this cloud develops faster and produces more particles of every class than the ISDAC case.

Figure 5.3c shows the vertical velocity variance. Once again turbulence is created by precipitation, especially at the beginning, where a lot of rain is formed. After that cloud top cooling also contributes at the upper part of the boundary layer.

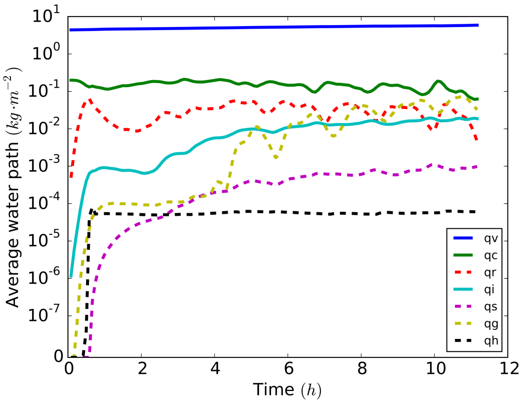

Figure 5.4: Time evolution of the horizontal mean and vertically integrated masses for all hydrometeors of the ${}^{M}(SIP_{off})$ run. Water vapor is also included.

The question, how the cloud develops after more than 10 hours, can not be addressed using the provided images. However, one run with collisional breakup only was able to sustain stability for about 25 hours (see figures 5.5a and 5.5b for LWC and IWC respectively). What immediately

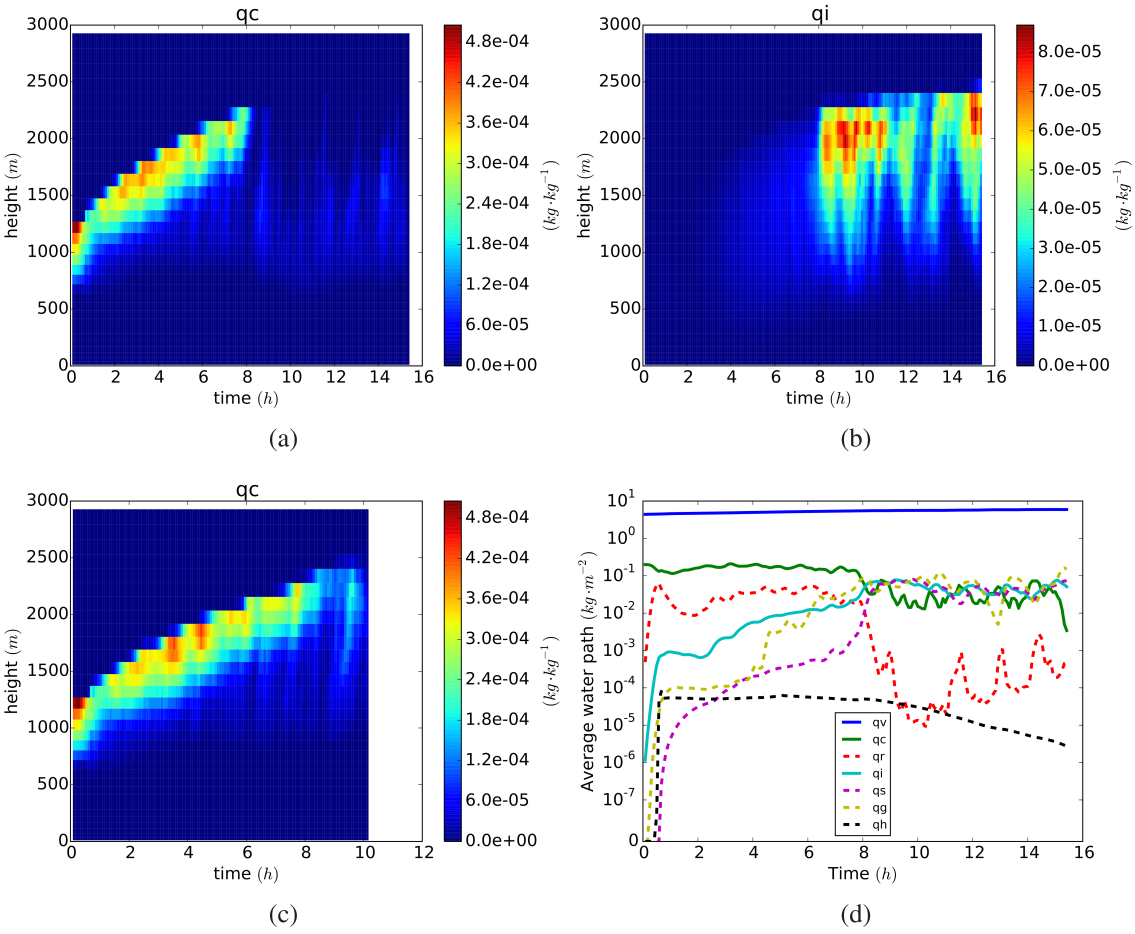

(a) (b)

(c) (d)

Figure 5.5: Time evolution of vertical profiles of the M-PACE horizontal mean LWC (a) and IWC (b) for the ${}^{M}(BR_{C})$ run, and LWC (c) for the ${}^{M}(SIP_{on,BR_{C}})$ run. d) Time evolution of the horizontal mean of vertically integrated masses for all hydrometeors of the ${}^{M}(BR_{C})$ run. Water vapor is also included.

stands out, is the reduction in cloud droplet mass even before the 10 hour mark. This may be less extreme, than it appears, given the applied colormap of the plots. Yet, from the development of the horizontal mean of vertically integrated number concentrations (figure 5.5d) an average reduction of cloud droplet mass of one order of magnitude can be extracted. A weaker reduction is arguably also happening in the $^{M}(SIP_{on,BR_C})$ run (figure 5.5c) but not in the $^{M}(SIP_{off})$ run (refer again to figure 5.3a). Although, this is not indisputable, since the simulation cuts short where the development should be decisive.
Nevertheless, the short amount of simulated time of the M-PACE case should still be sufficient to get valuable insights into SIP processes in these kind of clouds.

Note the difference in frozen particle masses present in the two cloud cases (compare figures 5.2 and 5.4). It will be shown later, that this may lead to different SIP sensitivities, especially to collisional breakup rates.

5.2 Liquid and Ice Water Path

Since this study is concerned with mixed-phase clouds it suggests itself to take a look into the partitioning of the liquid and frozen phases. A first impression concerning particle mass development of the control runs $^{I}(SIP_{off})$ and $^{M}(SIP_{off})$, has already been given in figures 5.2 and 5.4 of the preceding section 5.2.
The focus in this section lies on the comparison of the liquid and ice water paths of the sensitivity experiments, excluding simulations with BR_V implementations for now. An analysis of the differences between the two collisional breakup variants follows later in section 5.3.

5.2.1 ISDAC

The time series of horizontally averaged LWP and IWP for the ISDAC sensitivity experiments are shown in figure 5.6a and 5.6b respectively.

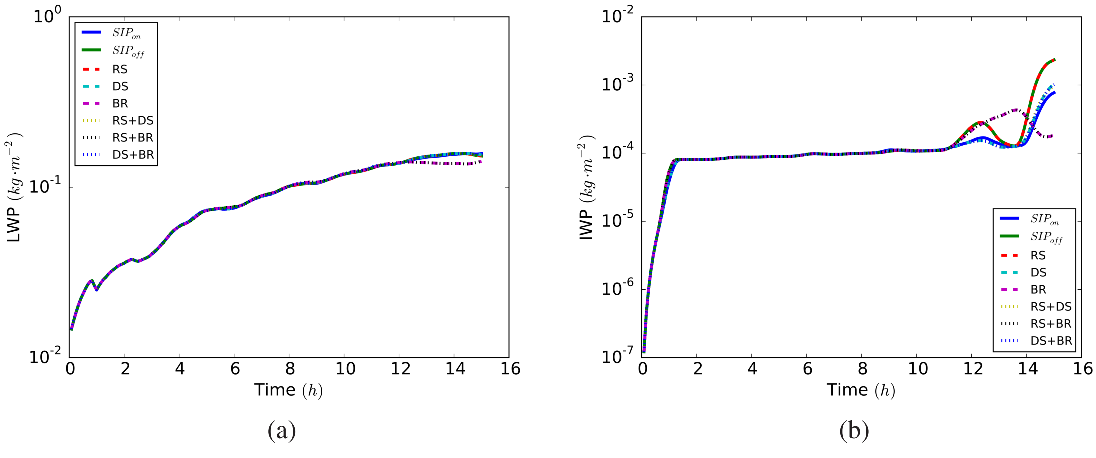

(a) (b)

Figure 5.6: Time series of the first 15 hours of horizontally averaged LWP (a) and IWP (b) for the ISDAC case. For the collisional breakup process the constant variant BR_C was used.

There is an increase in LWP in all simulations of about one order of magnitude from start up until the 15 hour mark, where it reaches its maximum of approximately $2 \times 10^{-3}\,\mathrm{kg\,m^{-2}}$. The results yield little to no impact of SIP on LWP in the timeframe of the simulations. The slight difference of LWP after around 13 hours in the simulations involving collisional breakup is of minor extend. However, the $^{I}(SIP_{on})$ simulation does not exhibit the same behavior, while an active collisional breakup process is included. Regarding the IWP development, the slight distortion caused by collisional breakup is again visible, though it seems to simply delay a change in IWP that is already occurring in the $^{I}(SIP_{off})$ run.

As expected, the increasing fragment number from rain freezing due to droplet shattering, changes the redistribution into the frozen categories, effecting IWP. This process is coupled only to the freezing of rain, but not of cloud droplets, hence there is no indication in the LWP picture. Interestingly, there appears to be no effect of droplet shattering during the first freezing event half an hour after simulation start, which could be due to the generally lower particle concentrations.

Rime splintering has no clearly visible influence in any regard. However, that is to be expected, because of the cold temperatures of the cloud, outside the sensitivity range of $-3\,^{\circ}\mathrm{C}$ to $-8\,^{\circ}\mathrm{C}$.

5.2.2 M-PACE

Figures 5.7a and 5.7b show the average LWP and IWP of the M-PACE sensitivity experiments. In contrast to the ISDAC case, the individual simulations differ more and LWP begins to diverge already after three hours. However, LWP development in all simulations stays approximately in the same range around $0.5 \times 10^{-3}\,\mathrm{kg\,m^{-2}}$, with a slight decreasing tendency. The only exception, one could argue, is again collisional breakup, as a stronger decreasing tendency can be surmised at the eight hour mark. Fortunately, longer simulations are available for the control run and all runs involving collisional breakup, that are shown in figure 5.8.

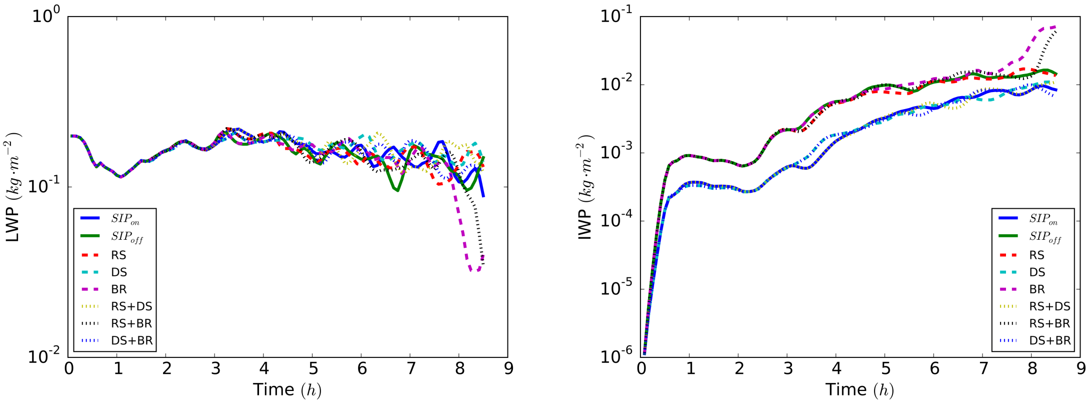

(a) (b)

Figure 5.7: Time series of horizontally averaged LWP (a) and IWP (b) for the M-PACE case. For the collisional breakup process the constant variant BR_C was used.

There the impact of collisional breakup is clearly visible, decreasing LWP by almost one order of magnitude and increasing IWP by a slightly less extended but still distinctive margin. However, additionally involvement of droplet shattering seems to strongly compensate this effect in case of LWP and even hinders the IWP to match the control run.

This is a very distinctive change, where droplet shattering leads to a complete underdevelopment

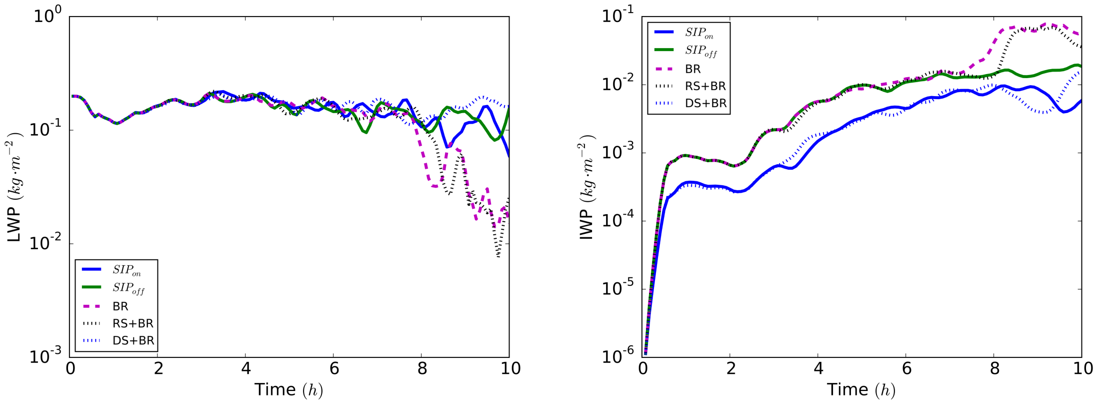

(a)

(b)

Figure 5.8: Time series of horizontally averaged LWP (a) and IWP (b) for the M-PACE and simulations involving the constant collisional breakup variant BR_C.

compared to the control run. This is already caused in the first hour and lasts throughout the simulations. Therefore this process has a very large impact on the overall IWP magnitude.

In section 5.3 it will be shown, that an active droplet shattering process lowers not only the amount of ice, but also of graupel and snow, that may lead to a reduced impact of collisional breakup.

This effect is not at all expected, since droplet shattering should increase ice crystal numbers. The redistribution of fragments into the three frozen particle classes ice, graupel and hail, should actually result in more ice, because more fragments means more smaller particles that fall below the ice-graupel distinction limit (see again section 3.2.2 for information on the redistribution of frozen droplets). But what happens in these simulations is essentially the opposite. Hail concentration increases while the other classes decrease.

Unfortunately, this issue could not be thoroughly investigated in the scope of this study and has to be addressed separately.

5.2.3 Liquid-Ice Partitioning

To compare the liquid and frozen fractions of the clouds, vertically integrated horizontally mean particle masses are averaged over time intervals where they stay considerably constant. For the ISDAC cloud that is between ten and fourteen hours, and for the M-PACE cloud between five and eight hours. Table 5.2 summarizes the results.

It is apparent, that the cloud from the M-PACE case produces considerably more ice than the stratiform cloud regime in the ISDAC case. The mean liquid to ice ratios are 8.7 and 634.8 respectively. The large difference may be due to the stronger dynamics as well as the colder cloud top temperatures in the M-PACE case. In association with the larger amount of water vapor, that is available in the M-PACE case, this also leads to more total condensate.

Comparing the sensitivity simulations among the cloud cases themselves, one finds relatively larger influences in the more dynamic system. Especially the droplet shattering process in the M-PACE case seems to lead to slower glaciation of the cloud, almost doubling the liquid to ice ratio. The ISDAC cloud reacts with stronger icing to every SIP process except rime splintering, that appears to have no impact at all.

Table 5.2: Liquid-Ice partitioning of ISDAC and M-PACE simulations, as well as average amount of total condensate. The ratios are calculated from horizontally and time-wise averaged, vertically integrated particle masses. The amount of total condensate is given in $(\mathrm{kg\,m^{-2}})$ and calculated as the sum of all six hydrometeor masses.

	ISDAC		M-PACE	
	Liquid-Ice Ratio	Total Condensate	Liquid-Ice Ratio	Total Condensate
(SIP_{off})	819.8	0.1412	6.9	0.2109
(RS)	819.8	0.1412	6.5	0.2046
(DS)	585.9	0.1414	12.1	0.2246
(BR_C)	564.3	0.1362	4.6	0.2248
$(RS+DS)$	578.3	0.1413	12.0	0.2115
$(RS+BR_C)$	564.3	0.1362	6.0	0.2142
$(DS+BR_C)$	578.7	0.1414	11.5	0.2139
(SIP_{on,BR_C})	567.6	0.1404	9.8	0.2120

Again the weakening of ice formation caused by droplet shattering in the M-PACE case can be observed. As expected from findings in section 5.2.2 the strongest enhancement of glaciation occurs in the $^{M}(BR_C)$ run.

5.3 Ice Crystal Number Concentration and SIP Rates

This section is concerned with the secondary ice production rates and the time evolution of ice crystal numbers. Therefore the particle concentrations again are vertically integrated and then horizontally averaged. Furthermore a comparative analysis of the two collisional breakup variants ist performed.

5.3.1 ISDAC

In the ISDAC case, the time evolution of ice crystal number concentrations follow very much the first 15 hours of IWP progression from figure 5.6b. They are shown in figure 5.9 for all sensitivity experiments and both collisional breakup versions.

Apart from a slight shift of the $^{I}(SIP_{on})$ runs around twelve hours into the simulation, there is no difference between the collisional breakup variants recognizable. The shift is due to a minor change in rime splintering, as can be seen in figure 5.10, where the secondary ice production rates for individual mechanisms as well as a total rate are shown for the $^{I}(SIP_{on})$ simulations. A smaller ice crystal concentration around twelve hours and the larger one around 15 hours fits the reduced respectively enhanced rime splintering rate of the $^{I}(SIP_{on,BR_V})$ simulation.

However, the missing sensitivity of the cloud to those variants, is obviously due to the missing, or at least vastly limited, collisional breakup process. Going back to figure 5.2, where the vertically integrated particle masses of the ISDAC control run are shown, it becomes clear, that the low

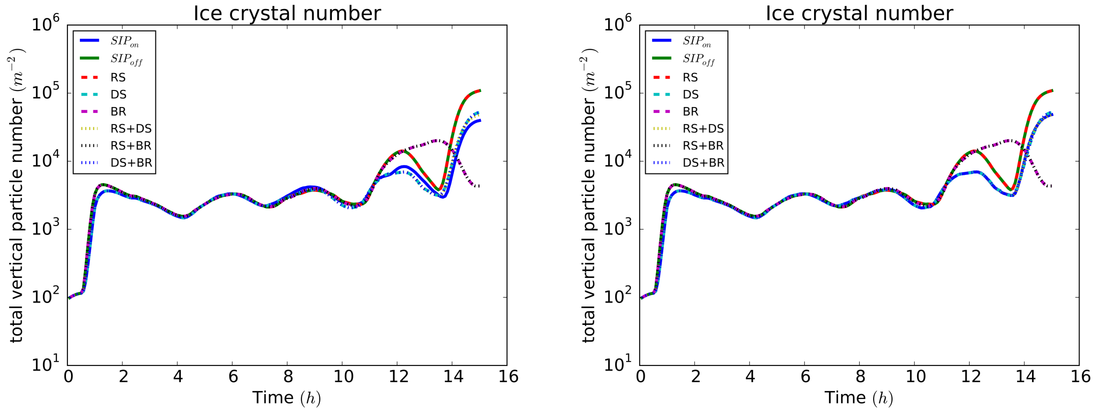

(a) (b)

Figure 5.9: The first 15 hours of horizontal average of vertically integrated ice crystal number concentration for all sensitivity experiments of the ISDAC case. Simulations including the constant variant of collisional breakup BR_C (a) and the variable variant BR_V (b) are shown.

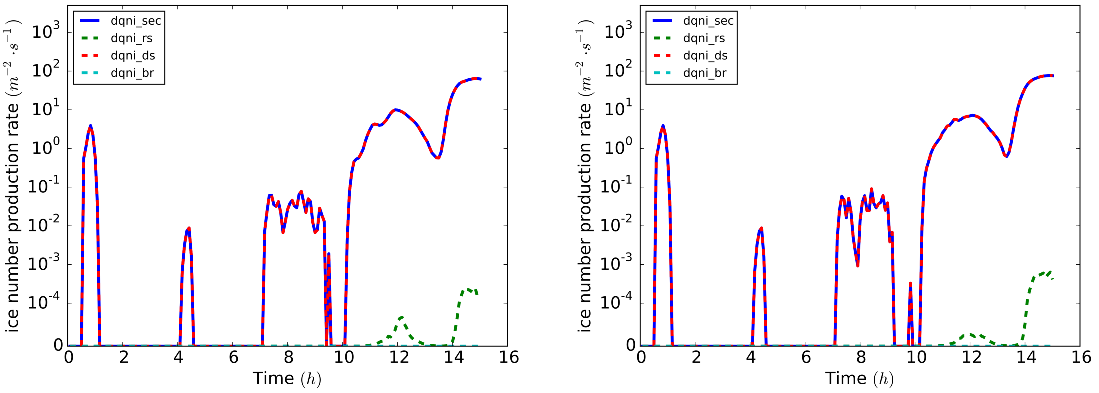

(a) (b)

Figure 5.10: Time series of the first 15 hours of horizontally averaged and vertically integrated SIP rates for $^{I}(SIP_{on,BR_C})$ (a) and $^{I}(SIP_{on,BR_V})$ (b).

amount of frozen particles does not favor particle-particle collisions. It will be shown, that this situation is different in the M-PACE case, leading to distinct features produced by the collisional breakup variants.

The differences in rime splintering rates certainly originate from slight variations of fragment numbers from early collisions, that may have some complex impact in the long run.

5.3.2 M-PACE

In the M-PACE case, the adjustment of the collisional breakup mechanism in the $^{M}(RS+BR_V)$ run leads to a large mitigation of cloud sensitivity to that process. Figure 5.11 shows, that in the $^{M}(BR_C)$ and $^{M}(RS+BR_V)$ runs, contrary to the other variant, there is no drastic change in ice crystal concentration. The difference is more apparent when comparing the collisional breakup rates of both variants directly as shown in figure 5.12.

The variant does not seem to have any other noticeable effect. Especially in the first couple of hours the development of ice crystal numbers is still mainly affected by droplet shattering, as

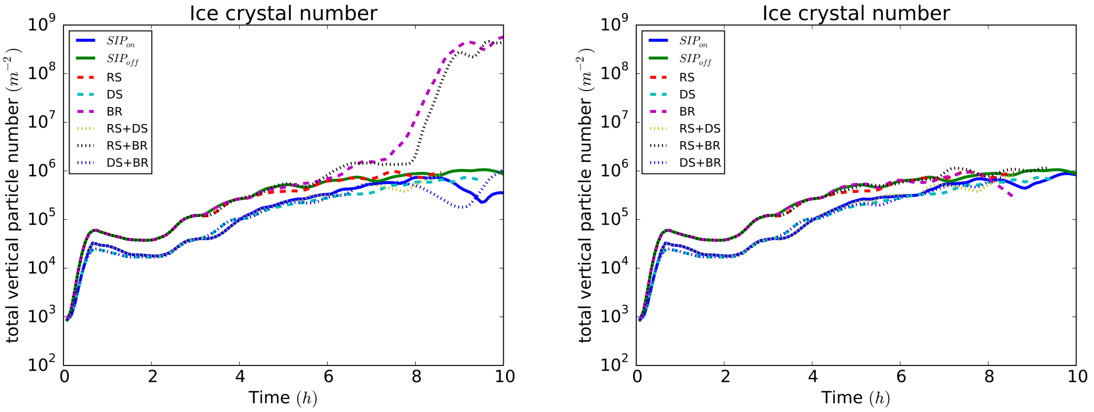

(a)

(b)

Figure 5.11: Horizontal average of vertically integrated ice crystal number concentration for all sensitivity experiments of the M-PACE case. Simulations including the constant variant of collisional breakup BR_C (a) and the variable variant BR_V (b) are shown.

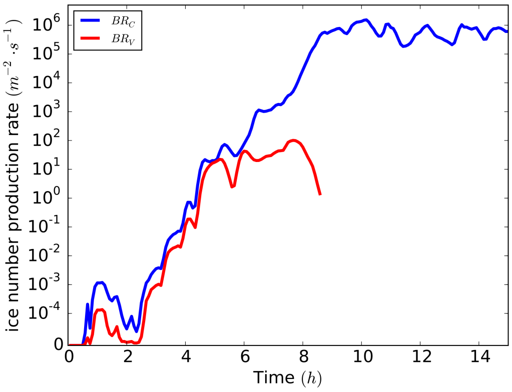

Figure 5.12: Rate of produced fragments through collisional fragmentation for $^M(BR_C)$ (blue) and $^M(BR_V)$ (red). Depicted are the horizontal averages of the vertically integrated generation rates.

discussed before in section 5.2.2.

To understand where this sensitivity difference comes from, a look into the development of all particle numbers is conducive. In figure 5.13 the differences between $^M(BR_C)$ and $^M(BR_V)$ can be seen. The clearly enhanced snow and graupel particles in the $^M(BR_C)$ case explain the strong ascent of the SIP rate around 8 hours into the simulation. Compared to the $^M(BR_V)$ case, there is a difference of around three orders of magnitude for snow and almost one order of magnitude for graupel number concentrations. Ice crystals numbers are also enhanced, but do not contribute to collisional breakup in this study.

Very little changes exist between the $^M(BR_V)$ and $^M(SIP_{off})$ simulations, indicating almost no influence to collisional breakup.

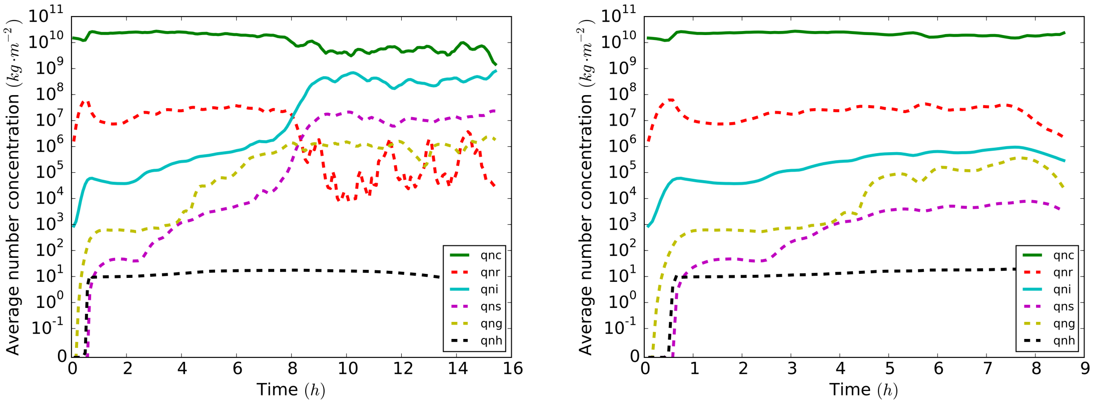

(a) (b)

Figure 5.13: Time evolution of the horizontal mean of vertically integrated particle number concentrations for all hydrometeor and a) $^{M}(BR_C)$ and b) $^{M}(BR_V)$.

5.4 SIP Dependence on Particle Profiles

To investigate where SIP processes occur, vertical profiles of the process rates as well as the vertical distributions of the involved particle classes are shown and analyzed. Additionally, a look into the temperature profiles is taken, since the implemented mechanisms are highly temperature dependent. In the previous sections it became clear, that the strongest sensitivity to SIP is found in the M-PACE case. Especially in simulations using the constant fragment approach for collisional Breakup. To impose interference of other SIP processes, $^{M}(RS)$, $^{M}(DS)$, and $^{M}(BR_C)$ simulations are chosen to address this question for each mechanism separately.

5.4.1 Rime Splintering

Since all types of particles can be involved in a riming processes, the vertical distributions of all classes have to be regarded. Vertical profiles are shown in figure 5.14 alongside the rime splintering rate. As can be seen in figure 5.14a rime splintering occurs mainly in the layer below the cloud from 200 to 1000 m, with a maximum at 500 m of around 0.4 particles per second and kilogram air. Below 500 m riming occurs solely with rain drops, since cloud droplets are not available. Above that region all particle types exist and may contribute to rime. Precipitation in lower heights primarily consists of graupel and ice crystals, with some snow and little hail, making graupel the main contributor there.

Although the highest concentration of cloud droplets and rain ranges from 1000 to around 2300 m, no riming takes place is that region. The reason for this lies in the temperature range where the process is active. As can be taken from figure 5.14b the minimum Temperature of $-8\,°\mathrm{C}$, where splinters are produced (see section 3.2.1), rises not higher than the estimated 1000 m during the simulation.

It can be concluded, that in the cloud cases at hand, rime splintering is largely inhibited by cold temperatures. And even in lower parts of the atmosphere, where temperatures support rime splintering, the gain is very small, because particle number concentrations may have been reduced by aggregation, melting, or evaporation.

5.4.2 Droplet shattering

Droplet shattering is expected to occure in all altitudes where rain exists and freezes, though, with neglectable efficiencies in regions warmer than $-10\,^{\circ}$C and colder than $-20\,^{\circ}$C, as the implemented routine allows (refer to section 3.2.2). Matching the temperature profile (figure 5.15b) with the availability of rain (figure 5.15a), one would expect, that droplet shattering starts at 500 m where the upper temperature limit is passed. This proves to be true by the vertical distribution of the fragment generation rate, that is shown in figure 5.16. The droplet shattering rate has its maximum at all times around the same altitude as the maximum rain drop number concentration, while rising and decreasing synchronously.

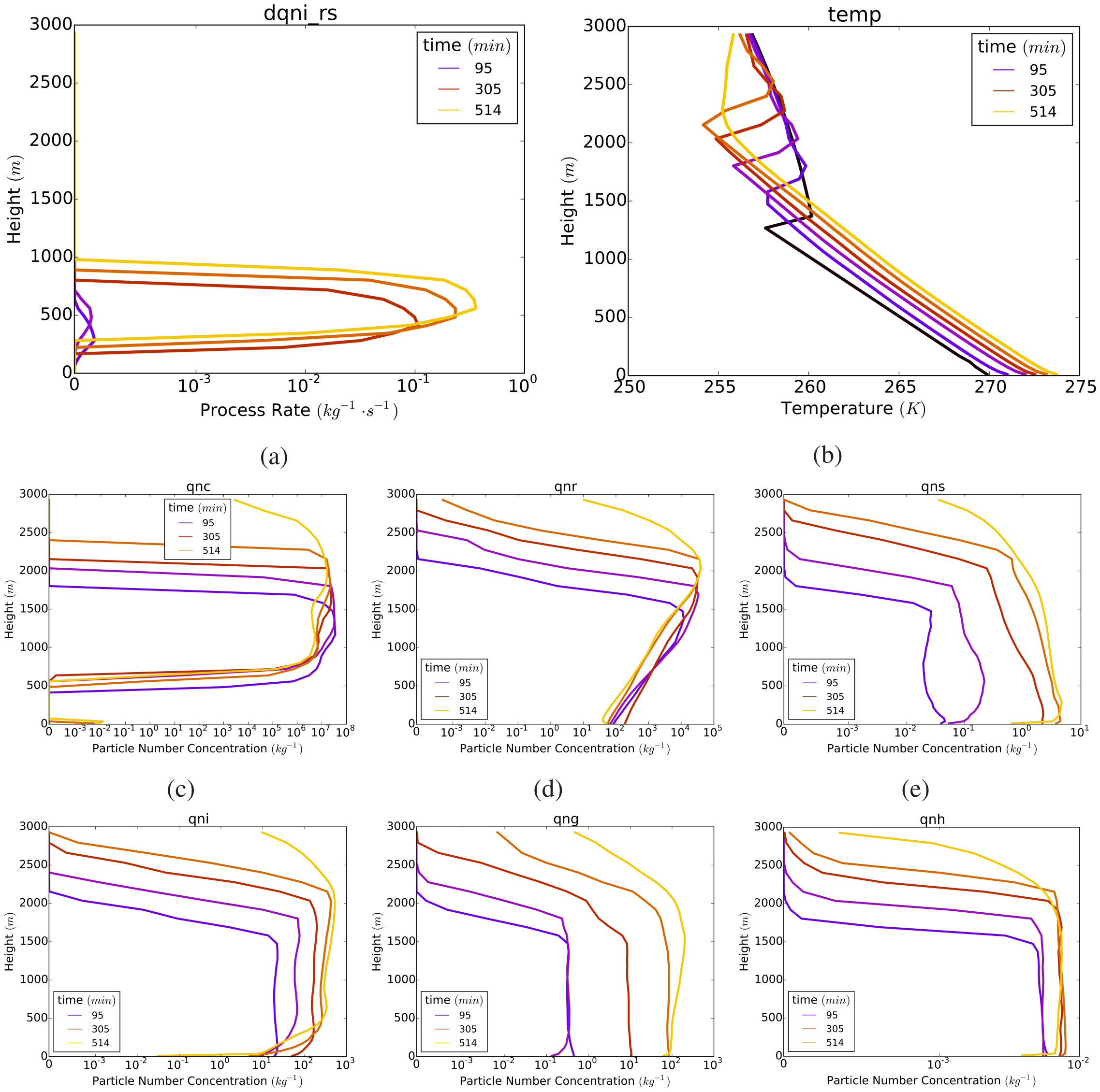

(a) (b)

(c) (d) (e)

(f) (g) (h)

Figure 5.14: Vertical profiles of a) SIP rate and b) corresponding temperature profile. Also shown are vertical profiles of horizontal mean mass mixing ratios for c) cloud droplet, d) rain drop, e) snow particle, f) ice crystal, g) graupel particle, and h) hail particle number concentrations. Shown is the $^{M}(RS)$ run.

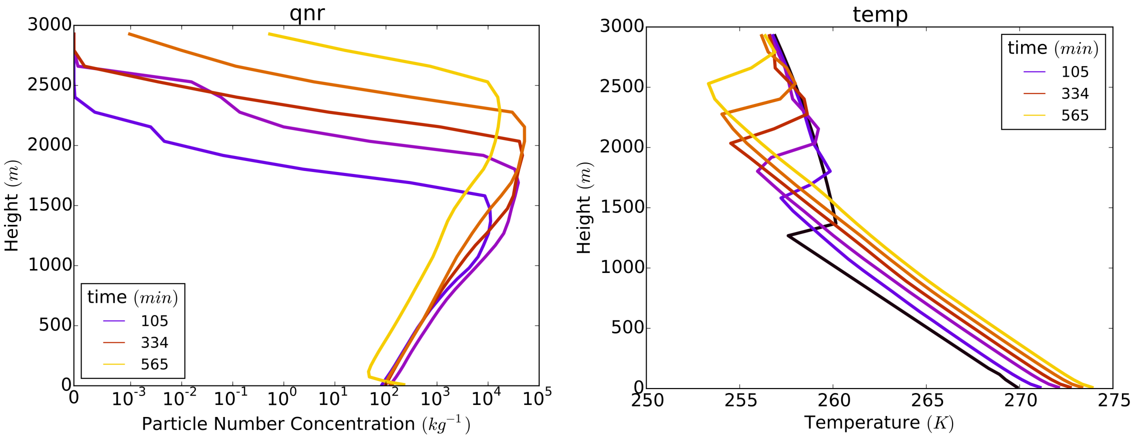

(a) (b)

Figure 5.15: a) Vertical profile of rain drop horizontal mean mass mixing ratio and b) corresponding temperature profile of the $^{M}(DS)$ run.

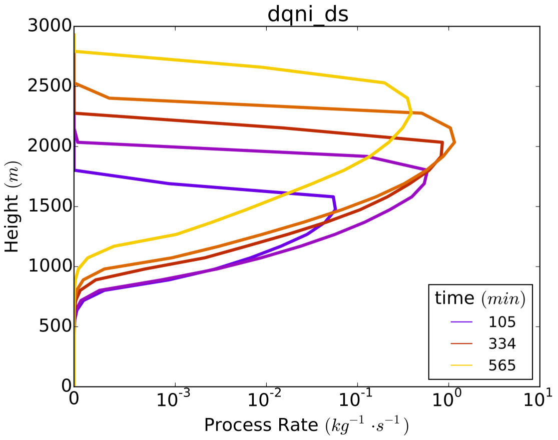

Figure 5.16: Vertical distribution of droplet shattering rate of the $^{M}(DS)$ run.

5.4.3 Collisional Breakup

Figure 5.17 shows the occurrence of collisional breakup, as well as the profiles of temperature and the involved particle classes snow, graupel, and hail. Since the fragment generation function of the implemented collisional breakup process (refer to section 3.2.3) produces particles in the whole temperature range, except at high subzero temperatures, the rate profile shows appropriate splinter generation throughout the entire boundary layer. The height where the rate experiences its maximum strongly correlates with early graupel maxima and with those of snow particles later in the course of the simulation. Considering the particle profiles, it appears obvious, that most splinters are being generated through the collision of snow with graupel and other snow particles. The over all maximum of around 10×10^{3} splinters per kilogram and second appears after 9 hours in heights of 1500 m to 2200 m around 200 m below cloud top.

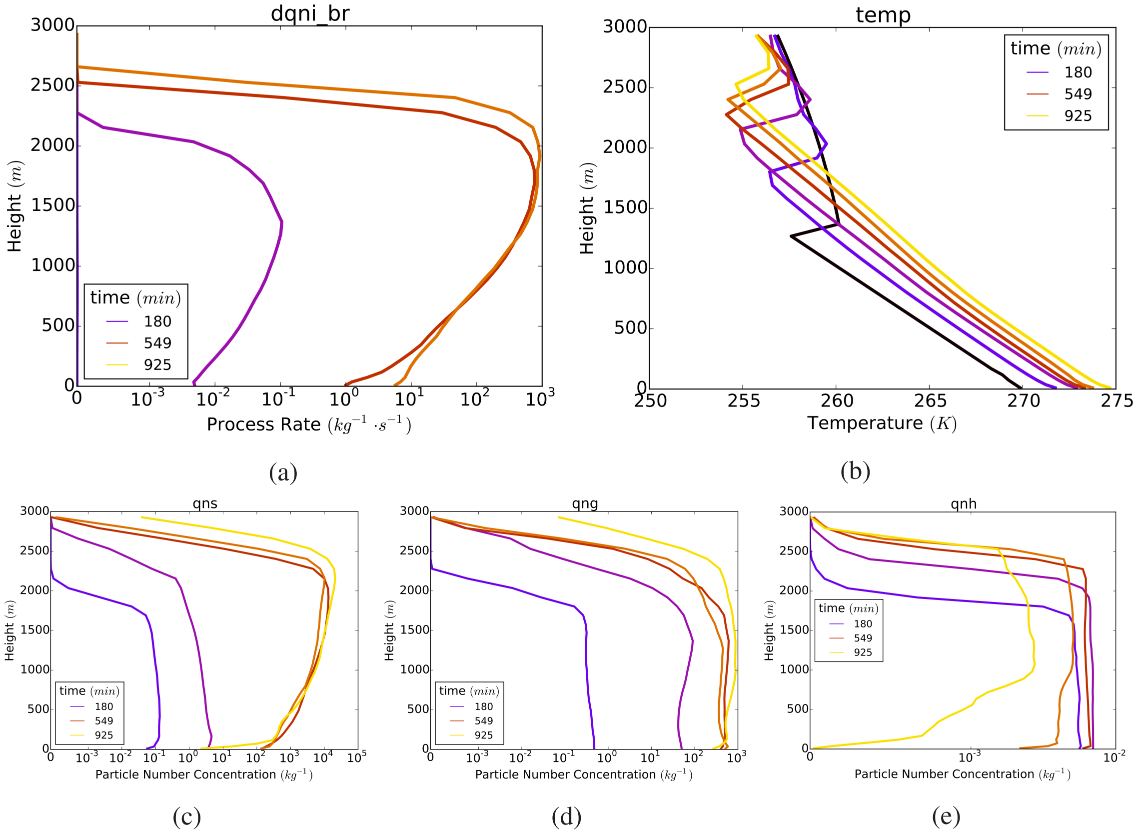

(a) (b)

(c) (d) (e)

Figure 5.17: Vertical profiles of a) SIP rate and b) corresponding temperature profile. Also shown are vertical profiles of horizontal mean mass mixing ratios for c) snow, d) graupel, and e) hail particle number concentrations. Shown is the $^{M}(BR)$ run.

5.5 Vertical velocity of high SIP Grid Cells

Finally the relation between SIP and vertical velocity is investigated. To identify possible correlations vertical velocity distributions are plotted as histograms once for the whole domain below 3000 m and once only for grid cells where SIP reaches a cloud case specific minimum. Sensitivity simulations involving rime splintering are not analyzed, since the fragment generation rates are to small to yield valuable information.

5.5.1 ISDAC

Figure 5.18 shows a set of velocity histograms of vertical velocity for the first 15 hours of the ISDAC case. The control run histogram is also shown for comparison. The unfiltered plots are positioned on the left side, the SIP only plots on the right. The minimum value for grid cell velocities to be included in the latter is $0.1\,\mathrm{kg}^{-1}\,\mathrm{s}^{-1}$, what is rather low, but since the ISDAC case in general is not very sensitive to SIP, higher values would reduce the sample size to much.

Key features of the domain wide velocity histograms occure in all displayed simulations. All of these exhibit a generally symmetrical distribution for small velocities less than $1\,\mathrm{m\,s}^{-1}$ in absolute value. For larger velocities, however, the histogram is slightly skewed towards negative values, that can be attributed to falling particles and thereby induced turbulence. The overall spectrum ranges from $-5\,\mathrm{m\,s}^{-1}$ to somewhere between $3.5\,\mathrm{m\,s}^{-1}$ and $4\,\mathrm{m\,s}^{-1}$ depending on the sensitivity

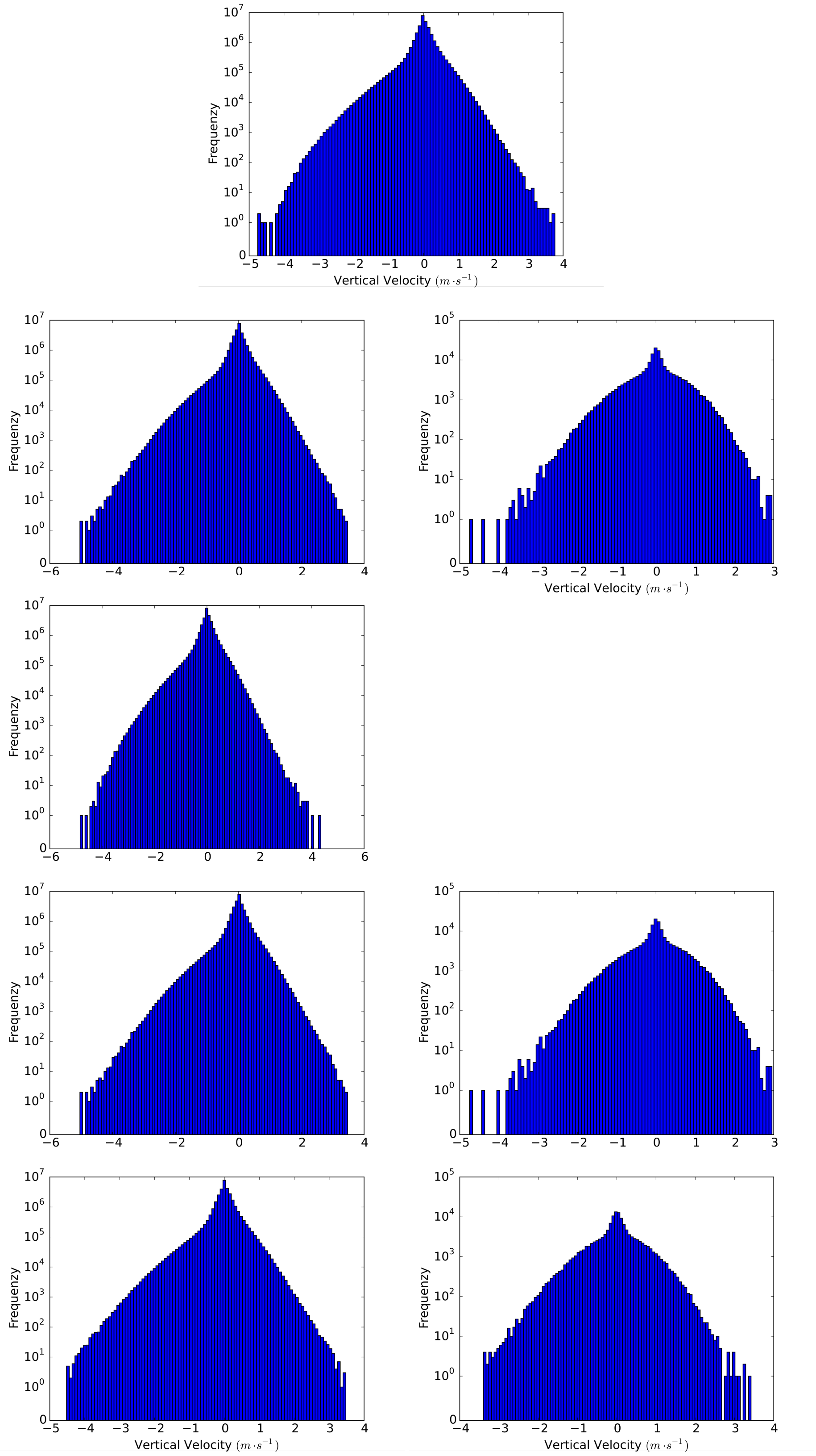

Figure 5.18: Histograms of vertical velocity for all grid cells (left), for grid cells with SIP rate higher than $0.1\,\mathrm{kg}^{-1}\,\mathrm{s}^{-1}$ (right), and for the control run with grid cells below 3000 m taken into account. The simulations depicted are $^{I}(SIP_{off})$, $^{I}(DS)$, $^{I}(BR)$, $^{I}(DS+BR)$, and $^{I}(SIP_{on,BR_C})$.

run.

No plot could be produced for the $^{I}(BR_C)$ run, since SIP rates were to small. That coincides with the previous finding, that In the ISDAC case mainly droplet shattering contributes to SIP in all sensitivity simulations. Therefore histograms of $^{I}(DS)$, $^{I}(DS+BR_C)$, and $^{I}(SIP_{on,BR_C})$ appear very similar in shape. The different amplitudes of the distributions mainly result from different run times.

Comparing the whole domain with the SIP only histograms, one notices a larger decrease of slow compared to medium velocities. The extreme tails of the distributions are cut short on both ends, but with larger change on the negative end, where the difference is around $1\,\mathrm{m\,s^{-1}}$. This may be because faster droplets have already reached lower and warmer regions, statistically escaping freezing.

5.5.2 M-PACE

The M-PACE case, in this regard, looks almost opposite to the ISDAC case. Figure 5.19 shows again histograms of the whole domain below 3000 m, as well as SIP only grid cell wind speeds, with the lower limit of SIP set to $3\,\mathrm{kg^{-1}\,s^{-1}}$.

Very narrowly around zero vertical motion the distribution looks symmetrical. Towards greater velocities, however, it is skewed to positive values. This is due to the domain wide upward vertical movement induced by the strong surface heat fluxes discussed in section 5.2.2. Over all the M-PACE case exhibits a wider scope of vertical wind speeds ranging from $-6\,\mathrm{m\,s^{-1}}$ to $7\,\mathrm{m\,s^{-1}}$ for the $^{M}(DS)$ and $^{M}(BR_C)$ unfiltered histograms. The control run displays a range from $-7\,\mathrm{m\,s^{-1}}$ to $7\,\mathrm{m\,s^{-1}}$, skewed in the sense, that positive intermediate values are enhanced. Lastly, the $^{M}(DS+BR_C)$ and $^{M}(SIP_{on,BR_C})$ simulations experience the highest wind speeds, with outliers of $-10\,\mathrm{m\,s^{-1}}$ and $10\,\mathrm{m\,s^{-1}}$.

Due to instability of the model, that led to unphysical wind speeds before the simulations terminated, the last time steps off each individual run were excluded from this analysis. However some remnants may still be accounted for in the $^{M}(DS+BR_C)$ and $^{M}(SIP_{on,BR_C})$ runs.

Applying the lower SIP limit to the histograms, it changes the picture in several ways. One matter, that catches the eye, is the difference in sample size, that is radically more reduced in simulations involving droplet shattering, because the $^{M}(BR_C)$ run produces a lot more secondary ice (see to section 5.2.2). In simulations $^{M}(DS+BR_C)$ and $^{M}(SIP_{on,BR_C})$ the extreme tails of the distributions are eliminated for a velocity reduction of $4\,\mathrm{m\,s^{-1}}$ and $3\,\mathrm{m\,s^{-1}}$ at both ends respectively, indicating a overall reduced spectrum. In case of $^{M}(DS)$ or $^{M}(BR_C)$ the negative ends are more affected, with a the lowest measured velocity being $2\,\mathrm{m\,s^{-1}}$ and $1.5\,\mathrm{m\,s^{-1}}$ reduced respectively, while the upper extreme value stays unaffected.

Keep in mind, that interpretation of the histograms with involved droplet shattering is difficult because of the low sample size.

For the $^{M}(BR_C)$ run, however, the shift towards positive values, when considering SIP rates, indicates process activity in higher altitudes near cloud top and less in the precipitation region. This is consistent with the findings in section 5.4.3. The $^{M}(BR_C)$ case shows one other feature, that should be mentioned. The sharp frequency maximum around vanishing velocity is gone when considering SIP only grid cells. This suggest influences of particle velocity on collisional fragmentation, what seems intuitive. However, the way collisional fragmentation is implemented in this study (see section 3.2.3 for details) particle velocity only effects the collision kernel and not the fragmentation

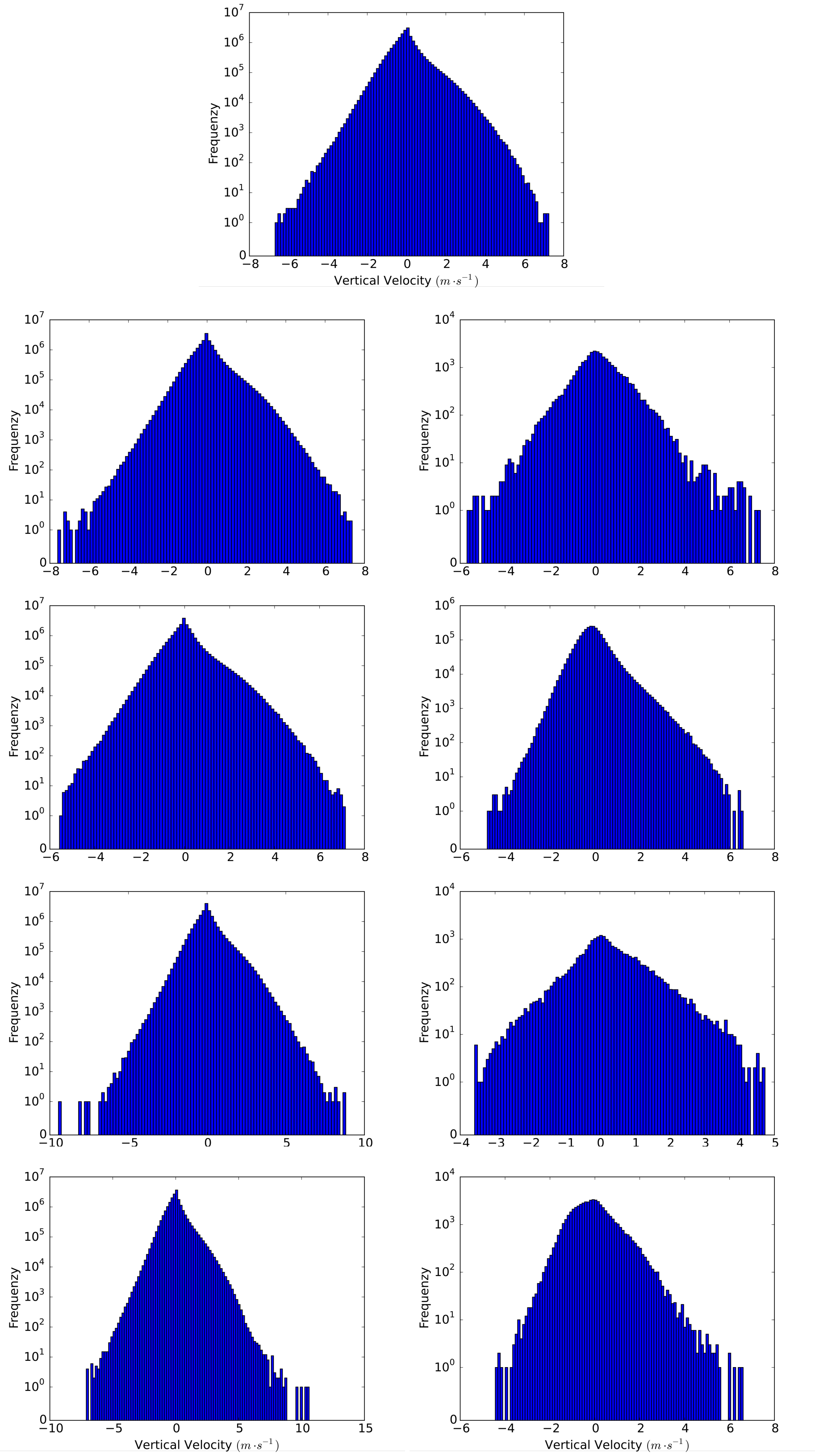

Figure 5.19: Histograms of vertical velocity for all grid cells (left), for grid cells with SIP rate higher than $0.1\,\mathrm{kg}^{-1}\,\mathrm{s}^{-1}$ (right), and the control run with grid cells below 3000 m taken into account. The simulations depicted are $^{I}(SIP_{off})$, $^{I}(DS)$, $^{I}(BR)$, $^{I}(DS+BR)$, and $^{I}(SIP_{on,BR_C})$.

itself, which makes the process less sensitive to such. If the microphysics scheme would capture the velocity effect on fragmentation, an significantly higher reduction in the low velocity range would be expected.

6 Summary and Outlook

The goal of this study was to investigate the influence of SIP on properties of arctic mixed-phase clouds. The tool at hand was the ICON-LEM, that was modified with parameterizations of three prominent SIP mechanisms. Sensitivity experiments were performed on two idealized stratiform cloud cases, based on the observations during the ISDAC and the M-PACE field campaigns over the Beaufort sea north of Alaska. These differed in horizontal wind velocity, surface sensible and latent heat fluxes, and were initiated with slightly different temperature and water vapor profiles.

Building on the preceding work of Dr. Beydoun, temperature dependent parameterizations based on Sullivan et al. [2018] for rime splintering, droplet shattering, and collisional breakup were implemented into the ICON code. The sensitivity experiments consisted of eight simulations for each cloud case, that included all possible combinations of these three processes. Additionally, simulations with the collisional breakup process were performed once using a constant number of 50 fragments generated per collision, and a second time using individual fragment numbers for collisions with different particle classes involved. The values for the variant fragment numbers were based on a new collisional breakup scheme by Phillips et al. [2017] and were additionally dependent on particle mass and the relative velocity of the collision partners. The sensitivity experiments were limited to the first 15 hours of the ISDAC and eight to ten hours of the M-PACE case.

The two simulated cases produced stratiform clouds, that developed at different rates. While the cloud layer in the ISDAC case was dynamically decoupled from the surface and experienced a rise of about 30 m per hour, the M-PACE cloud, driven by the strong surface fluxes, ascended 80 m per hour and experienced overall stronger turbulence.

All model runs of the ISDAC case simulated the domain average LWP to stabilize around $0.14\,\mathrm{kg\,m^{-2}}$ between ten to 14 hours after simulation start, with very little deviations due to SIP processes. IWP was qualitatively influenced by SIP when starting to fluctuate after eleven hours but the spread of all sensitivity runs stayed small around $2.26 \times 10^{-4}\,\mathrm{kg\,m^{-2}}$ in the same time interval.

In the M-PACE case LWP experienced more fluctuation early on but quantitatively stayed in a narrow range around $0.19\,\mathrm{kg\,m^{-2}}$ for all sensitivity experiments up until eight hours. IWP stabilized around $2.07 \times 10^{-2}\,\mathrm{kg\,m^{-2}}$ in the same time period. After that, simulation ${}^{M}(BR_C)$ and ${}^{M}(RS + BR_C)$ exhibited a LWP reduction of about one order of magnitude. This effect was also visible in the evolution of IWP, where the ${}^{M}(BR_C)$ and ${}^{M}(RS + BR_C)$ runs featured an increase of not quite one order of magnitude after eight hours. However, additional droplet shattering seemed to compensate this development completely.

One other feature stands out in the IWP picture. All sensitivity experiments including droplet shattering, experience an negative offset compared to the other simulations, right from simulation start. Why the droplet shattering process induced the observed inhibition of ice crystal formation could not be answered in this study and needs further investigation. However, it is hypothesized, that the redistribution of frozen rain drop fragments into the particle classes ice, graupel and hail does not work correctly, since an actual increase of particle numbers would be expected.

The application of two different versions of the collisional breakup process had quite different outcomes. While the use of a constant fragment number per collision led to an increase in ice crystal number concentration of more than two orders of magnitude, the individual treatment of collisions of different types of particles completely prevented this enhancement. This is due to the fact, that the constant variant of the parameterization overestimates the amount of fragments for all types of collisions in the M-PACE case, compared to the variable variant.

Although the constant variant in the ISDAC case actually underestimates the produced fragments in collisions involving snow, no effect is observed in those simulations. That can be explained with the overall smaller particle number concentrations of the frozen classes.

Due to the low temperatures in all simulations no statements can be made about the sensitivity of the simulated clouds on the rime splintering process.

Ideas for Future Studies

In depth comparison to observations may result in a better interpretation of the results of this study in terms of realism and applicability of the SIP parameterizations. Furthermore, several ideas to improve the existing model set-ups and SIP implementations are suggested.

Some simulations had considerable problems with stability. While the ISDAC case generally run smoothly, the M-PACE simulations experienced vertical instability through violating the Courant-Friedrichs-Lewy condition, leading to unphysically high vertical wind speeds, that in turn caused the simulations to terminate. This complicated the analysis of the sensitivity simulations of the more dynamic M-PACE case. These problems were not addressed conclusively in the scope of this thesis and could not be solved. Solutions that were tried, include lowering the model time step, increasing the radiation time step, changing the damping height, changing the aerosol scheme, and increasing computational resources. All strategies either failed completely or showed only marginal improvement.

In order to better match simulations and observational background, implementation of large scale forcing, as well as horizontal wind speed nudging was attempted, but failed again because of model instability. This is a serious issue and should be addressed. Once this is accomplished, the simulation set-ups can be adjusted, increasing the realism of the considered clouds. Nevertheless, the simulated stratiform clouds yielded valuable information about cloud sensitivity to SIP.

An additional option for better adapting the synoptical basis, that was not done in this study, concerns the aerosol background of the two cases. As mentioned in section 4.2, the ISDAC and the M-PACE studies where conducted in different seasonal time periods, being exposed to different environmental situations, including aerosol load. Introducing more realistic aerosol schemes would further differentiate the two cases, giving insight to a wider range of arctic clouds. As Korolev et al. [2017] points out, there are different indirect effects currently discussed, concerning the sensitivity of mixed-phase clouds to aerosols.

1. Higher concentrations of INP lead to a higher ice crystal number concentration, that influences glaciation of clouds [Lohmann, 2002].

2. Higher CCN concentrations cause higher amounts of cloud droplets, while reducing their mean sizes. This would lead to a reduced riming efficiency and a larger liquid to ice partitioning of the cloud [Borys et al., 2003].
3. Lower CCN concentrations lead to larger liquid drop sizes, that affects SIP processes [Rangno and Hobbs, 2001]. This may be due to increased riming and subsequently larger frozen particles with higher rime fraction, enhancing rime splintering and collisional fragmentation. Larger liquid particles may also shatter more frequently, increasing fragmentation through droplet shattering.

Jackson et al. [2012] analyzed the effect of aerosol concentrations on the two regarded field campaigns. While the riming indirect effect could not be confirmed, they found indications for the glaciation indirect effect influencing the ice crystal number concentration in the ISDAC case through entrainment of aerosols from above the cloud. It was also acknowledged, that the cleaner air in the M-PACE case could explain the increase in ice crystal and decrease in cloud droplet number concentrations. However, it was emphasized, that there was no clear evidence for the influence of aerosol conditions on the different cloud properties, since the synoptic situations also had great impact.
In that sense, to get more insight into specific microphysical effects and their dependence on environmental conditions, research regarding a wider range of synoptic situations and aerosol conditions, is indeed recommended.

There is always room for improvement of the process implementations. A first step would certainly be to implement collisional breakup for all possible particle-particle collisions. So far, this has been restricted to collisions without ice, due to the lower fragmentation rate of ice crystals. Furthermore there has not been done an implementation for hail-hail collisions, that would surely add another strong source of fragmentation. It is assumed that this process could become the main contributor to collisional fragment generation, due to the particles high mass and velocity, if number concentrations would be high enough and snow would not be the primary collision partner. The reason this was not done in this study, was the small amount of hail, that was produced in both cloud cases, while graupel and snow were clearly the main players here.
Additionally, and for the same reason, snow-graupel and snow-hail collisions could be split into independent model routines, to further enhance the precision of this process. In general it could be argued, that the differences between hail and graupel may be small and simply lie in their size, mass and corresponding fall velocity, and therefore could be consolidated into the same routine. But as long as these properties are not included into the collisional breakup algorithm, collisions involving graupel should be separated from those involving hail.
A simple example, based on the Phillips et al. [2017] parameterization, may help illustrate this matter. Again calculating the sensitivity of fragment generation with equation 3.40 and the expression for the density of breakable branches at the surface of spatial planar crystals 3.46, and using the mean particle masses and the optimal temperature for this process, the maximum amount of fragments generated during one snow-graupel collision yields approximately 65 fragments in the M-PACE case and 424 fragments in the ISDAC case. Performing the same procedure for a snow-hail collision, the results yield approximately 106 fragments in the M-PACE case and 801

fragments in the ISDAC case.

Putting aside the concerns of realism while using mean particle masses and estimations for riming fraction and effective spherical diameter, this example, nevertheless, shows how sensitive this process is to factors other than temperature. Ideally, a physically more complete implementation like the one proposed by Phillips et al. [2017] may be used in the first place. This parameterization especially captures particle velocity and mass better, and in this regard seems to be superior to the current implementation used in this study. This would not be trivial, however, since a selective distinction between smaller and larger collision partner would have to be performed, while the treatment of particle mass in the used model is not based on a bin, but a bulk microphysics scheme.

One strong advantage of the new collision scheme surely is the variable treatment of rime fraction, that suggests applications in property-based ice microphysics schemes. Nevertheless, good improvements are expected by integrating the scheme into the existing model framework.

Final Thoughts

Finally, some elementary statements shall be highlighted, where this study agrees with preceding research on secondary ice processes.

First, the understanding of secondary ice production mechanisms is still poor and developments in parameterization of these processes are just beginning to unfold. This study showed how different parameterizations may lead to different results, even when initial conditions are the same.

Second, supporting conditions for secondary ice formation are diverse and the sensitivity of the processes to those differ greatly. This was made clear by the strongly inhibited rime splintering mechanism, that may be better observed in warmer clouds. Collisional breakup on the other hand tends to be largely dependent on the number of preexisting ice particles, that can lead to a self-inflicted intensified enhancement of ice crystal numbers, especially if an abundance of liquid water exists.

Eventually, this study could not find clear evidence for a strong impact of secondary ice formation processes on properties of stratiform clouds. Large differences between the results of the two analyzed cloud cases are primarily attributed to the stronger dynamic nature of the cold air outbreak during M-PACE and the more stable environment of the boundary layer during ISDAC.

List of Figures

2.1 Cloud microphysical interactions included in the ICON model. The boxes represent the particle classes and water vapor. Larger particles are located further down. The arrowheads symbolize where the product of the process is assigned to. The colors of the arrow line represent the classes of all participating particles. (adapted from Seifert [2002]) 4

2.2 Schematic diagram of the main ice processes in convective clouds. The depicted cloud is segmented by dashed lines into an all-liquid, a mixed-phase, and an all-ice part. Round symbols represent liquid droplets, hexagonal shapes symbolize frozen and combinations of both rimed particles, and fragments from SIP are indicated as small rectangles. The values on the left side showcase the spacial distribution of cloud temperature. Temperature ranges, where the microphysical processes are active, are symbolized by arrows and bars. An arrow with bar indicates an one sided open range, two bars a relatively constrained range, and the bar with two arrows indicates a two sided open range with a defined efficiency maximum. (based on Lamb and Verlinde [2011] and Hartmann [2019]) 6

2.3 Number of ice crystals measured on 4 different dates plotted over the respective cloud top temperature. The dashed lines indicate the range of active INP concentration, while the different markers symbolizes measured ice crystal concentrations. 7

2.4 Droplet shattering event with two larger and some smaller fragments. The latter are highlighted inside the red circle. (from Lauber et al. [2018]) 8

2.5 Fragment number of graupel-graupel-collisions during laboratory experiments of Takahashi et al. [1995] with a collision force of $5 \times 10^{-3}\,\mathrm{N}$. The fragment maximum appears to center around $-15\,^{\circ}\mathrm{C}$. 9

3.1 Fragment numbers generated by the Sullivan et al. [2017b] particle-particle-collision parameterization (equation 3.38) with leading factors depending on collision types and calculated with the Phillips et al. [2017] parameterization. Blue lines symbolize parameterization for the ISDAC case (section 4.2.1), red those for M-PACE case (section 4.2.2). Black is the reference simulation BR_C with a constant leading factor of 50. 27

3.2 Temperature dependent parts of the SIP parameterizations. Black is the fragment generation function of the collisional breakup reference simulation BR_C, blue is the droplet shattering probability function and red is the temperature weighting function for rime splintering. 28

4.1 Satellite image of the North Slope of Alaska and the adjacent Beaufort Sea. The black dots indicate the to observation sites from where aircraft measurements were started during the ISDAC (Barrow) and M-PACE (Barrow, Oliktok Point) field campaigns. The visible cloud-streets belong to a cold air outbreak that occurred on 9 October 2004. 30

4.2 Initial soundings used for the ISDAC case. a) Temperature (red) and liquid water potential temperature (blue). b) Initial water vapor mass mixing ratio profile. . . 31

4.3 Initial soundings used for the M-PACE case. a) Temperature (red) and liquid water potential temperature (blue). b) Initial water vapor mass mixing ratio profile. . . . 34

5.1 Time evolution of vertical profiles of the ISDAC horizontal mean LWC (a) and IWC (b) as well as the variance of vertical velocity $< w^2 >$ (c) and temperature (d) for the control run $^I(SIP_{off})$. Only the first 22 height levels are shown. the color bars of the LWC and IWC image differ in around two orders of magnitude. Little production of ice crystals is already happening after half an hour, but is hardly visible in figure b). 36

5.2 Time evolution of the horizontal mean and vertically integrated mass for all hydrometeors of the $^I(SIP_{off})$ run. Water vapor is also included. 37

5.3 Time evolution profiles of the M-PACE horizontally mean LWC (a) and IWC (b) as well as the variance of vertical velocity $< w^2 >$ (c) and temperature (d) for the control run $^M(SIP_{off})$. Only the first 22 height levels are shown. The color bars range of LWC and IWC differ in around one and a half orders of magnitude. . . . 38

5.4 Time evolution of the horizontal mean and vertically integrated masses for all hydrometeors of the $^M(SIP_{off})$ run. Water vapor is also included. 39

5.5 Time evolution of vertical profiles of the M-PACE horizontal mean LWC (a) and IWC (b) for the $^M(BR_C)$ run, and LWC (c) for the $^M(SIP_{on,BR_C})$ run. d) Time evolution of the horizontal mean of vertically integrated masses for all hydrometeors of the $^M(BR_C)$ run. Water vapor is also included. 39

5.6 Time series of the first 15 hours of horizontally averaged LWP (a) and IWP (b) for the ISDAC case. For the collisional breakup process the constant variant BR_C was used. 40

5.7 Time series of horizontally averaged LWP (a) and IWP (b) for the M-PACE case. For the collisional breakup process the constant variant BR_C was used. 41

5.8 Time series of horizontally averaged LWP (a) and IWP (b) for the M-PACE and simulations involving the constant collisional breakup variant BR_C. 42

5.9 The first 15 hours of horizontal average of vertically integrated ice crystal number concentration for all sensitivity experiments of the ISDAC case. Simulations including the constant variant of collisional breakup BR_C (a) and the variable variant BR_V (b) are shown. 44

5.10 Time series of the first 15 hours of horizontally averaged and vertically integrated SIP rates for $^I(SIP_{on,BR_C})$ (a) and $^I(SIP_{on,BR_V})$ (b). 44

5.11 Horizontal average of vertically integrated ice crystal number concentration for all sensitivity experiments of the M-PACE case. Simulations including the constant variant of collisional breakup BR_C (a) and the variable variant BR_V (b) are shown. 45

5.12 Rate of produced fragments through collisional fragmentation for $^M(BR_C)$ (blue) and $^M(BR_V)$ (red). Depicted are the horizontal averages of the vertically integrated generation rates. 45

5.13 Time evolution of the horizontal mean of vertically integrated particle number concentrations for all hydrometeor and a) $^M(BR_C)$ and b) $^M(BR_V)$. 46

5.14 Vertical profiles of a) SIP rate and b) corresponding temperature profile. Also shown are vertical profiles of horizontal mean mass mixing ratios for c) cloud droplet, d) rain drop, e) snow particle, f) ice crystal, g) graupel particle, and h) hail particle number concentrations. Shown is the $^M(RS)$ run. 47

5.15 a) Vertical profile of rain drop horizontal mean mass mixing ratio and b) corresponding temperature profile of the $^M(DS)$ run. 48

5.16 Vertical distribution of droplet shattering rate of the $^M(DS)$ run. 48

5.17 Vertical profiles of a) SIP rate and b) corresponding temperature profile. Also shown are vertical profiles of horizontal mean mass mixing ratios for c) snow, d) graupel, and e) hail particle number concentrations. Shown is the $^M(BR)$ run. . . 49

5.18 Histograms of vertical velocity for all grid cells (left), for grid cells with SIP rate higher than $0.1\,\mathrm{kg^{-1}\,s^{-1}}$ (right), and for the control run with grid cells below 3000 m taken into account. The simulations depicted are $^I(SIP_{off})$, $^I(DS)$, $^I(BR)$, $^I(DS+BR)$, and $^I(SIP_{on,BR_C})$. 50

5.19 Histograms of vertical velocity for all grid cells (left), for grid cells with SIP rate higher than $0.1\,\mathrm{kg^{-1}\,s^{-1}}$ (right), and the control run with grid cells below 3000 m taken into account. The simulations depicted are $^I(SIP_{off})$, $^I(DS)$, $^I(BR)$, $^I(DS+BR)$, and $^I(SIP_{on,BR_C})$. 52

List of Tables

2.1 Power laws for equivalent spherical diameter and terminal fall velocitie of all hydrometeor classes, coefficients of the particles generalized Γ-distributions and corresponding ranges of mean particle mass. The power law coefficients are rounded to three decimal places. 11

2.2 Some attributes of the frozen particle classes essential for collection processes. $\overline{E}^{max}_{j,CLS}$ is the collision efficiency, D_{crit} is the critical diameter, below that collision efficiency is zero, q_{crit} is the lower limit of total mass mixing ratio necessary for the collection to happen, and σ_{υ} is the fall velocity variance. 14

2.3 Collision and sticking coefficients for all collection processes included in the ICON model. Information on the literary bases of the parameterizations is given in the text. 15

3.1 Mean masses of the BR_C simulations. 26

3.2 Number of fragments generated in specific particle-particle collision, as well as the corresponding scaling factors of the fragment generation functions, for both cloud cases. 26

3.3 SIP relevant parameters. 28

5.1 Overview over all simulations. The prescribed superscript indicates the cloud case, the information inside parentheses the combination of active SIP mechanisms. Simulations without SIP are indicated as SIP_{off}, simulations including all three processes as SIP_{on}. 35

5.2 Liquid-Ice partitioning of ISDAC and M-PACE simulations, as well as average amount of total condensate. The ratios are calculated from horizontally and timewise averaged, vertically integrated particle masses. The amount of total condensate is given in $(\mathrm{kg\,m^{-2}})$ and calculated as the sum of all six hydrometeor masses. 43

Bibliography

Ackerman, A. S., Hobbs, P. V., and Toon, O. B. A model for particle microphysics, turbulent mixing, and radiative transfer in the stratocumulus-topped marine boundary layer and comparisons with measurements. *Journal of the Atmospheric Sciences*, 52(8):1204–1236, 1995. doi: 10.1175/1520-0469(1995)052<1204:AMFPMT>2.0.CO;2. URL `https://doi.org/10.1175/1520-0469(1995)052<1204:AMFPMT>2.0.CO;2`.

Bacon, N. J., Swanson, B. D., Baker, M. B., and Davis, E. J. Breakup of levitated frost particles. *Journal of Geophysical Research: Atmospheres*, 103(D12):13763–13775, 1998. doi: 10.1029/98JD01162. URL `https://agupubs.onlinelibrary.wiley.com/doi/abs/10.1029/98JD01162`.

Barklie, R. H. D. and Gokhale, N. The freezing of supercooled water drops. *McGill University, Stormy Weather Group, Scientific Report MW-30, Part III*, page 43–64, 1959.

Beard, K. V. Ice initiation in warm-base convective clouds: An assessment of microphysical mechanisms. *Atmospheric Research*, 28(2):125 – 152, 1992. ISSN 0169-8095. doi: https://doi.org/10.1016/0169-8095(92)90024-5. URL `http://www.sciencedirect.com/science/article/pii/0169809592900245`.

Bigg, E. K. The formation of atmospheric ice crystals by the freezing of droplets. *Quarterly Journal of the Royal Meteorological Society*, 79(342):510–519, 1953. doi: 10.1002/qj.49707934207. URL `https://rmets.onlinelibrary.wiley.com/doi/abs/10.1002/qj.49707934207`.

Borys, R. D., Lowenthal, D. H., Cohn, S. A., and Brown, W. O. J. Mountaintop and radar measurements of anthropogenic aerosol effects on snow growth and snowfall rate. *Geophysical Research Letters*, 30(10), 2003. doi: 10.1029/2002GL016855. URL `https://agupubs.onlinelibrary.wiley.com/doi/abs/10.1029/2002GL016855`.

Boucher, O., Randall, D., Artaxo, P., Bretherton, C., Feingold, G., Forster, P., Kerminen, V.-M., Kondo, Y., Liao, H., Lohmann, U., Rasch, P., Satheesh, S. K., Sherwood, S., Stevens, B., and Zhang, X. Y. Clouds and aerosols. In Stocker, T. F., Qin, D., Plattner, G.-K., Tignor, M., Allen, S. K., Doschung, J., Nauels, A., Xia, Y., Bex, V., and Midgley, P. M., editors, *Climate Change 2013: The Physical Science Basis. Contribution of Working Group I to the Fifth Assessment Report of the Intergovernmental Panel on Climate Change*, pages 571–657. Cambridge University Press, Cambridge, United Kingdom and New York, NY, USA, 2013. doi: 10.1017/CBO9781107415324.016.

Brownscombe, J. L. and Thorndike, N. S. C. Freezing and shattering of water droplets in free fall. *Nature*, 220(5168):687 – 689, 11 1968. ISSN 1476-4687. doi: 10.1038/220687a0. URL `hthttps://doi.org/10.1038/220687a0`.

Cotton, W. R., Tripoli, G. J., Rauber, R. M., and Mulvihill, E. A. Numerical simulation of the effects of varying ice crystal nucleation rates and aggregation processes on orographic snowfall. *Journal of Climate and Applied Meteorology*, 25(11):1658–1680, 1986. doi: 10.1175/1520-0450(1986)025<1658:NSOTEO>2.0.CO;2. URL `https://doi.org/10.1175/1520-0450(1986)025<1658:NSOTEO>2.0.CO;2`.

Crawford, I., Bower, K., Choularton, T., Dearden, C., Crosier, J., Westbrook, C., Capes, G., Coe, H., Connolly, P., Dorsey, J., Gallagher, M., Williams, P., Trembath, J., Cui, Z., and Blyth, A. Ice formation and development in aged, wintertime cumulus over the uk: Observations and modelling. *Atmospheric Chemistry & Physics Discussions*, 11:30797–30851, 11 2011. doi: 10.5194/acpd-11-30797-2011.

Deutscher Wetterdienst. Icon (icosahedral nonhydrostatic) model. Web page, 09 2019. URL `http://www.dwd.de/EN/research/weatherforecasting/num_modelling/01_num_weather_prediction_modells/icon_description.html`. Accessed: 2019-09-07, 16:55:18.

Dipankar, A., Stevens, B., Heinze, R., Moseley, C., Zängl, G., Giorgetta, M., and Brdar, S. Large eddy simulation using the general circulation model ICON. *Journal of Advances in Modeling Earth Systems*, 7(3):963–986, jul 2015. doi: 10.1002/2015ms000431. URL `https://doi.org/10.1002%2F2015ms000431`.

Field, P. R., Lawson, R. P., Brown, P. R. A., Lloyd, G., Westbrook, C., Moisseev, D., Miltenberger, A., Nenes, A., Blyth, A., Choularton, T., Connolly, P., Buehl, J., Crosier, J., Cui, Z., Dearden, C., DeMott, P., Flossmann, A., Heymsfield, A., Huang, Y., Kalesse, H., Kanji, Z. A., Korolev, A., Kirchgaessner, A., Lasher-Trapp, S., Leisner, T., McFarquhar, G., Phillips, V., Stith, J., and Sullivan, S. Secondary ice production: Current state of the science and recommendations for the future. *Meteorological Monographs*, 58:7.1–7.20, 2017. doi: 10.1175/AMSMONOGRAPHS-D-16-0014.1. URL `https://doi.org/10.1175/AMSMONOGRAPHS-D-16-0014.1`.

Fridlind, A., Ackerman, A., Mcfarquhar, G., Zhang, G., Poellot, M., DeMott, P., Prenni, A., and Heymsfield, A. Ice properties of single-layer stratocumulus during the mixed-phase arctic cloud experiment: 2. model results. *Journal of Geophysical Research*, 112, 12 2007. doi: 10.1029/2007JD008646.

Fridlind, A. M., Jacobson, M. Z., Kerminen, V.-M., Hillamo, R. E., Ricard, V., and Jaffrezo, J.-L. Analysis of gas-aerosol partitioning in the arctic: Comparison of size-resolved equilibrium model results with field data. *J. Geophys. Res.*, 105:19891–19904, 2000. doi: 10.1029/2000JD900257.

Hallett, J. and Mossop, S. C. Production of secondary ice particles during the riming process. *Nature*, 249(5452):26 – 28, 05 1974. ISSN 1476-4687. doi: 10.1038/249026a0. URL `https://doi.org/10.1038/249026a0`.

Hartmann, S. Schematic representation of microphysical processes in a mixed-phase cloud with regard to secondary ice particle production. Web page (Leibniz Institute for Tropospheric Research), 2019. URL `https://www.tropos.de/en/research/aerosol-cloud-interaction/process-studies-on-small-spatial-and-temporal-scales/aerosol-and-clouds-microphysical-interactions/laboratory-studies-on-secondary-ice-produ` Accessed: 2019-11-10, 19:58:00.

Heinze, R., Dipankar, A., Henken, C., Moseley, C., Sourdeval, O., Troemel, S., Xie, X., Adamidis, P., Ament, F., Baars, H., Barthlott, C., Behrendt, A., Blahak, U., Bley, S., Brdar, S., Brueck, M., Crewell, S., Deneke, H., Girolamo, P., and Quaas, J. Large-eddy simulations over germany using icon: a comprehensive evaluation: Evaluation of icon in realistic les configuration. *Quarterly Journal of the Royal Meteorological Society*, 143, 10 2016. doi: 10.1002/qj.2947.

Heymsfield, A. J. and Mossop, S. C. Temperature dependence of secondary ice crystal production during soft hail growth by riming. *Quarterly Journal of the Royal Meteorological Society*, 110: 765–770, July 1984. doi: 10.1002/qj.49711046512.

Hobbs, P. V. and Alkezweeny, A. J. The fragmentation of freezing water droplets in free fall. *Journal of the Atmospheric Sciences*, 25(5):881–888, 1968. doi: 10.1175/1520-0469(1968)025<0881:TFOFWD>2.0.CO;2. URL `https://doi.org/10.1175/1520-0469(1968)025<0881:TFOFWD>2.0.CO;2`.

Hobbs, P. V. and Rangno, A. L. Ice particle concentrations in clouds. *Journal of the Atmospheric Sciences*, 42(23):2523–2549, 1985. doi: 10.1175/1520-0469(1985)042<2523:IPCIC>2.0.CO;2. URL `https://doi.org/10.1175/1520-0469(1985)042<2523:IPCIC>2.0.CO;2`.

Huang, Y., Blyth, A. M., Brown, P. R. A., Choularton, T. W., and Cui, Z. Factors controlling secondary ice production in cumulus clouds. *Quarterly Journal of the Royal Meteorological Society*, 143(703):1021–1031, 2017. doi: 10.1002/qj.2987. URL `https://rmets.onlinelibrary.wiley.com/doi/abs/10.1002/qj.2987`.

Jackson, R. C., McFarquhar, G. M., Korolev, A. V., Earle, M. E., Liu, P. S. K., Lawson, R. P., Brooks, S., Wolde, M., Laskin, A., and Freer, M. The dependence of ice microphysics on aerosol concentration in arctic mixed-phase stratus clouds during isdac and m-pace. *Journal of Geophysical Research: Atmospheres*, 117(D15), 2012. doi: 10.1029/2012JD017668. URL `https://agupubs.onlinelibrary.wiley.com/doi/abs/10.1029/2012JD017668`.

Khain, A., Ovchinnikov, M., Pinsky, M., Pokrovsky, A., and Krugliak, H. Notes on the state-of-the-art numerical modeling cloud microphysics. *Atmospheric Research*, 55:159–224, 12 2000. doi: 10.1016/S0169-8095(00)00064-8.

Klein, S. A., McCoy, R. B., Morrison, H., Ackerman, A. S., Avramov, A., de Boer, G., Chen, M., Cole, J. N. S., Del Genio, A. D., Falk, M., Foster, M. J., Fridlind, A., Golaz, J.-C., Hashino, T., Harrington, J. Y., Hoose, C., Khairoutdinov, M. F., Larson, V. E., Liu, X., Luo, Y., McFarquhar, G. M., Menon, S., Neggers, R. A. J., Park, S., Poellot, M. R., Schmidt, J. M., Sednev, I., Shipway, B. J., Shupe, M. D., Spangenberg, D. A., Sud, Y. C., Turner, D. D., Veron, D. E., von Salzen, K., Walker, G. K., Wang, Z., Wolf, A. B., Xie, S., Xu, X.-M., Yang, F., and Zhang, G. Intercomparison of model simulations of mixed-phase clouds observed during the arm mixed-phase arctic cloud experiment. part i: Single-layer cloud. *Q. J. Roy. Meteorol. Soc.*, 135(641): 979–1002, 2009. doi: 10.1002/qj.416.

Korolev, A., McFarquhar, G., Field, P. R., Franklin, C., Lawson, P., Wang, Z., Williams, E., Abel, S. J., Axisa, D., Borrmann, S., Crosier, J., Fugal, J., Krämer, M., Lohmann, U., Schlenczek, O., Schnaiter, M., and Wendisch, M. Mixed-phase clouds: Progress and challenges. *Meteorological Monographs*, 58:5.1–5.50, 2017. doi: 10.1175/AMSMONOGRAPHS-D-17-0001.1. URL `https://doi.org/10.1175/AMSMONOGRAPHS-D-17-0001.1`.

Lamb, D. and Verlinde, J. *Physics and Chemistry of Clouds*. Cambridge University Press, 2011. doi: 10.1017/CBO9780511976377.

Lauber, A., Kiselev, A., Pander, T., Handmann, P., and Leisner, T. Secondary ice formation during freezing of levitated droplets. *Journal of the Atmospheric Sciences*, 75(8):2815–2826, 2018. doi: 10.1175/JAS-D-18-0052.1. URL `https://doi.org/10.1175/JAS-D-18-0052.1`.

Lawson, R. P., Woods, S., and Morrison, H. The microphysics of ice and precipitation development in tropical cumulus clouds. *Journal of the Atmospheric Sciences*, 72(6):2429–2445, 2015. doi: 10.1175/JAS-D-14-0274.1. URL `https://doi.org/10.1175/JAS-D-14-0274.1`.

Leuenberger, D., Koller, M., Fuhrer, O., and Schär, C. A generalization of the sleve vertical coordinate. *Monthly Weather Review*, 138(9):3683–3689, 2010. doi: 10.1175/2010MWR3307.1. URL `https://doi.org/10.1175/2010MWR3307.1`.

Lilly, D. K. On the numerical simulation of buoyant convection. *Tellus*, 14(2):148–172, 1962. doi: 10.1111/j.2153-3490.1962.tb00128.x. URL `https://onlinelibrary.wiley.com/doi/abs/10.1111/j.2153-3490.1962.tb00128.x`.

Lin, Y.-L., Farley, R. D., and Orville, H. D. Bulk parameterization of the snow field in a cloud model. *Journal of Climate and Applied Meteorology*, 22(6):1065–1092, 1983. doi: 10.1175/1520-0450(1983)022<1065:BPOTSF>2.0.CO;2. URL `https://doi.org/10.1175/1520-0450(1983)022<1065:BPOTSF>2.0.CO;2`.

Lohmann, U. A glaciation indirect aerosol effect caused by soot aerosols. *Geophysical Research Letters*, 29(4):11–1–11–4, 2002. doi: 10.1029/2001GL014357. URL `https://agupubs.onlinelibrary.wiley.com/doi/abs/10.1029/2001GL014357`.

Mason, B. J. and Maybank, J. The fragmentation and electrification of freezing water drops. *Quarterly Journal of the Royal Meteorological Society*, 86(368):176–185, 1960. doi: 10.1002/qj.49708636806. URL `https://rmets.onlinelibrary.wiley.com/doi/abs/10.1002/qj.49708636806`.

McFarquhar, G. M., Ghan, S., Verlinde, J., Korolev, A., Strapp, J. W., Schmid, B., Tomlinson, J. M., Wolde, M., Brooks, S. D., Cziczo, D., Dubey, M. K., Fan, J., Flynn, C., Gultepe, I., Hubbe, J., Gilles, M. K., Laskin, A., Lawson, P., Leaitch, W. R., Liu, P., Liu, X., Lubin, D., Mazzoleni, C., Macdonald, A.-M., Moffet, R. C., Morrison, H., Ovchinnikov, M., Shupe, M. D., Turner, D. D., Xie, S., Zelenyuk, A., Bae, K., Freer, M., and Glen, A. Indirect and semi-direct aerosol campaign. *Bulletin of the American Meteorological Society*, 92(2):183–201, 2011. doi: 10.1175/2010BAMS2935.1. URL `https://doi.org/10.1175/2010BAMS2935.1`.

Mlawer, E. J., Taubman, S. J., Brown, P. D., Iacono, M. J., and Clough, S. A. Radiative transfer for inhomogeneous atmospheres: Rrtm, a validated correlated-k model for the longwave. *Journal of Geophysical Research: Atmospheres*, 102(D14):16663–16682, 1997. doi: 10.1029/97JD00237. URL `https://agupubs.onlinelibrary.wiley.com/doi/abs/10.1029/97JD00237`.

Mossop, S. C. The origin and concentration of ice crystals in clouds. *Bulletin of the American Meteorological Society*, 66(3):264–273, 1985. doi: 10.1175/1520-0477(1985)066<0264:TOACOI>2.0.CO;2. URL `https://doi.org/10.1175/1520-0477(1985)066<0264:TOACOI>2.0.CO;2`.

Mossop, S. C., Ono, A., and Wishart, E. R. Ice particles in maritime clouds near tasmania. *Quarterly Journal of the Royal Meteorological Society*, 96(409):487–508, 1970. doi: 10.1002/qj.49709640910. URL `https://rmets.onlinelibrary.wiley.com/doi/abs/10.1002/qj.49709640910`.

Mülmenstädt, J., Sourdeval, O., Delanoë, J., and Quaas, J. Frequency of occurrence of rain from liquid-, mixed-, and ice-phase clouds derived from a-train satellite retrievals. *Geophysical Research Letters*, 42(15):6502–6509, 2015. doi: 10.1002/2015GL064604. URL `https://agupubs.onlinelibrary.wiley.com/doi/abs/10.1002/2015GL064604`.

Ovchinnikov, M., Ackerman, A. S., Avramov, A., Cheng, A., Fan, J., Fridlind, A. M., Ghan, S., Harrington, J., Hoose, C., Korolev, A., McFarquhar, G. M., Morrison, H., Paukert, M., Savre, J., Shipway, B. J., Shupe, M. D., Solomon, A., and Sulia, K. Intercomparison of large-eddy simulations of arctic mixed-phase clouds: Importance of ice size distribution assumptions. *J. Adv. Model. Earth Syst.*, 6(1):223–248, 2014. doi: 10.1002/2013MS000282.

Phillips, V. T. J., Yano, J.-I., and Khain, A. Ice multiplication by breakup in ice–ice collisions. part i: Theoretical formulation. *Journal of the Atmospheric Sciences*, 74(6):1705–1719, 2017. doi: 10.1175/JAS-D-16-0224.1. URL `https://doi.org/10.1175/JAS-D-16-0224.1`.

Pruppacher, H. R. and Klett, J. D. *Microphysics of clouds and precipitation*. Dordrecht: Kluwer Academic Publishers, 1997.

Rangno, A. L. and Hobbs, P. V. Ice particles in stratiform clouds in the arctic and possible mechanisms for the production of high ice concentrations. *Journal of Geophysical Research: Atmospheres*, 106(D14):15065–15075, 2001. doi: 10.1029/2000JD900286. URL `https://agupubs.onlinelibrary.wiley.com/doi/abs/10.1029/2000JD900286`.

Schär, C., Leuenberger, D., Fuhrer, O., Lüthi, D., and Girard, C. A new terrain-following vertical coordinate formulation for atmospheric prediction models. *Monthly Weather Review*, 130 (10):2459–2480, 2002. doi: 10.1175/1520-0493(2002)130<2459:ANTFVC>2.0.CO;2. URL `https://doi.org/10.1175/1520-0493(2002)130<2459:ANTFVC>2.0.CO;2`.

Seifert, A. and Beheng, K. D. A two-moment cloud microphysics parameterization for mixed-phase clouds. part 1: Model description. *Meteorology and Atmospheric Physics*, 92(1):45–66, Feb 2006. ISSN 1436-5065. doi: 10.1007/s00703-005-0112-4. URL `https://doi.org/10.1007/s00703-005-0112-4`.

Seifert, A. *Parametrisierung wolkenmikrophysikalischer Prozesse und Simulation konvektiver Mischwolken*. PhD thesis, Karlsruhe Institute of Technology (KIT), 7 2002.

Shupe, a. D., Uttal, T., and Matrosov, S. Y. Arctic cloud microphysics retrievals from surface-based remote sensors at sheba. *Journal of Applied Meteorology*, 44(10):1544–1562, 2005. doi: 10.1175/JAM2297.1. URL `https://doi.org/10.1175/JAM2297.1`.

Sullivan, S. C., Barthlott, C., Crosier, J., Zhukov, I., Nenes, A., and Hoose, C. The effect of secondary ice production parameterization on the simulation of a cold frontal rainband. *Atmospheric Chemistry and Physics*, 18(22):16461–16480, 2018. doi: 10.5194/acp-18-16461-2018. URL `https://www.atmos-chem-phys.net/18/16461/2018/`.

Sullivan, S., Hoose, C., Kiselev, A., Leisner, T., and Nenes, A. Initiation of secondary ice production in clouds. *Atmospheric Chemistry and Physics Discussions*, 18:1–22, 05 2017a. doi: 10.5194/acp-18-1593-2018.

Sullivan, S., Hoose, C., and Nenes, A. Investigating the contribution of secondary ice production to in-cloud ice crystal numbers: Secondary ice production. *Journal of Geophysical Research: Atmospheres*, 122, 07 2017b. doi: 10.1002/2017JD026546.

Takahashi, T., Nagao, Y., and Kushiyama, Y. Possible high ice particle production during graupel–graupel collisions. *Journal of the Atmospheric Sciences*, 52(24):4523–4527, 1995. doi: 10.1175/1520-0469(1995)052<4523:PHIPPD>2.0.CO;2. URL `https://doi.org/10.1175/1520-0469(1995)052<4523:PHIPPD>2.0.CO;2`.

Vardiman, L. The generation of secondary ice particles in clouds by crystal–crystal collision. *Journal of Atmospheric Sciences*, 35:2168–2180, 10 1978. doi: 10.1175/1520-0469(1978)035<2168:TGOSIP>2.0.CO;2.

Verlinde, J., Harrington, J. Y., McFarquhar, G. M., Yannuzzi, V. T., Avramov, A., Greenberg, S., Johnson, N., Zhang, G., Poellot, M. R., Mather, J. H., Turner, D. D., Eloranta, E. W., Zak, B. D., Prenni, A. J., Daniel, J. S., Kok, G. L., Tobin, D. C., Holz, R., Sassen, K., Spangenberg, D., Minnis, P., Tooman, T. P., Ivey, M. D., Richardson, S. J., Bahrmann, C. P., Shupe, M., DeMott, P. J., Heymsfield, A. J., and Schofield, R. The mixed-phase arctic cloud experiment. *Bulletin of the American Meteorological Society*, 88(2):205–222, 2007. doi: 10.1175/BAMS-88-2-205. URL `https://doi.org/10.1175/BAMS-88-2-205`.

Zängl, G., Reinert, D., Rípodas, P., and Baldauf, M. The icon (icosahedral nonhydrostatic) modelling framework of dwd and mpi-m: Description of the nonhydrostatic dynamical core. *Quarterly Journal of the Royal Meteorological Society*, 141, 01 2015. doi: 10.1002/qj.2378.

Acknowledgement

The last twelve month truly were an experience. Diving into a relatively unknown subject I learned more than I could have expected; about science, meteorology, modeling, hard work and teamwork.

My interest in the field of atmospheric science has grown tremendously.

For making that possible I would like to thank Prof. Dr. Corinna Hoose. I want to thank her for being open minded, supportive and a very good listener; and a very spontaneous listener, always having a minute to spare.

Furthermore I want to thank Prof. Dr. Thomas Leisner, for taking on the role of second referee.

I would like to thank Dr. Hassan Beydoun for being resilient in recruiting me for this thesis, being my supervisor and lending an ear, even from across the Atlantic.

Working with the whole team of the cloud physics group was a very pleasant undertaking. Thank you for the nice atmosphere and the productive environment.

Special thanks to Dr. Christian Barthlott who was always available to solve computational obstacles, and to Dr. Andrew Barrett, who really stepped in as a part time supervisor and being of great help concerning modeling and programing.

Finally I want to thank my family, Brigitte Morsch-Kuntze, Thomas Kuntze and Oliver Kuntze for their unconditionally support and always believing in me. And my partner in life Marisa Lang I want to thank for her incredible patience and loving support.

Declaration of Authorship

I hereby declare that the thesis submitted is my own unaided work. All direct or indirect sources used are acknowledged as references. I am aware that the thesis in digital form can be examined for the use of unauthorized aid and to determine wether the thesis as a whole or parts incorporated in it may be deemed as plagiarism.
For the comparison of my work with existing sources I agree that it shall be entered in a database where it shall also remain after examination, to enable comparison with future theses submitted. Further rights of reproduction and usage, however, are not granted here. This paper was not previously presented to another examination board and has not been published.

Karlsruhe, 05. 11. 2019

Patrick Kuntze